Dynamic Modeling, Control and Energy Simulation of a Solar-assisted

Hydronic Space Heating System in a Multi-function Building

Xiangyu Cai

A Thesis

in

Department

of

Building, Civil and Environmental Engineering

Presented

in

Partial Fulfillment of Requirements

for the Degree of Master of Applied Science at

Concordia University

Montreal, Quebec, Canada

March 2019

CONCORDIA UNIVERSITY
School of Graduate Studies

This is to certify that the thesis prepared

By: Xiangyu Cai

Entitled: Dynamic Modeling, Control and Energy Simulation of a Solar-assisted Hydronic
Space Heating System in a Multi-function Building

and submitted in partial fulfillment of the requirements for the degree of

Master of Applied Science (Building Engineering)

complies with the regulations of the University and meets the accepted standards with respect to
originality and quality.

Signed by the final Examining Committee:

_____Chair
Dr. H. Ge

_____External Examiner
Dr. M. Y. Chen

_____Examiner
Dr. J. Lee

_____Examiner
Dr. H. Ge

_____Supervisor
Dr. M. Zaheeruddin

Approved by   _____
Chair of Department or Graduate Program Director

_____
Dean of Faculty

Date   _____

ABSTRACT

Dynamic Modeling, Control and Energy Simulation of a Solar-assisted Hydronic Space Heating
System in a Multi-function Building

Xiangyu Cai

A dynamic model of a solar-assisted hydronic space heating system for a multi-function
building has been developed. The system performance under different control strategies and the
model-based energy simulations studies have been conducted. The system consists of several
components including a boiler, heat exchangers, flat-plate solar collectors, a water storage tank,
baseboard heaters and a radiant floor heating system. The model consists of nonlinear differential
equations which were programmed and solved using the MATLAB software.

Two control strategies have been explored to compare the system performance: (i) a
conventional PI control and (ii) a gain-scheduling adaptive (GSA) PI control. The simulation
results indicate that the system performance under GSA PI control is better than the conventional
PI control with respect to disturbance rejection and stability.

An optimization problem was formulated and solved to study the energy performance of
the system. Preliminary simulation results with assumed outdoor temperature profiles showed that
the optimized set-point operating strategy contributes 7% and 14.87% to boiler energy saving in
mild and warm day conditions compared with constant set-point strategy.

One week energy simulations under actual weather conditions based on typical
meteorological year (TMY) data have been conducted to investigate the percent contribution of
solar energy to space heating. The simulation results show that the solar system contributes less

energy during cold winter conditions such as in the month of December. However, it can reduce 16.94% of boiler energy supplied to the radiant floor heating system in the month of March. Besides, the implementation of the optimal GSA PI control strategy can result in higher solar fractions of 5.71% and 30.36% as compared to the base case PI control under cold (December) and mild (March) weather conditions, respectively.

ACKNOWLEDGEMENTS

I would first like to express my sincere gratitude to my thesis supervisor: Dr. M. Zaheer-Uddin, for his invaluable guidance, encouragement and financial support during the whole span of this thesis.

Sincere thanks are also given to my colleagues: Min Ning, Songchun Li and Hanfei Cao, for their help in my study. I would also express my appreciations to the staff in BCEE department.

Finally, I would like to dedicate this thesis to my parents Shaozhen Liu, Qiuhua Cai and my best friends, for their patience, understanding, encouragement and support during my whole studies.

TABLE OF CONTENTS

LIST OF FIGURES

LIST OF TABLES

NOMENCLATURE

$A_{wall,czi/rzi}$	Commercial or residential zone i net wall area (m²)
$A_{win,czi/rzi}$	Commercial or residential zone i window area (m²)
$A_{rf,rzi}$	Residential zone i roof area (m²)
A_{sc}	Flat-plate solar collector area (m²)
A_{tank}	Storage tank surface area (m²)
A_1	Heat transfer area on the top of RFH tube node (m²)
A_2	Heat transfer area on the top of RFH concrete node (m²)
a_j	Boiler jacket heat loss coefficient (J/°C)
c_a	Specific heat of air (J/kg K)
c_f	Specific heat of working fluid (antifreeze) in solar collector (J/kg K)
c_w	Specific heat of water (J/kg K)
c_c	Specific heat of RFH concrete slab (J/kg K)
c_{flo}	Specific heat of RFH flooring (J/kg K)
C_{brick}	Thermal capacity of face brick (J/°C)
$C_{htr,i}$	Thermal capacity of baseboard heater i (J/°C)
$C_{cz,i}$	Thermal capacity of commercial zone i (J/°C)
$C_{rz,i}$	Thermal capacity of residential zone i (J/°C)
C_{hxp}	Thermal capacity of water stored in the heat exchanger primary side (hot side) (J/°C)

C_{hxs}	Thermal capacity water stored in the heat exchanger secondary side (cold side) (J/°C)
C_{wt}	Thermal capacity of the water inside the tube node $T_{w,i}$ (J/°C)
C_{c1}	Thermal capacity of the RFH concrete node in transverse direction of C_{wt} node (J/°C)
C_{c2}	Thermal capacity of the RFH concrete node in perpendicular direction of C_{wt} node (J/°C)
C_{c3}	Thermal capacity of the RFH concrete node in transverse direction of C_{c2} node (J/°C)
C_{flo1}	Thermal capacity of the floor node on top of C_{c2} node (J/°C)
C_{flo2}	Thermal capacity of the floor node on top of C_{c3} node (J/°C)
C_{bond}	Bond conductance
C_{sc}	Thermal capacity of the solar collector node (J/°C)
C_{tank}	Thermal capacity of water stored in the storage tank (J/°C)
C_b	Thermal capacity of gas-fuel boiler (J/°C)
d_a	Density of the air (kg/m^3)
d_c	Density of the concrete slab (kg/m^3)
d_{flo}	Density of the flooring (kg/m^3)
d_f	Density of working fluid (kg/m^3)
$D_{o,rfh}$	Radiant floor heating system tube outer diameter (mm)
$D_{i,rfh}$	Radiant floor heating system tube inner diameter (mm)
$D_{o,sc}$	Flat-plate solar collector riser outer diameter (mm)

$D_{i,sc}$	Flat-plate solar collector riser inner diameter (mm)
e_b	Boiler efficiency (%)
e	Error between set-point temperature and measured temperature
F_{en}	Radiation angle factor between RFH surface node and enclosure
F	Flat-plate solar collector fin efficiency factor
F'	Flat-plate solar collector efficiency factor
F_R	Flat-plate collector heat removal factor
$F_R{}'$	Solar coil heat exchanger heat removal factor
h_o	Heat transfer coefficient of the exterior surface film (W/m^2 °C)
h_i	Heat transfer coefficient of the interior surface film (W/m^2 °C)
h_{wind}	Heat transfer coefficient of wind effect (W/m^2 °C)
h_f	Heat transfer coefficient between the working fluid and tube wall (W/m^2 °C)
HV	Heating value of the natural gas (J/Kg)
I	Solar irradiance (W/m^2)
K_p	Solar collector absorber plate thermal conductivity (W/m °C)
K_t	Thermal conductivity of water tube (W/m °C)
K_c	Thermal conductivity of concrete (W/m °C)
K_{flo}	Thermal conductivity of flooring (W/m °C)
k_p	Controller proportional gain
k_i	Controller integral gain

$m_{w,czi}$	Commercial zone i water flow rate (kg/s)
$m_{w,czi,d}$	Commercial zone i design water flow rate (kg/s)
$m_{w,rzi}$	Residential zone i water flow rate (kg/s)
$m_{w,rzi,d}$	Residential zone i design water flow rate (kg/s)
$m_{w,hxp}$	Heat exchanger primary side (hot side) water flow rate (kg/s)
$m_{w,hxs}$	Heat exchanger secondary side (cold side) water flow rate (kg/s)
m_{sc}	Working fluid flow rate in flat-plate solar collector (kg/s)
m_{fmax}	Maximum fuel consumption rate in boiler (kg/s)
N	Number of cover layers in flat-plate solar collector
N_{sc}	Number of flat-plate solar collectors
n	Factor identified based on baseboard heater heat transfer test
$Q_{rad,conv,i}$	Radiative and convective heat transfer from radiant floor slab to zone i (W)
$Q_{int,czi/rzi}$	Internal heat gain for commercial and residential zone i (W)
$Q_{sol,czi/rzi}$	Solar heat gain for commercial and residential zone i (W)
q_{sc}	Single flat-plate solar collector energy gain (W)
q_{sct}	Total flat-plate solar collectors energy gain (W)
q_{useful}	Useful solar energy gain from collectors' array with a heat exchanger coil (W)
q_{hx}	Heat exchanger heat transfer rate between the primary and secondary side (W)
$u_{w,czi}$	Flowrate control signal for commercial zone i
$u_{w,rzi}$	Flowrate control signal for residential zone i

U_{win} Heat transfer coefficient of the window (W/m^2 °C)

U_{wall} Heat transfer coefficient of the wall (W/m^2 °C)

U_{rf} Heat transfer coefficient of the roof (W/m^2 °C)

U_{w1} Heat transfer coefficient between the face brick node to face brick surface node (W/m^2 °C)

U_{w2} Heat transfer coefficient between the face brick node to indoor environment (W/m^2 °C)

$U_{htr,i}$ Heat transfer coefficient of each baseboard heater i (W/°C)

U_{cond_wc1} Heat transfer coefficient between water node and its horizontal concrete node (W/m °C)

U_{cond_wc2} Heat transfer coefficient between water node and its vertical concrete node (W/m °C)

U_{cond_c1c3} Heat transfer coefficient between concrete node 1 and concrete node 3 (W/m °C)

U_{cond_c2c3} Heat transfer coefficient between concrete node 2 and concrete node 3 (W/m °C)

U_{cond_c2f1} Heat transfer coefficient between concrete node 2 and flooring node 1 (W/m °C)

U_{cond_c3f2} Heat transfer coefficient between concrete node 2 and flooring node 2 (W/m °C)

U_{cond_f1f2} Heat transfer coefficient between flooring node 1 and flooring node 2 (W/m °C)

U_{cond_f1sf1}	Heat transfer coefficient between flooring node 1 and floor surface node 1 (W/m °C)
U_{cond_f2sf2}	Heat transfer coefficient between flooring node 2 and floor surface node 2 (W/m °C)
U_{sc}	Flat-plate solar collector heat loss coefficient (W/m² °C)
U_{tank}	Water storage tank heat loss coefficient (W/m² °C)
$Vol_{cri,rzi}$	Zone Volume (m³)
W_{sc}	Riser pitch in flat-plate solar collector (mm)
T_o	Outdoor air temperature (°C)
T_a	Ambient air temperature (°C)
T_{brick}	Face brick temperature (°C)
T_{bsf}	Face brick surface temperature (°C)
$T_{z,czi}$	Commercial zone i indoor air temperature (°C)
$T_{z,rzi}$	Residential zone i indoor air temperature (°C)
$T_{s,cz}$	Commercial zones supply water temperature (°C)
$T_{r,cz}$	Commercial zones return water temperature (°C)
$T_{s,rz}$	Residential zones supply water temperature (°C)
$T_{r,rz}$	Residential zones return water temperature (°C)
$T_{s,czi}$	Commercial zone i supply water temperature (°C)
$T_{r,czi}$	Commercial zone i return water temperature (°C)
$T_{s,rzi}$	Residential zone i supply water temperature (°C)
$T_{r,rzi}$	Residential zone i return water temperature (°C)

$T_{htr,i}$	Outlet water temperature of baseboard heater i (°C)
$T_{w,i}$	Water temperature in tube node i (°C)
$T_{c1,i}$	Concrete temperature around tube in water tube layer (°C)
$T_{c2,i}$	Concrete temperature above tube in concrete layer (°C)
$T_{c3,i}$	Concrete temperature in concrete layer (°C)
$T_{flo1,i}$	Flooring temperature above tube in flooring layer (°C)
$T_{flo2,i}$	Flooring temperature above concrete in flooring layer (°C)
$T_{sf1,i}$	Floor surface temperature above tube (°C)
$T_{sf2,i}$	Floor surface temperature above concrete (°C)
$T_{r,rfh,i}$	Residential zone i radiant floor system return water temperature (°C)
T_{pm}	Solar collector plate mean temperature (°C)
T_{sci}	Solar collector inlet fluid temperature (°C)
T_{sco}	Solar collector outlet fluid temperature (°C)
T_{tank}	Solar tank water temperature (°C)
$T_{i,hxp}$	Heat exchanger primary side inlet water temperature (°C)
$T_{o,hxp}$	Heat exchanger primary side outlet water temperature (°C)
$T_{o,hxs}$	Heat exchanger secondary side outlet water temperature (°C)
$T_{i,hxs}$	Heat exchanger secondary side inlet water temperature (°C)
$T_{s,bhx}$	Supply water temperature to boiler heat exchanger (°C)
$T_{r,bhx}$	Return water temperature from boiler heat exchanger (°C)
T_{shx}	Outlet water temperature from solar heat exchanger (°C)

$T_{s,b}$ Boiler supply water temperature (°C)

$T_{r,b}$ Boiler return water temperature (°C)

SUBSCRIPTS

agg	referring to aggregated
conv	referring to convective
cond	referring to conductive
rad	referring to radiative
w	referring to water
s	referring to supply
sc	referring to solar collector
r	referring to return
f	referring to working fluid
htr	referring to heater
int	referring to internal
win	referring to window
sf	referring to surface
rf	referring to roof
cz/rz	referring to commercial or residential zone
bhx	referring to boiler heat exchanger
shx	referring to solar heat exchanger
sol	referring to solar
b	referring to boiler

GREEK LETTERS

α	Absorption coefficient
ε	Surface emittance
ϵ	Effectiveness
k	Thermal conductivity (W/m °C)
δ	Thickness (mm)
μ	Fluid dynamic viscosity (Kg/m s)
τ	Transmission coefficient

ABBREVIATION

C	Controller
$ACH_{czi/rzi}$	Air changer rate per hour for commercial and residential zone i (/hour)
NTU	Number of transfer units
HVAC	Heating, ventilation and air conditioning
OLT	Open-loop test
RFH	Radiant floor heating
PI	Proportional and integral control
GSA	Gain scheduling adaptive

CHAPTER 1 INTRODUCTION

1.1 Introduction

Over the years, energy consumption has been a prevalent topic of research interest around the world. Building energy consumption, as the dominant portion of overall energy consumption, has drawn more attention in the research field. According to the statistics from the World Business Council for Sustainable Development, buildings worldwide account for 40% of the global energy consumption [28]. Available energy use statistics by sector from U.S. and Canada, both indicate similar percentage about energy use in residential and commercial buildings representing 47.6% of the U.S. energy consumption and 27% of total Canadian energy use in 2013[27] [20]. Moreover, Canadian energy use statistics contained in Energy Use Data Handbook published by Natural Resources Canada (NRCan) indicates that space heating as the largest end-use, accounting for 59.3% of total residential and commercial buildings energy consumption [19]. In most buildings, hydronic space heating systems are the primary source of space heating systems. Therefore, it is important to develop innovative design and operation strategies for the hydronic space heating systems such that significant savings in building energy consumption could be achieved.

In recent years, for the majority of the hydronic space heating systems, a gas-fired boiler is the preferred choice. Even though the high-efficiency boiler heating systems are widely used, the fact remains that fossil fuel energy systems are not sustainable and environmentally unfriendly. New and replaceable sustainable energy is becoming a popular research subject. In the last few years, two active solar technologies are becoming more common around the world. The first one is solar photovoltaic technology which converts sunlight directly into electric form by using a semiconductor material. Another one is solar thermal collector which absorbs solar energy and

transfer it into usable heat form. Flat-plate and concentrating solar collectors are two available solar products in the industry. According to NRCan, Canada has tremendous potential for solar energy use, and it has excellent solar resources. Since 2007, there are an estimated 544,000 m^2 of solar collectors operating across Canada. Comparing with other sources of energy, solar has several distinct advantages, such as its renewability, and affordability. Solar energy applications related to building HVAC system include domestic water heating, space heating, solar cooling and so forth.

To this end, an integrated system combining the hydronic heating and solar thermal system is a preferred option in northern climates. Therefore, a solar-assisted hydronic space heating system for a multi-functional building is proposed in this thesis. A solar thermal collector system is integrated into the conventional boiler hydronic heating system. In this manner, the heat load can be partially or completely fed by solar energy so that the boiler input energy can be decreased. The interactions of combined systems are examined and evaluated regarding system performance and temperature control.

1.2 The scope and objectives

The scope of this thesis is to develop a solar-assisted hydronic space heating system model, to explore appropriate control and operating strategies, and to conduct system energy simulations over a wide range of operating conditions.

The main objectives of this study are presented as follow:

1) Design a solar-assisted hydronic space heating system for a multi-functional building located in Montreal based on steady-state design methods.

2) Develop a dynamic model for each component of the hydronic space heating system, and simulate the integrated system dynamic response under design day load conditions.

3) Explore appropriate adaptive control strategies for the multi-loop system and examine the overall system dynamic performance of different control strategies under different load conditions.

4) Develop an optimal operation strategy for the overall system by formulating and solving a multi-variable constraint optimization problem in order to minimize the energy input to the system.

5) Conduct simulation runs with the optimal operation and control strategies to evaluate the potential system energy savings due to the utilization of solar energy.

1.3   The thesis organization

This thesis is organized into seven main chapters. Introduction to the thesis is covered in Chapter 1, Chapter 2 presents a literature review of previous studies about the hydronic space heating system modeling and building HVAC system control strategies. Chapter 3 is focused on the development of a dynamic model for the solar-assisted hydronic space heating system and the open loop test of the system. The content of next Chapter 4 is about the hydronic space heating system control strategy studies. Constant gain proportional-integral (PI), on-off and gain scheduling adaptive gain PI controls are discussed in this chapter. The following Chapter 5 is regarding the system optimization. By using the $f_{mincon}(J)$ function in MATLAB program, the

objective is to find the optimized system supply water temperature set-points. The Chapter 6 is about the system energy simulation and determine the fraction of solar energy utilization. Two real outdoor conditions are used to investigate the overall system energy consumption and the fraction of solar energy utilization. Conclusions, contributions and recommendations for future research are given in Chapter 7.

CHAPTER 2 LITERATURE REVIEW

2.1 Introduction

The developed solar-assisted hydronic space heating system consists of several components, such as boiler, heat exchanger, radiant floor heating system, baseboard heater heating system, solar thermal collector, water storage tank, pipe distribution system and et cetera. A literature review of the hydronic space heating system models will be discussed initially in this chapter. After that, a literature review for exploring the hydronic space heating system control and operation strategies will be presented.

2.2 Literature review

2.2.1 Boiler hydronic space heating system models

Boiler dominant hydronic space heating systems, as the most common space heating approach, have been widely studied and applied so far. The dynamic models for boiler dominant hydronic space heating systems related components, such as a gas-fired boiler, radiant floor heating and baseboard heaters, are developed by many researchers. Huang and Ko (1994) developed a dynamic model of a fire-tube shell boiler. To simplify the simulation process, a three nodes-lumped model was derived. The boiler was divided into three distinct phases: solid, liquid, and gaseous phases. Each phase was assumed to be at uniform temperature. By applying the energy and mass balance principle to each phase, a linear time-invariant perturbed model around steady-state operating points was derived. The dynamic response of this derived model was shown to agree very well with the test results. The study did not include control design for the boiler.

Liao and Parand (2002) proposed a gas-fired boiler model which consists of four major parts: an inner shell, a water channel, an outer shell and an insulation layer. By using the electrical circuit analogy, a dynamic model of heat transfer processes was developed. Besides, the dynamic model was validated with experimental data, which showed good agreement.

L. Li et al. (2010) developed a dynamic model for an indirect district heating system. This dynamic model consists of several sub-system models, including the boiler, heat exchanger, terminal heater and zones. The sub-system models, such as the boiler, and the terminal heater were developed using energy balance principles and data from field tests. Moreover, the log mean temperature difference (LMTD) method was employed to establish the water-to-water heat exchanger model. The model simulation results showed that the overall efficiency of the indirect district heating system is around 79%. Two highest components of heat loss were identified as the boiler heat losses and secondary water makeup.

S. Li and Zaheeruddin (2013) established a radiant floor slab model to simulate the dynamic performance of a radiant floor heating system. The hot water circulating inside the water tubes transfers heat to the surrounding medium by heat conduction. Then, the heat is released to the zone air through radiation and convection heat transfer between the slab surface and zone environment. Since the hot water temperature is decreasing in the flow direction the hot water pipe was divided into several nodes and the temperature of each node is assumed to be at uniform temperature. By applying the energy balance and mass balance principles for each node, the dynamic model was developed, and its performance was simulated. The simulated responses were compared with experimental results which showed good agreement thus validating the effectiveness of this model.

2.2.2 Solar-assisted hydronic space heating system models

In the past few years, various kinds of solar-assisted hydronic space heating systems became commercially available. Many studies were conducted to investigate the solar contribution of hydronic space heating system. Z. Zhang et al. (1988) conducted an experimental study of a solar-radiant heating system. In the experiment, the solar collectors heat the water in the storage tank which is then circulated through a heat exchanger to the radiant ceiling panel system. The experimental results showed that it was feasible to use a solar system integrated into a low-temperature radiant-panel heating system for space heating. However, such standalone solar systems are unlikely to provide heating in cold climates.

Haddad et al. (2007) carried out an energy comparison between a forced-air heating system and a radiant floor heating system. Both systems use a low-temperature tank to store available or additional solar energy. The results showed that the portion of the heating load that comes from solar energy is higher in the case of the radiant floor heating system. The authors conclude that the portion from solar energy increases when the radiant floor system operates with a lower water temperature.

Zelzouli et al. (2012) investigated the solar system thermal performance for two different kinds of settings: solar direct hot water and solar indirect hot water. The only difference between these two systems is an additional external heat exchanger in an indirect solar system. The simulated results showed that the mass flow rate in the solar system has a significant impact on the system performance in both systems. Besides, the storage tank volume has a strong impact on the performance of the system. When the storage volume is bigger, the solar fraction is less sensitive to the load variation on the performance of the system.

Sobhansarbandi and Atikol (2015) explored the possibility of using compound parabolic concentrating solar collectors instead of the normally used flat-plate solar collectors in the underfloor heating system. The system consists of solar thermal collectors, a storage tank, and water circulation pumps to four underfloor heating systems. The simulation results showed that this system maintained a higher fluid temperature at the collector outlet. In this manner, the collector area can be reduced without sacrificing solar performance.

Many researchers have developed dynamic models for solar-related hydronic space heating system components over the last few years. The models of solar thermal collectors account for a large proportion. In addition to solar collectors, the heat exchangers and storage tank play an important role in solar thermal systems. Heat exchangers are often used between solar collector and storage allowing for the use of antifreeze solution in the collector loop, especially in cold climates.

Arinze et al. (1992) proposed a dynamic model for the flat-plate solar collector. This dynamic model describes the fluid, plate and cover temperatures by three different differential equations. The simulation results showed a reasonable match with the measured experimental data. However, several assumptions have been made in the simulation model which may have an impact on the system performance, such as the heat capacity of the air gap between the cover and absorber is neglected. The temperature gradient in the direction of perpendicular to the fluid flow is also neglected, and the heat flow through the insulation is assumed to be negligible.

Kazeminejad (2002) conducted a numerical study of flat-plate solar collectors. The authors stated that the conventional one-dimensional analysis method is accurate enough for most engineering purposes. However, for optimum design, they recommended two-dimensional

analysis, especially under lower mass flow rate situations. The results indicated that a large number of parameters have an impact on the performance of flat-plate solar collectors, such as fluid inlet temperature, the fluid mass flow rate in the collector and tube spacing.

Cadafalch (2009) developed a basic one-dimensional transient numerical model for a flat-plate solar collector based on the control volume method. Comparisons between simulated and experimental data were made to verify the accuracy of the proposed model. However, this model is limited only for standard flat-plate solar collectors. For other types of solar collectors, this model cannot be used.

Saleh (2012) developed a detailed five-node flat-plate solar collector model to represent all layers of the collector. From outer to inner, these layers include a glass cover layer, an air gap layer, an absorber layer, fluid flow and insulation s, respectively. The governing differential equations were solved by applying the implicit finite difference method. During the simulating process, the solar radiation and ambient conditions were considered as time-dependent. The model predictions showed a good match with experimental data.

Duffie and Backman (2013) proposed a dynamic model for flat-plate solar collectors which has been broadly used for predicting the solar thermal performance nowadays. They included a number of critical factors, such as the overall heat loss coefficient and collector heat removal factor, into governing equations and formulated a simplified mathematical model to describe the thermal performance of the solar collector. Moreover, Duffie and Backman (2013) also proposed a single node and multi-node models for the solar water storage tank. In the single node model, the storage tank was assumed to be at uniform temperature. In the multi-node model, the storage tank was divided into several nodes or sections. By applying energy balance equations to each node, a set

of differential equations were established as a function of time. Furthermore, Duffie and Backman (2013) proposed an effectiveness-NTU (number of transfer units) method to simulate the heat exchanger performance.

2.2.3 HVAC system control and operation strategies

Zaheeruddin (1991) explored a sub-optimal control strategy for a dual-source heat pump system for space heating. This dual-source heat pump has an ambient air source as well as a solar collector source. The control strategy for the heat pump selects the air source mode or collector mode depending on which one has higher available energy. Simulation results showed that the adaptive feedback controllers were able to respond effectively to the load changes. It was shown that the application of this strategy resulted in a significant reduction in purchased energy requirements. The author concluded that through increasing the size of the solar collector, the thermal capacity of the storage tank and the building-loop heat transfer coefficient, the space heating system could achieve higher energy savings.

Zheng et al. (1997) developed an optimal control strategy for an embedded-piping floor heating system. An optimal operating strategy was designed by formulating and solving a multi-variable constrained optimization problem. By defining an appropriate objective function, the energy input to the boiler was minimized while maintaining the zone temperature at the desired set-point. The simulation results showed energy savings of the order of 15-20% while the zone temperature was held within 0.5°C of the set-point throughout the day.

Seem (1998) described an adaptive control strategy which can adjust the gain and integral time of the proportional-integral (PI) controller automatically based on the pattern recognition of

the close-loop system response. This method is limited to systems that can be modeled as the first-order-plus-dead-time system. Application of this adaptive controller to the HVAC system was shown by showing simulation results. Zaheeruddin et al. (2002) developed a dynamic model of a radiant floor heating system. This dynamic model consists of a boiler, water distribution e system, an embedded tube floor slab and building enclosure. The overall model was described by non-linear differential equations. Two control strategies were investigated in this study: a multistage on-off control and augmented constant gain control. The results showed that the multistage on-off controller could have a better set-point regulation compared with the existing on-off control scheme. The augmented constant gain controller showed a better zone temperature control in response to changes in outdoor air temperature.

Qu and Zaheeruddin (2004) developed an adaptive PI control strategy for local loop HVAC processes that can be described by a first-order-plus-dead-time model. The tuning methodology updated the controller parameters in real-time while the control system remains in the closed-loop. This adaptive PI control was applied to a discharge air temperature (DAT) HVAC system. The simulation results indicated that the proposed adaptive PI control strategy works very well in response to changes in plant parameters, disturbances and external noise acting on the HVAC system.

Bai and Zhang (2007) proposed a new adaptive PI controller for use in HVAC systems. The HVAC process was described by a first order plus dead time model. A simple tuning formula for a PI controller with robustness based on the estimated parameters was applied to modify the parameters automatically while under the closed loop. The simulation results showed that this new

adaptive PI control strategy has a faster response, smaller overshoot and higher accuracy than the other adaptive control methods under load disturbances or set-point changes.

Ning and Zaheeruddin (2010) proposed a neural network based optimal supervisory control strategy for the efficient operation of a two-zone VAV-HVAC&R system. A dynamic model was established initially to simulate the overall system response under different scenarios. A multi-layer feed forward neural network was trained to minimize the objective cost function. After that, a neural network based optimization algorithm was developed to find out the optimal set-points for the VAV system. The energy simulation results showed that compared with conventional night reset operation scheme; this suggested optimal operation scheme can save around 10% energy in full load and 19% energy in partial load conditions, respectively.

Singh et al. (2000) developed a multivariable adaptive control strategy for a two-zone fan-coil heating (FCH) system which consists of a hot water boiler, a fan-coil unit for each zone, two environmental zones and a two pipe distribution system. This multivariable adaptive controller was designed based on the linear quadratic regulator (LQR) theory. The simulation results showed that the suggested controller was able to adapt to a wide range of operating conditions and was also able to maintain the zone air temperature and the boiler supply water temperature close to their respective set-points.

Haddad (2011) proposed an on-off and outdoor temperature reset control strategies for a solar-assisted radiant floor heating system. For this system, the radiant loops were fed with water which was first heated by using solar energy stored in the tank and then using a boiler. Two independent pumps and heat exchangers were placed between flat-plate solar collector and storage tank side, between solar storage tank and RFH system return water loop side respectively. Once

the temperature difference between the tank and collector outlet reach 5.5°C, the pump in the collector side was turned on, and it was turned off when this temperature difference drops to 1°C. For another side, the pump was turned on when the temperature of the tank was at least 5°C higher than the radiant floor return water temperature or a call for heating. This pump was turned off when this temperature drops to 1°C or no more call for heating. Besides, the solar system and the boiler share the same supply water set-point. The results indicated that the solar fraction was increased by 17% when the supply temperature to the radiant loops was varied based on outdoor reset control strategy as opposed to a constant supply water temperature.

Candanedo et al. (2011) developed a predictive control strategy for a building with large solar heat gain. The proposed control strategy was based on the system's model and expected loads, and was investigated under two different control conditions: (i) a radiant floor heating (RFH) system and (ii) a dynamic fenestration system with automatically controlled solar transmittance. The investigation results suggested that a simplified linear model could facilitate the implementation of control strategies in homes with large solar gains and thermal mass system.

Cho et al. (2013) conducted a study of the energy performance of an optimal predictive control strategy for multi-zone radiant floor district heating systems. In this predictive control strategy, the boiler supply water set-point was predicted based on the variation in the zone load. The control strategy was applied to a four-zone radiant floor heating system. By comparing with conventional PI control, this optimal predictive control strategy was shown to contribute about 10% energy saving. Experimental results further confirmed the validity of this optimal predictive control strategy for the radiant floor district heating system.

Liu (2014) developed a gain scheduling control strategy for a chilled water cooling system which consists of a chiller, a cooling coil, a stratified chilled water tank and a cooling tower. Based on the conventional proportional-integral (PI) controller structure, the proposed gain scheduling (GS) control scheme was designed and implemented. The dynamic system performance was compared with the constant gain PI controller subjected to sudden zone set-point changes and load disturbances. The simulation results indicated that the proposed GS controller had better temperature regulation performance. Also, a near-optimal strategy combined with the GS control was designed. The system energy consumption was determined under various load conditions. The results showed that energy savings ranging from 21% to 36% could be achieved by using the optimal-GS controller in full and partial load conditions.

Li and Karava (2014) explored a methodology to develop a deterministic model predictive control (MPC) strategy for a solar integrated hydronic space heating system. This integrated solar system includes a BIPV/T panel, an air source heat pump, a thermal storage tank and a radiant floor heating system. By establishing the detailed prediction model in TRNSYS program, and simulating under the typical meteorological year condition, it was shown that the implantation of this MPC control algorithm could result in significant savings in building energy consumption.

Kang et al. (2015) proposed an advanced on-off control strategy based on a fuzzy logic methodology for a hydronic radiant floor heating (HRFH) system. The proposed controller was implemented based on a conventional on-off controller and combined with a fuzzy algorithm. A novel modeling program for thermal analysis of the radiant floor heating system was developed to include consideration of the solar impact on the system. By comparing with the traditional on-off controller, the proposed fuzzy logic based on-off controller showed a better regulation

performance in terms of reducing overheating and underheating. Also, the experimental results showed that the advanced on-off control strategy works more effectively with proper on-off timing.

Hu and Karava (2015) proposed a model-predictive control strategy for an office building integrated with solar collectors, radiant floor heating and active thermal storage tank system. Through building up the detailed model in TRNSYS and using system identification technique, a simplified model was implemented within the predictive controller. The simulation results indicated that this proposed control strategy could contribute up to 35% energy saving.

Ma and Zaheeruddin (2017) developed an adaptive control strategy for a hybrid hydronic space heating system. In this system, the water returning from the radiant floor heating system was first heated by using a geothermal source heat pump system and then increased to supply water set-point by using boiler energy. An adaptive gain PI controller was designed, and it was shown that it gives better set-point tracking performance than the conventional PI controller in disturbance rejection. Daily system energy simulations under three different operating strategies were compared as well. The results showed that the optimal adaptive PI controller could contribute 22% higher energy savings in mild outdoor conditions compared with conventional fixed set-point PI control and outdoor air temperature reset control strategies.

In summary, it is noted that the majority of studies on hydronic space heating systems and solar-assisted heating systems have focused their attention on model development of components such as boilers and solar collectors. Furthermore, on a system level basis, the previous studies have dealt with stand-alone systems mostly dealing with radiant heating systems. In other words, they did not consider the integration of solar and boiler heating system in a multi-functional building. This entails the use of different water supply temperatures as opposed to single source supply water

temperature in the heating system. This adds to a new complexity in designing control strategies for such systems which are not addressed in the literature.

From the viewpoint of control studies, it is noted that PI control, adaptive control and optimal control techniques have been proposed for space heating systems. However, the application is limited to single zone buildings as opposed to multi-zone buildings. Furthermore, the hybrid nature of controls involving both on-off controls and adaptive controls in a multiple control loop system environments has not been studied. In addition, much less work is done on operation and control of systems involving the integration of the solar system into a conventional boiler heating system. This study addresses the limitation noted above. To this end, the primary objective of this thesis is to model a hydronic space heating system integrated with a sustainable solar energy system for a multi-zone multi-functional building, and also to develop improved control and operation strategies for this multiple control loop system and optimize the energy efficiency of the overall system.

CHAPTER 3 DYNAMIC MODEL OF A SOLAR-ASSISTED HYDRONIC SPACE HEATING SYSTEM

3.1 Introduction

In this chapter, the dynamic modeling and open loop tests of the hydronic space heating system are explored. First of all, the physical model of the system is described with a schematic diagram. After that, the dynamic models of each component are developed in sequence. These are the commercial and residential zones models, the building enclosure model, the terminal baseboard heater model, the radiant floor heating system model, the flat-plate solar collector model, the solar storage water tank model, the water-to-water heat exchanger model and the gas-fired boiler model. At the end of this chapter, the open loop test is conducted to simulate the dynamic responses of the integrated system under design day conditions.

3.2 The physical model of the system

A typical two-storey multi-functional building located in Montreal is considered in this thesis. Figure 3.2.1 shows the building orientation, size and zone layout for each floor. The first floor consists of two individual commercial zones, and each zone is heated by using the terminal baseboard heater heating system. For the second floor, it has four residential zones; the radiant floor heating system is installed in each residential zone. In total, six individual zones are considered in this thesis.
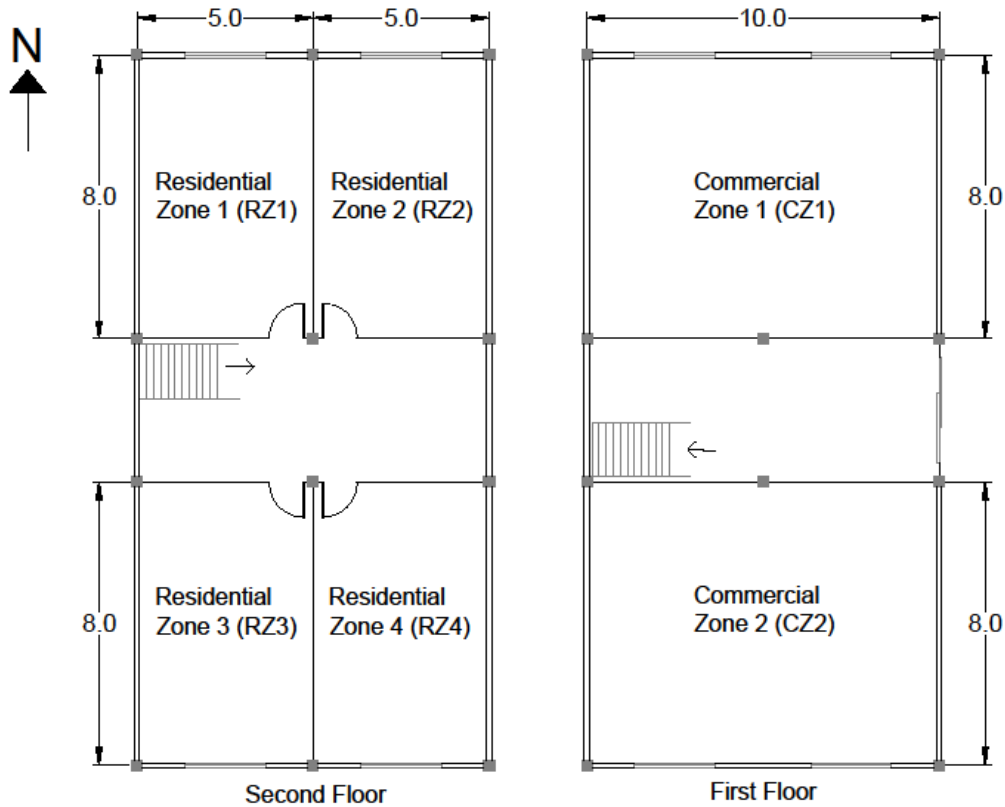
Figure 3.2.1 Commercial and residential floor zone layout

The schematic diagram of two kinds of heating systems is shown in Figure 3.2.2 and Figure 3.2.3, respectively. The base case system is a conventional gas-fuel boiler which can supply hot water to the baseboard heater for the first commercial floor and also to the radiant floor heating system of the second residential floor as shown in Figure 3.2.2. However, from the design aspect of view, the radiant floor heating system requires relatively-lower supply water temperature compared with the baseboard heater heating system. Therefore, a water-to-water boiler heat exchanger is designed to regulate the supply water temperature to the radiant floor system.
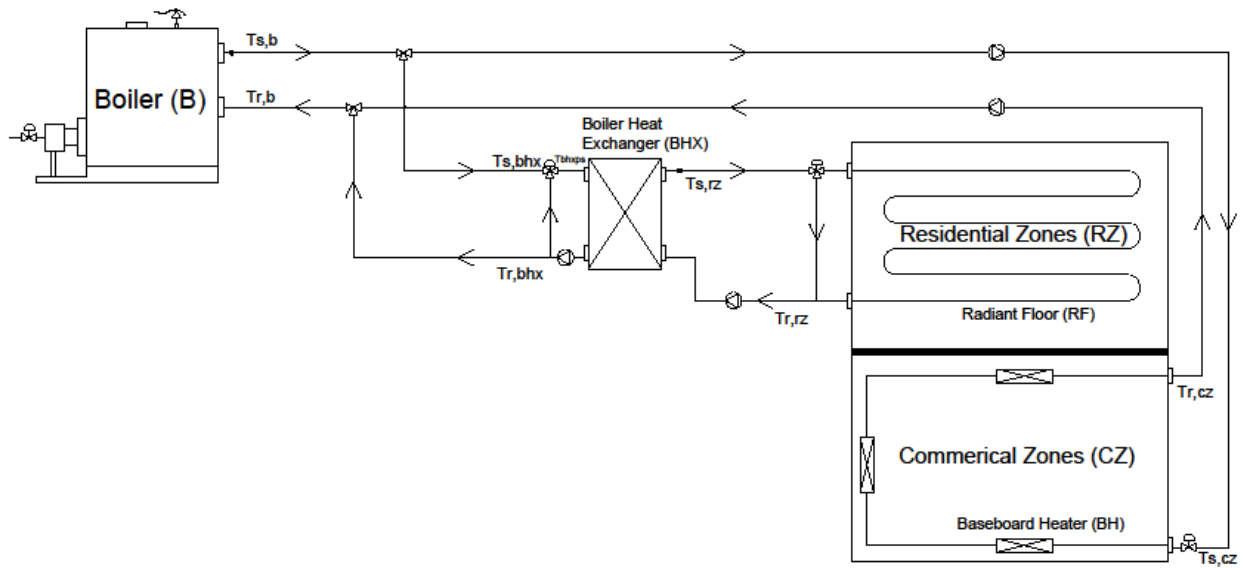
Figure 3.2.2 All boiler hydronic space heating system schematic diagram

On the other hand, from the energy efficiency point of view, it is not desirable to use high-quality heat (boiler heat source) for low-quality energy demand system (radiant floor heating system). In order to improve the overall system energy efficiency and to make the building more sustainable, free solar energy is considered as an appropriate heat resource for low-quality energy demand system (radiant floor system). Therefore, a more advanced system is proposed which adds in the liquid flat-plate solar collector, two heat exchangers and one water tank and working together with the conventional boiler heating system as shown in Figure 3.2.3. In this way, the radiant floor system return water can be heated first by using solar heat from the solar tank and then the boiler in case further heating is required. The detailed solar and entire system operation and control strategies will discuss in the next chapter.
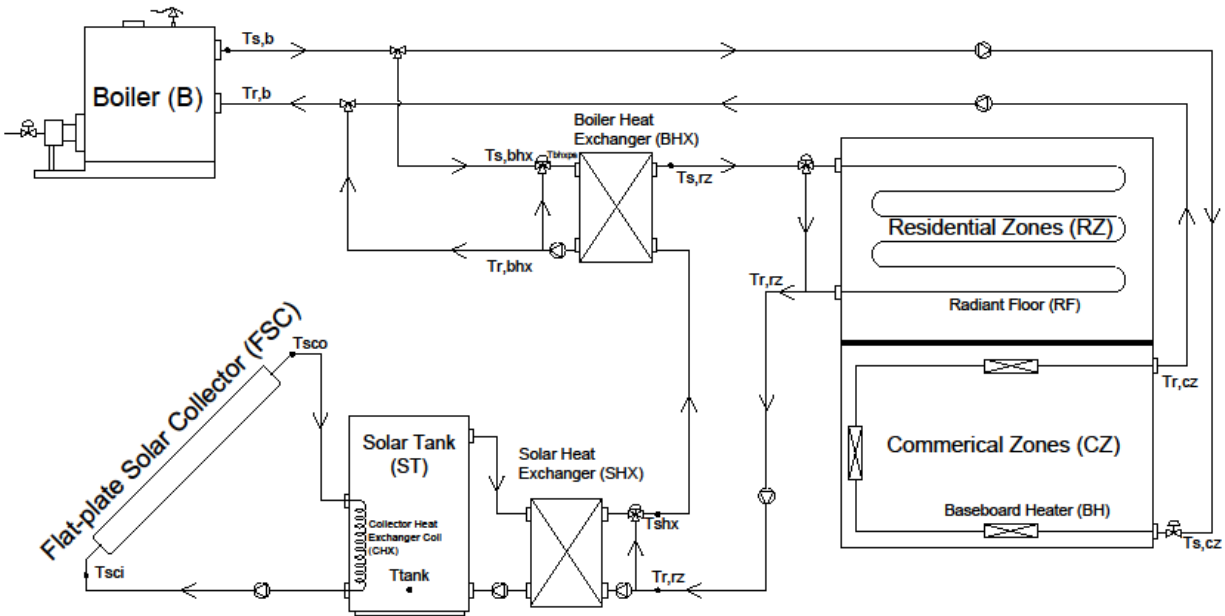
Figure 3.2.3 Solar-assisted hydronic space heating system schematic diagram

The overall system design and equipment selection consist of six main components: 1, zone heating load calculation. 2, commercial zones (CZ) baseboard heater (BH) sizing. 3, residential zones (RZ) radiant floor heating (RFH) system sizing. 4, flat-plate solar collector (FSC), solar tank (ST) and solar heat exchanger (SHX) sizing. 5, boiler heat exchanger (BHX) sizing. 6, gas-fired boiler (B) selection. The steady-state design method is applied to determine the capacity of each component. The summary of the calculation is presented in Appendix-A. The flat-plate solar collector was sized based on steady-state design calculations. The appropriate size of flat-plate solar collector modules was then selected from the manufacturer's catalogue data which is attached in Appendix-B.

3.3   The formulation of dynamic models

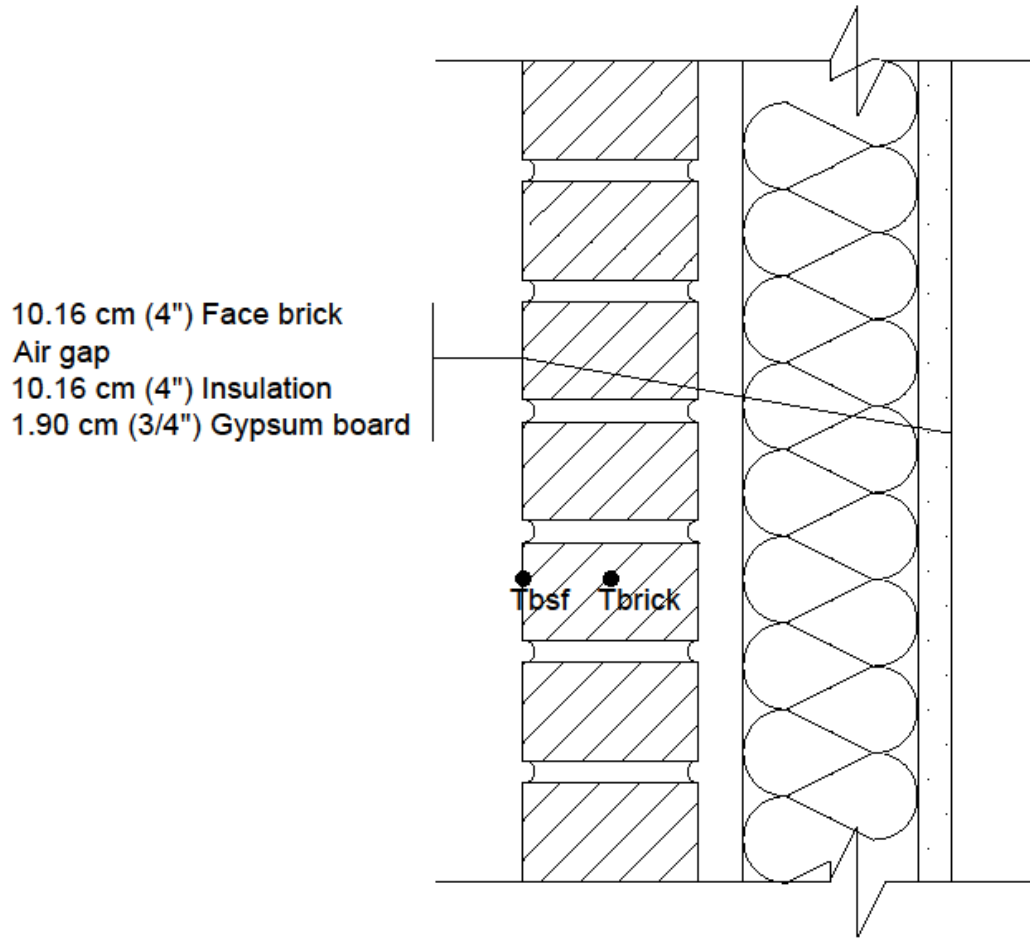### 3.3.1   Building enclosure model

Figure 3.3.1 Sectional view of the wall assembly

A sectional view of the exterior wall section is shown in Figure 3.3.1. The exterior wall consists of four main layers: a face brick, an air gap, an insulation and a gypsum board from exterior to interior. In order to simplify the model, the temperature distribution in each layer is assumed as uniform. Therefore, the heat transfer analysis of the exterior wall can be simply regarded as a one-dimensional situation. A two-node heat transfer model is developed for the exterior walls. One node is in the face bricklayer; another one is located on its exterior surface as

shown in Figure 3.3.1. By applying the energy conservation method for each node, the heat balance equations of the brick node and the temperature equation of brick surface node were expressed as below:

$$C_{brick} \frac{d(T_{brick})}{dt} = A_{wall} U_{w2} (T_{brick} - T_z) - A_{wall} U_{w1} (T_{brick} - T_{bsf}) \tag{3.1}$$

$$T_{bsf} = \frac{U_{w1} T_{brick} + h_o T_o + Q_{sol,inci}}{U_{w1} + h_o} \tag{3.2}$$

All mentioned symbols in the above equations, corresponding definitions and values are listed in the following Table 3.3.1.

Definition	Symbol	Value or Formula	Unit
Density of the face brick	d_{brick}	2002.3	kg/m3
Specific heat of the face brick	c_{brick}	750	J/kg °C
Thickness of the face brick	H_{brick}	0.1016	m
Thickness of the air gap	H_{ag}	0.0254	m
Thickness of the insulation	H_{ins}	0.1016	m
Thickness of the gypsum board	H_{gb}	0.019	m
Thermal conductivity of the face brick	K_{brick}	1.31	W/m °C

Thermal conductivity of the air gap	K_{ag}	0.024	W/m °C
Thermal conductivity of the insulation	K_{ins}	0.0975	W/m °C
Thermal conductivity of the gypsum board	K_{gb}	0.17	W/m °C
Exterior surface film conductance	h_o	17.1955	W/m^2 °C
Interior surface film conductance	h_i	8.23	W/m^2 °C
Heat transfer coefficient from brick node to surface node	U_{w1}	$$U_{w1} = \frac{1}{0.5 * H_{brick}/K_{brick}}$$	W/m^2 °C
Heat transfer coefficient from brick node to the indoor	U_{w2}	$$U_{w2} = \frac{1}{\frac{0.5 * H_{brick}}{K_{brick}} + \frac{H_{ag}}{K_{ag}} + \frac{H_{ins}}{K_{ins}} + \frac{H_{gb}}{K_{gb}} + 1/h_i}$$	W/m^2 °C

Table 3.3.1 Physical properties of the exterior wall assembly

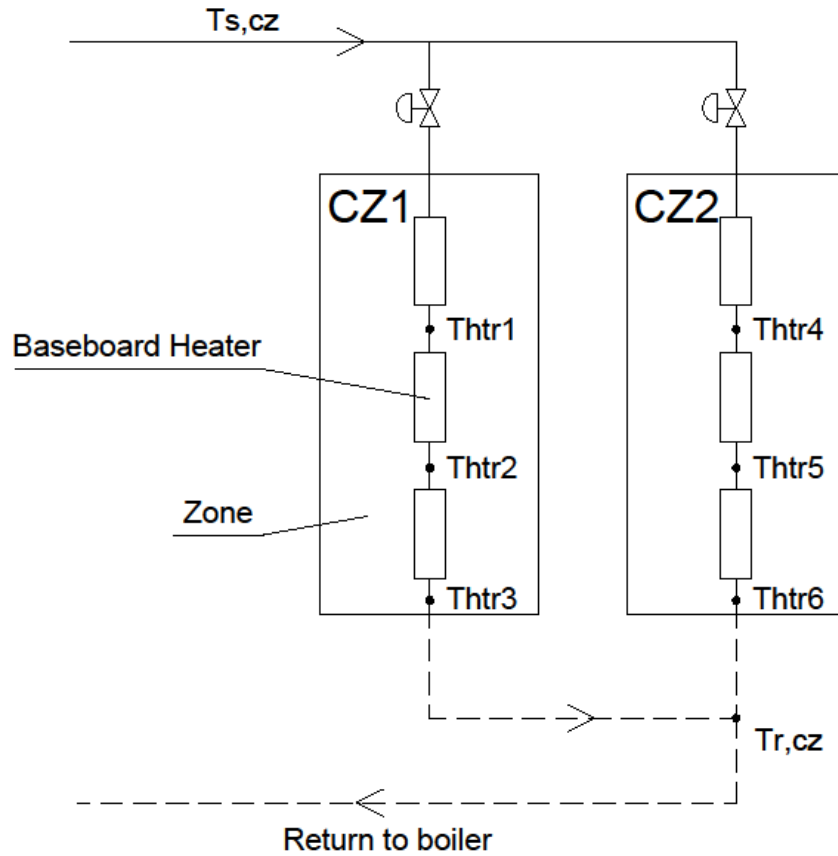### 3.3.2 Commercial zones model

Figure 3.3.2 Schematic diagram of the reversed return hot water heating system in

commercial zones

Figure 3.3.2 provides a schematic diagram of the reversed return hot water space heating system for two commercial zones. A mathematic model for simulating each commercial zone air temperature is developed by assuming the zone air temperature distribution is uniform. The rate of heat stored in the commercial zone air mass equals to the net heat transferred from the baseboard heater to zone air, the heat transferred between zone air and the outside environment through building enclosure and the infiltration. The heat balance equations and the water flow rates of two commercial zones indoor air are expressed as below:

$$C_{cz,1}\frac{d(T_{z,cz1})}{dt} = c_w m_{w,cz1}(T_{s,cz1} - T_{htr,3}) - A_{win,cz1}U_{win}(T_{z,cz1} - T_o)$$

$$- A_{wall,cz1}U_{w2}(T_{z,cz1} - T_{brick}) \tag{3.3}$$

$$- \frac{ACH_{cz1} * Vol_{cz1} * c_a * d_a * (T_{z,cz1} - T_o)}{3600} + Q_{int,cz1} + Q_{sol,cz1}$$

$$C_{cz,2}\frac{d(T_{z,cz2})}{dt} = c_w m_{w,cz2}(T_{s,cz2} - T_{htr,6}) - A_{win,cz2}U_{win}(T_{z,cz2} - T_o)$$

$$- A_{wall,cz2}U_{w2}(T_{z,cz2} - T_{brick}) \tag{3.4}$$

$$- \frac{ACH_{cz2} * Vol_{cz2} * c_a * d_a * (T_{z,cz2} - T_o)}{3600} + Q_{int,cz2} + Q_{sol,cz2}$$

$$m_{w,cz1} = u_{w,cz1}m_{w,cz1,d} \tag{3.5}$$

$$m_{w,cz2} = u_{w,cz2}m_{w,cz2,d} \tag{3.6}$$

3.3.3 Baseboard heaters model

The baseboard heater heating system is designed for the first-floor commercial zones. Following the approach described in [14], the model equations were derived. The rate of energy stored in the baseboard heater water tube is equal to the heat supply from the boiler hot water minus the heat transferred from the hot water and the zone environment. Equation 3.7 to 3.12 describe the heat transfer process for each baseboard heater.

$$C_{htr,1}\frac{d(T_{htr,1})}{dt} = c_w m_{w,cz1}(T_{s,cz1} - T_{htr,1}) - U_{htr,1}\left(\frac{T_{s,cz1} + T_{htr,1}}{2} - T_{z,cz1}\right)^{1+n} \tag{3.7}$$

$$C_{htr,2}\frac{d(T_{htr,2})}{dt} = c_w m_{w,cz1}(T_{htr,1} - T_{htr,2}) - U_{htr,2}\left(\frac{T_{htr,1} + T_{htr,2}}{2} - T_{z,cz1}\right)^{1+n} \tag{3.8}$$

$$C_{htr,3} \frac{d(T_{htr,3})}{dt} = c_w m_{w,cz1}(T_{htr,2} - T_{htr,3}) - U_{htr,3}\left(\frac{T_{htr,2} + T_{htr,3}}{2} - T_{z,cz1}\right)^{1+n} \tag{3.9}$$

$$C_{htr,4} \frac{d(T_{htr,4})}{dt} = c_w m_{w,cz2}(T_{s,cz2} - T_{htr,4}) - U_{htr,4}\left(\frac{T_{s,cz2} + T_{htr,4}}{2} - T_{z,cz2}\right)^{1+n} \tag{3.10}$$

$$C_{htr,5} \frac{d(T_{htr,5})}{dt} = c_w m_{w,cz2}(T_{htr,4} - T_{htr,5}) - U_{htr,5}\left(\frac{T_{htr,4} + T_{htr,5}}{2} - T_{z,cz2}\right)^{1+n} \tag{3.11}$$

$$C_{htr,6} \frac{d(T_{htr,6})}{dt} = c_w m_{w,cz2}(T_{htr,5} - T_{htr,6}) - U_{htr,6}\left(\frac{T_{htr,5} + T_{htr,6}}{2} - T_{z,cz2}\right)^{1+n} \tag{3.12}$$

Also, the commercial zone mixed return water temperature can be described as:

$$T_{r,cz} = \frac{m_{w,cz1}T_{htr,3} + m_{w,cz2}T_{htr,6}}{m_{w,cz1} + m_{w,cz2}} \tag{3.13}$$

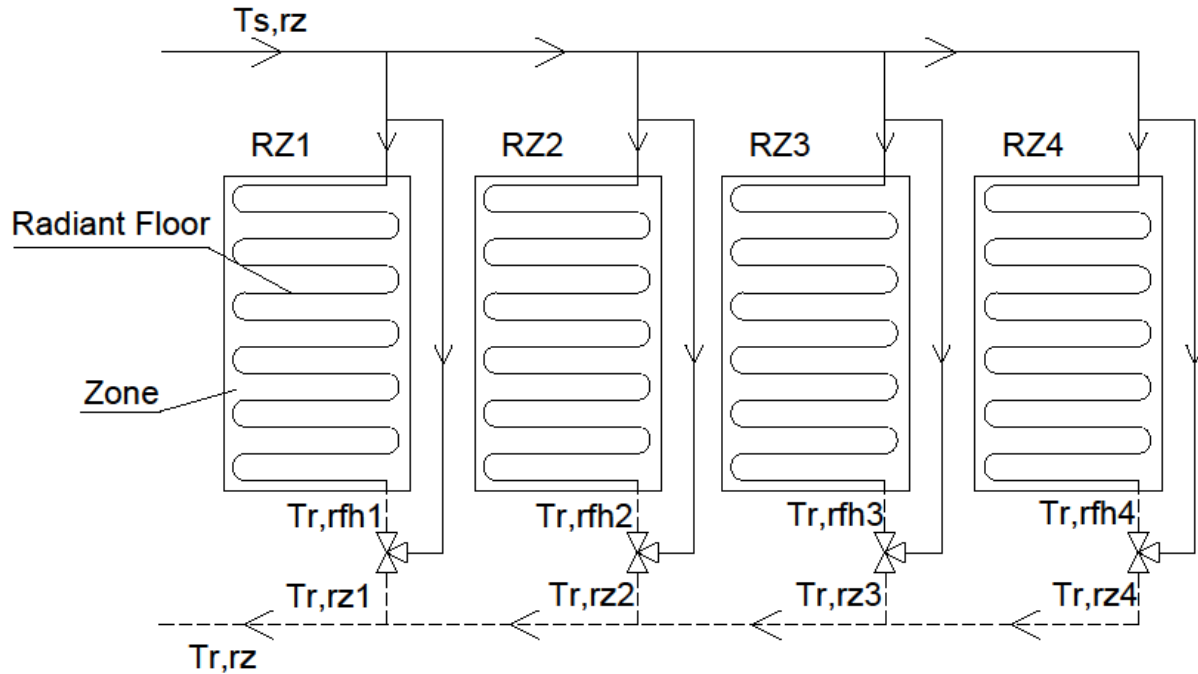### 3.3.4　Residential zones model

Figure 3.3.3 Schematic diagram of the radiant floor heating system in residential zones

Figure 3.3.3 shows the schematic diagram of the radiant floor heating system in residential zones. A model for simulating each residential zone air temperature is established by assuming the zone air temperature distribution is uniform. Therefore, the rate of heat stored in the residential zone air mass equals to the net heat transferred by the radiant floor through radiation and convection, the heat transferred between zone air and the outside environment through building enclosure and the air infiltration.

$$C_{rz,1}\frac{d(T_{z,rz1})}{dt} = Q_{rad,conv,1} - A_{win,rz1}U_{win}(T_{z,rz1} - T_o)$$

$$- A_{wall,rz1}U_{w2}(T_{z,rz1} - T_{brick}) - A_{rf,rz1}U_{rf}(T_{z,rz1} - T_o) \tag{3.14}$$

$$- \frac{ACH_{rz1} * Vol_{rz1} * c_a * d_a * (T_{z,rz1} - T_o)}{3600} + Q_{int,rz1} + Q_{sol,rz1}$$

$$C_{rz,2}\frac{d(T_{z,rz2})}{dt} = Q_{rad,conv,2} - A_{win,rz2}U_{win}(T_{z,rz2} - T_o)$$

$$- A_{wall,rz2}U_{w2}(T_{z,rz2} - T_{brick}) - A_{rf,rz2}U_{rf}(T_{z,rz2} - T_o) \tag{3.15}$$

$$- \frac{ACH_{rz2} * Vol_{rz2} * c_a * \rho_a * (T_{z,rz2} - T_o)}{3600} + Q_{int,rz2} + Q_{sol,rz2}$$

$$C_{rz,3}\frac{d(T_{z,rz3})}{dt} = Q_{rad,conv,3} - A_{win,rz3}U_{win}(T_{z,rz3} - T_o)$$

$$- A_{wall,rz3}U_{w2}(T_{z,rz3} - T_{brick}) - A_{rf,rz3}U_{rf}(T_{z,rz3} - T_o) \tag{3.16}$$

$$- \frac{ACH_{rz3} * Vol_{rz3} * c_a * \rho_a * (T_{z,rz3} - T_o)}{3600} + Q_{int,rz3} + Q_{sol,rz3}$$

$$C_{rz,4}\frac{d(T_{z,rz4})}{dt} = Q_{rad,conv,4} - A_{win,rz4}U_{win}(T_{z,rz4} - T_o)$$

$$- A_{wall,rz4}U_{w2}(T_{z,rz4} - T_{brick}) - A_{rf,rz4}U_{rf}(T_{z,rz4} - T_o) \tag{3.17}$$

$$- \frac{ACH_{rz4} * Vol_{rz4} * c_a * \rho_a * (T_{z,rz4} - T_o)}{3600} + Q_{int,rz4} + Q_{sol,rz4}$$

$$T_{r,rz1} = \frac{u_{w,rz1}m_{w,rz1,d}T_{r,rfh1} + (1 - u_{w,rz1})m_{w,rz1,d}T_{s,rz1}}{u_{w,rz1}m_{w,rz1,d} + (1 - u_{w,rz1})m_{w,rz1,d}} \tag{3.18}$$

$$T_{r,rz2} = \frac{u_{w,rz2}m_{w,rz2,d}T_{r,rfh2} + (1 - u_{w,rz2})m_{w,rz2,d}T_{s,rz2}}{u_{w,rz2}m_{w,rz2,d} + (1 - u_{w,rz2})m_{w,rz2,d}} \tag{3.19}$$

$$T_{r,rz3} = \frac{u_{w,rz3}m_{w,rz3,d}T_{r,rfh3} + (1 - u_{w,rz3})m_{w,rz3,d}T_{s,rz3}}{u_{w,rz3}m_{w,rz3,d} + (1 - u_{w,rz3})m_{w,rz3,d}} \tag{3.20}$$

$$T_{r,rz4} = \frac{u_{w,rz4} m_{w,rz4,d} T_{r,rfh4} + (1 - u_{w,rz4}) m_{w,rz4,d} T_{s,rz4}}{u_{w,rz4} m_{w,rz4,d} + (1 - u_{w,rz4}) m_{w,rz4,d}} \qquad (3.21)$$

$$T_{r,rz} = \frac{m_{w,cz1} T_{r,rz1} + m_{w,cz2} T_{r,rz2} + m_{w,cz3} T_{r,rz3} + m_{w,cz4} T_{r,rz4}}{m_{w,cz1,d} + m_{w,cz2,d} + m_{w,cz4,d} + m_{w,cz4,d}} \qquad (3.22)$$

3.3.5 Radiant floor heating system model

A plan view of the radiant floor heating panel is shown in Figure 3.3.4. Hot water circulating inside the tube transfers heat to the tube wall by convection, and then the tube wall transfers heat to its surrounding concrete through conduction in both horizontal and vertical directions. Besides, the hot water serpentine pipes are equally spaced, so it can be assumed that the same unit section is symmetrically repeated. Furthermore, the temperature gradient in the direction of the hot water pipes is considered as negligible. The temperature gradient in the direction of perpendicular to the panel is considered.
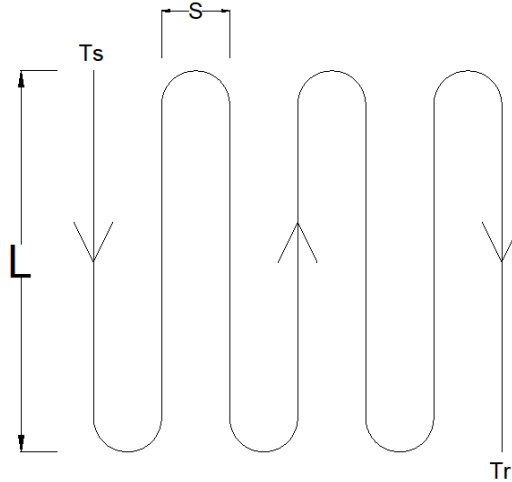

Figure 3.3.4 Plan view of an embedded tube for the radiant floor system

A sectional view of the radiant floor structure is shown in Figure 3.3.5. The radiant floor consists of three main layers: finish flooring layer, concrete slab layer and insulation layer. Besides, the serpentine tubes are embedded at the center of the concrete layer. The properties of each material are provided in Table 3.3.2.
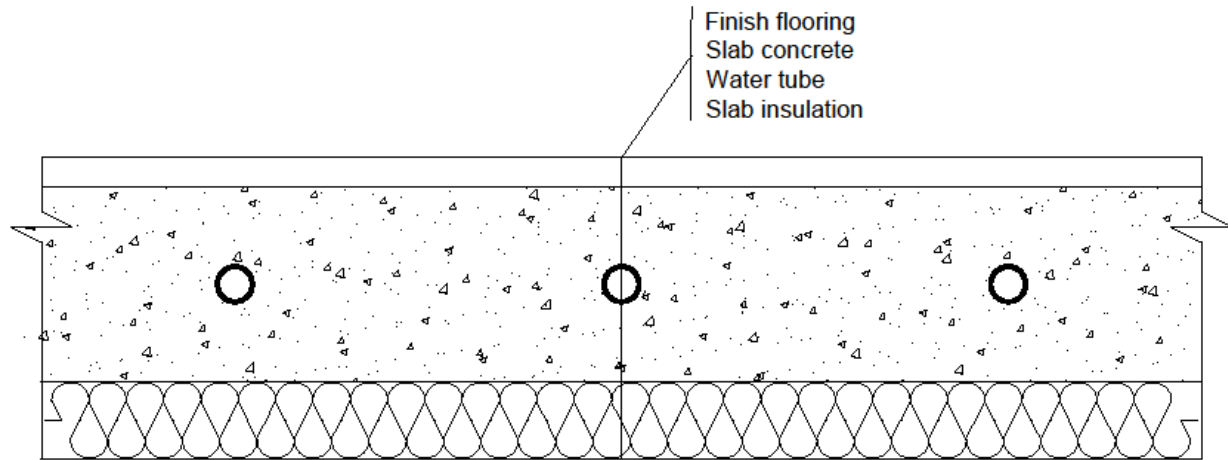

Figure 3.3.5 Sectional view of the concrete slab

A sectional view of the radiant floor nodes diagram is presented in Figure 3.3.6. The heat transfer analysis for the radiant floor system is considered as a two-dimensional situation [18]: heat flux from the water tube node to its nearby horizontal concrete nodes, and heat flux from the water tube node to its nearby vertical concrete nodes. It is also assumed that the nearby concrete nodes are at the same condition. Furthermore, it is assumed that the slab is well insulated. The heat transfer from the tube wall and the concrete to the insulation is considered as negligible. The governing equations of each node are described as below:
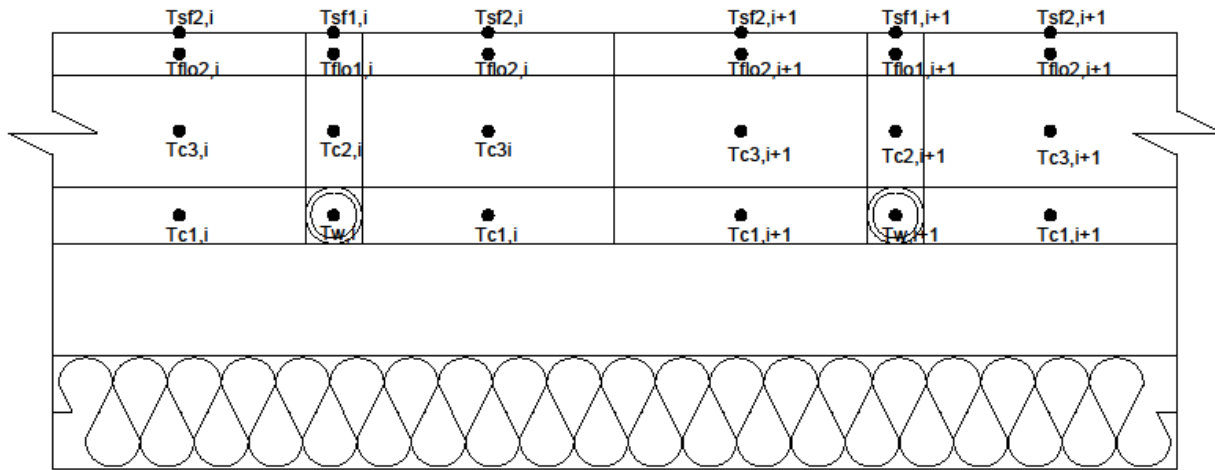
Figure 3.3.6 Radiant floor nodes diagram for two adjacent pipe sections

Where,

$T_{w,i}$ represents the water tube node temperature, °C

$T_{c1,i}$ represents the concrete node temperature around the tube in the water tube layer, °C

$T_{c2,i}$ represents the concrete node temperature above the tube in the concrete layer, °C

$T_{c3,i}$ represents the concrete node temperature around the $T_{c1,i}$ and $T_{c2,i}$ in the concrete layer, °C

$T_{flo1,i}$ represents the flooring node temperature above the tube in the flooring layer, °C

$T_{flo2,i}$ represents the flooring node temperature above the concrete in the flooring layer, °C

$T_{sf1,i}$ represents the surface node temperature above the tube, °C

$T_{sf2,i}$ represents the surface node temperature above the concrete, °C

The energy balance equation of the circulating water node can be described as:

$$C_{wt} * \frac{d(T_{w,i})}{dt} = c_w u_{w,rzi} m_{w,rzi,d} (T_{s,rz} - T_{w,i}) + 2U_{cond\_wc1}(T_{c1,i} - T_{w,i})$$
$$+ U_{cond\_wc2}(T_{c2,i} - T_{w,i}) \qquad (3.23)$$

The energy balance equation of the concrete temperature around the tube in water tube layer can be described as:

$$C_{c1} * \frac{d(T_{c1,i})}{dt} = 2U_{cond\_wc1}(T_{w,i} - T_{c1,i}) + U_{cond\_c1c3}(T_{c3,i} - T_{c1,i}) \qquad (3.24)$$

The energy balance equation of the concrete temperature above tube in concrete tube layer can be described as:

$$C_{c2} * \frac{d(T_{c2,i})}{dt} = U_{cond\_wc2}(T_{w,i} - T_{c2,i}) + 2U_{cond\_c2c3}(T_{c3,i} - T_{c2,i})$$
$$+ U_{cond\_c2f1}(T_{flo1,i} - T_{c2,i}) \qquad (3.25)$$

The energy balance equation of the concrete temperature in the concrete layer can be described as:

$$C_{c3} * \frac{d(T_{c3,i})}{dt} = 2U_{cond\_c2c3}(T_{c2,i} - T_{c3,i}) + U_{cond\_c1c3}(T_{c1,i} - T_{c3,i})$$
$$+ U_{cond\_c3f2}(T_{flo2,i} - T_{c3,i}) \qquad (3.26)$$

The energy balance equation of flooring temperature above tube in flooring layer can be described as:

$$C_{flo1} * \frac{d(T_{flo1,i})}{dt}$$

$$= U_{cond\_c2f1}(T_{c2,i} - T_{flo1,i}) + 2U_{cond\_f1f2}(T_{flo2,i} - T_{flo1,i}) \tag{3.27}$$

$$+ U_{cond\_f1sf1}(T_{sf1,i} - T_{flo1,i})$$

The energy balance equation of flooring temperature above concrete in flooring layer can be described as:

$$C_{flo2} * \frac{d(T_{flo2,i})}{dt}$$

$$= U_{cond_{c3f2}}(T_{c3,i} - T_{flo2,i}) + 2U_{cond_{f1f2}}(T_{flo1,i} - T_{flo2,i}) \tag{3.28}$$

$$+ U_{cond\_f2sf2}(T_{sf2i} - T_{flo2,i})$$

The energy balance equation of surface temperature above the tube can be described as:

$$T_{sf1,i} = T_{flo1,i} - \left(\frac{q_{r1,i}}{U_{cond\_f1sf1}}\right) - \left(\frac{q_{c1,i}}{U_{cond\_f1sf1}}\right) \tag{3.29}$$

The energy balance equation of surface temperature above concrete can be described as:

$$T_{sf2,i} = T_{flo2,i} - \left(\frac{q_{r2,i}}{U_{cond\_f2sf2}}\right) - \left(\frac{q_{c2,i}}{U_{cond\_f2sf2}}\right) \tag{3.30}$$

Heat transfer due to the radiation and convention between the floor surface and zone environment on the top of tube node can be described as:

$$q_{r1,i} = 5 \times 10^8 F_{en}A_1\left((T_{sf1,i} + 273)^4 - (T_{en,rzi} + 273)^4\right) \tag{3.31}$$

$$q_{c1,i} = 2.17A_1(T_{sf1,i} - T_{z,rzi})^{1.31} \tag{3.32}$$

Heat transfer due to the radiation and convention between the floor surface and zone environment on the top of a concrete node can be described as:

$$q_{r2,i} = 5 \times 10^8 F_{en} A_2 \left((T_{sf2,i} + 273)^4 - (T_{en,rzi} + 273)^4 \right) \tag{3.33}$$

$$q_{c2,i} = 2.17 A_2 (T_{sf2,i} - T_{z,rzi})^{1.31} \tag{3.34}$$

So the total radiative and convective heat transfer from the radiant floor to the zone air can be expressed as:

$$Q_{rad,conv,i} = \sum_{i=1}^{n} (q_{r1,i} + q_{c1,i} + q_{r2,i} + q_{c2,i}) \tag{3.35}$$

All mentioned symbols in the above equations, corresponding definitions and values are listed in the following Table 3.3.1 and in Appendix A.

Definition	Symbol	Value or Formula	Unit
Thermal conductivity of the tube	K_t	0.38	W/m °C
Thermal conductivity of the concrete	K_c	2.4	W/m °C
Thermal conductivity of the flooring	K_{flo}	0.17	W/m °C
Density of the concrete	d_c	2242	kg/m3
Density of the flooring	d_{flo}	70	kg/m3
Specific heat of the concrete	c_c	750	J/kg °C
Specific heat of the flooring	c_{flo}	120	J/kg °C
Prandtl number of water	P_r	3.91	-
Dynamic viscosity	vs	$0.596*10^{-3}$	kg/m s
Nusselt number	N_u	$N_u = 0.023 Re^{0.8} P_r^{0.3}$	-
Thermal resistance of the tube wall	R_{cond_t}	$R_{cond\_t} = \dfrac{\ln(\frac{D_o}{D_i})}{2\pi K_t}$	m °C /W

Thermal resistance between water and tube wall due to convection	R_{conv_wt}	$R_{conv\_wt} = \dfrac{1}{N_u \pi k_w}$	m °C /W
Thermal resistance between tube wall and its horizontal concrete node $T_{c1,i}$	R_{cond_tc1}	R_{cond_tc1} $= \dfrac{0.25(S - D_o)}{D_o k_c}$	m °C /W
Thermal resistance between tube wall and its vertical concrete node $T_{c2,i}$	R_{cond_tc2}	R_{cond_tc2} $= \dfrac{0.5(H_c - D_o)}{D_o k_c}$	m °C /W
Thermal conductance between water node $T_{w,i}$ and its horizontal concrete node $T_{c1,i}$	R_{cond_wc1}	R_{cond_wc1} $= R_{cond\_t} + R_{conv\_wt}$ $+ R_{cond\_tc1}$	m °C /W
Thermal conductance between water node $T_{w,i}$ and its vertical concrete node $T_{c2,i}$	R_{cond_wc2}	R_{cond_wc2} $= R_{cond\_t} + R_{conv\_wt}$ $+ R_{cond\_tc2}$	m °C /W
Thermal conductance between water node $T_{w,i}$ and its horizontal concrete node $T_{c1,i}$	U_{cond_wc1}	U_{cond_wc1} $= \dfrac{1}{R_{cond\_wc1}}$	W/ m °C
Thermal conductance between water node $T_{w,i}$ and its vertical concrete node $T_{c2,i}$	U_{cond_wc2}	U_{cond_wc2} $= \dfrac{1}{R_{cond\_wc2}}$	W/ m °C
Thermal resistance between concrete nodes $T_{c1,i}$ and $T_{c3,i}$	R_{cond_c1c3}	R_{cond_c1c3} $= \dfrac{0.5H_c}{0.5(S - D_o)k_c}$	m °C /W

Thermal resistance between concrete nodes $T_{c2,i}$ and $T_{c3,i}$	R_{cond_c2c3}	R_{cond_c2c3} $= \dfrac{0.25(S + D_o)}{0.5 H_c k_c}$	m °C /W
Thermal conductance between concrete nodes $T_{c1,i}$ and $T_{c3,i}$	U_{cond_c1c3}	U_{cond_c1c3} $= \dfrac{1}{R_{cond\_c1c3}}$	W/ m °C
Thermal conductance between concrete nodes $T_{c2,i}$ and $T_{c3,i}$	U_{cond_c2c3}	U_{cond_c2c3} $= \dfrac{1}{R_{cond\_c2c3}}$	W/ m °C
Thermal resistance between concrete node $T_{c2,i}$ and floor node $T_{flo1,i}$	R_{cond_c2f1}	R_{cond_c2f1} $= \dfrac{0.5(H_c - D_o)}{D_o k_c}$ $+ \dfrac{0.5 H_{flo}}{D_o k_{flo}}$	m °C /W
Thermal resistance between concrete node $T_{c3,i}$ and floor node $T_{flo2,i}$	R_{cond_c3f2}	R_{cond_c3f2} $= \dfrac{0.5(H_c - D_o)}{0.5(S - D_o)k_c}$ $+ \dfrac{0.5 H_{flo}}{0.5(S - D_o)k_{flo}}$	m °C /W
Thermal conductance between concrete node $T_{c2,i}$ and its vertical floor node $T_{flo1,i}$	U_{cond_c2f1}	U_{cond_c2f1} $= \dfrac{1}{R_{cond\_c2f1}}$	W/ m °C

Thermal conductance between concrete node $T_{c3,i}$ and its vertical floor node $T_{flo2,i}$	U_{cond_c3f2}	U_{cond_c3f2} $$= \frac{1}{R_{cond\_c3f2}}$$	W/ m °C
Thermal resistance between floor nodes $T_{flo1,i}$ and $T_{flo2,i}$	R_{cond_f1f2}	R_{cond_f1f2} $$= \frac{0.25(S + D_o)}{H_{flo}k_{flo}}$$	m °C /W
Thermal conductance between floor nodes $T_{flo1,i}$ and $T_{flo2,i}$	U_{cond_f1f2}	U_{cond_f1f2} $$= \frac{1}{R_{cond\_f1f2}}$$	W/ m °C
Thermal resistance between floor node $T_{flo1,i}$ and its vertical surface node $T_{sf1,i}$	R_{cond_f1sf1}	$R_{cond\_f1sf1} = \frac{0.5H_{flo}}{D_o k_{flo}}$	m °C /W
Thermal resistance between floor node $T_{flo2,i}$ and its vertical surface node $T_{sf2,i}$	R_{cond_f2sf2}	R_{cond_f2sf2} $$= \frac{0.5H_{flo}}{0.5(S - D_o)k_{flo}}$$	m °C /W
Thermal conductance between floor node $T_{flo1,i}$ and its vertical surface node $T_{sf1,i}$	U_{cond_f1sf1}	U_{cond_f1sf1} $$= \frac{1}{R_{cond\_f1sf1}}$$	W/ m °C
Thermal conductance between floor node $T_{flo2,i}$ and its vertical surface node $T_{sf2,i}$	U_{cond_f2sf2}	U_{cond_f2sf2} $$= \frac{1}{R_{cond\_sf2f2}}$$	W/ m °C

Thermal capacity of the water inside the tube node $T_{w,i}$	C_{wt}	$C_{wt} = \dfrac{D_i{}^2}{4}\pi d_w c_w$	J/C m
Thermal capacity of the concrete node $T_{c1,i}$	C_{c1}	C_{c1} $= 0.5(S - D_o)D_o d_c c_c$	J/C m
Thermal capacity of the concrete node $T_{c2,i}$	C_{c2}	C_{c2} $= 0.5(H_c$ $- D_o)D_o d_c c_c$	J/C m
Thermal capacity of the concrete node $T_{c3,i}$	C_{c3}	C_{c3} $= 0.5(S - D_o)0.5(H_c$ $- D_o)d_c c_c$	J/C m
Thermal capacity of the floor node $T_{flo1,i}$	C_{flo1}	C_{flo1} $= H_{flo}D_o d_{flo} c_{flo}$	J/C m
Thermal capacity of the floor node $T_{flo2,i}$	C_{flo2}	C_{flo2} $= 0.5(S$ $- D_o)H_{flo}d_{flo}c_{flo}$	J/C m

Table 3.3.2 Physical properties of the radiant floor heating system

3.3.6 Solar system model

A sectional view of the collector module is shown in Figure 3.3.7. This flat-plate solar collector consists of seven main parts: an outer glass cover, an air gap between two glass covers, an inner glass cover, another air gap between the inner glass and absorber plate, an absorber coating plate, water circulating tube and insulation.
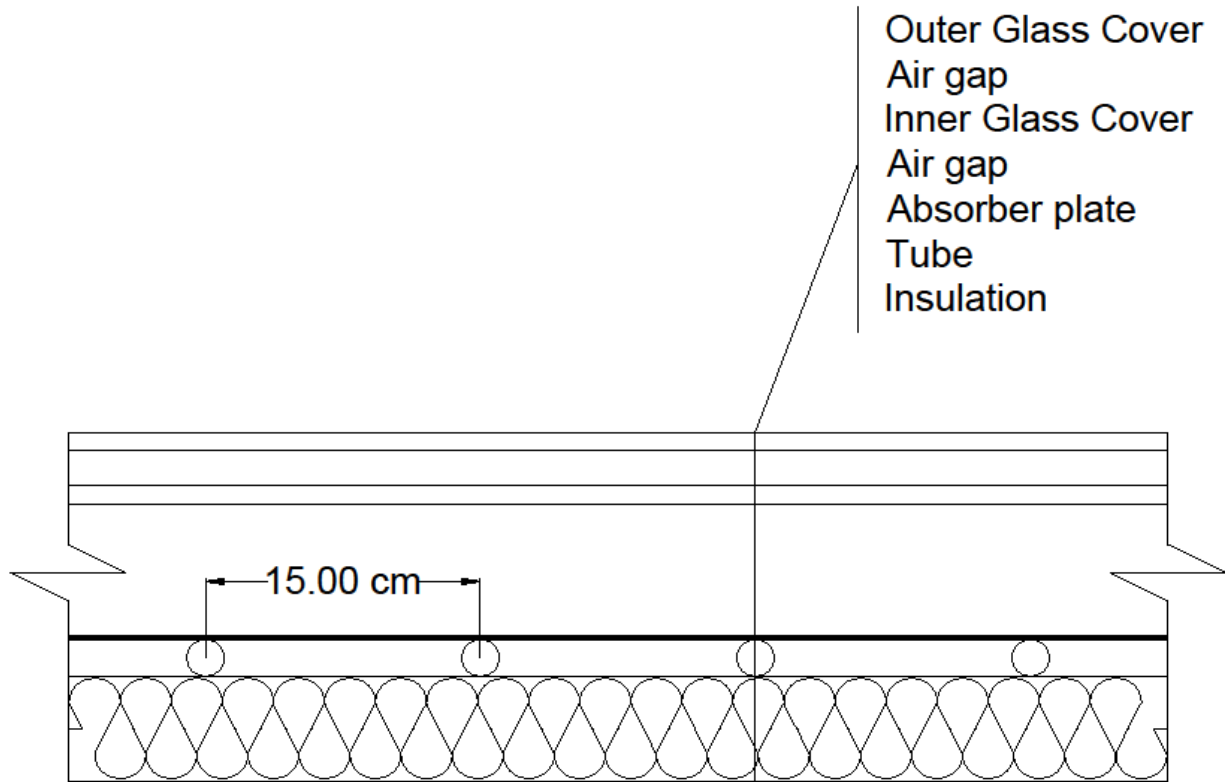
Figure 3.3.7 Sectional view of the flat-plate solar collector

The rate of heat loss from a flat-plate solar collector to surrounding environment depends on the overall heat loss transfer coefficient U_{sc}. An empirical equation for calculating the flat-plate solar collector overall heat loss coefficient is described as [6]:

$$U_{sc} = \left(\frac{N}{\frac{C}{T_{pm}} \left[\frac{(T_{pm} - T_o)}{(N + f)} \right]^e} + \frac{1}{h_{wind}} \right)^{-1}$$

(3.36)

$$+ \frac{\sigma (T_{pm} + T_o)(T_{pm}^2 + T_o^2)}{\frac{1}{\varepsilon_p + 0.00591 * N * h_{wind}} + \frac{2N + f - 1 + 0.133\varepsilon_p}{\varepsilon_g} - N}$$

In order to calculate the actual useful energy gain of a solar collector, except determining the overall heat loss coefficient, several related factors need to be defined as well. The fin

efficiency factor F is related with collector geometry shown in Figure 3.3.7. The equation for calculating fin efficiency factor can be expressed as:

$$M = \sqrt{\frac{U_{sc}}{k_p * \delta_p}} \tag{3.37}$$

$$F = \frac{tanh[M(W_{sc} - D_{o,sc})/2]}{M(W_{sc} - D_{o,sc})/2} \tag{3.38}$$

After determining the collector overall heat loss coefficient U_{sc} and fin efficiency factor F, the collector efficiency factor F′ is described as below which is related with internal heat transfer coefficient:

$$F' = \frac{1/U_{sc}}{W_{sc}\left[\frac{1}{U_{sc}[D_{sc} + (W_{sc} - D_{o,sc})F]} + \frac{1}{C_{bond}} + \frac{1}{\pi D_{i,sc}h_f}\right]} \tag{3.39}$$

Furthermore, the actual useful energy gain of a solar collector is affected by the mass flow rate. The equation for determining the collector heat removal factor F_R is described as:

$$F_R = \frac{m_{sc}C_p}{A_{sc}U_{sc}}\left[1 - exp\left(-\frac{A_{sc}U_{sc}F'}{m_{sc}C_f}\right)\right] \tag{3.40}$$

Therefore, the actual useful energy gain q_{sc} in a flat-plate solar collector can be written as below which is a widely used relationship for simulating collector useful energy gain and is generally known as the "Hottel-Whillier-Bliss" equation [6]. The actual useful energy gain is a function of the collector heat removal factor, the inlet fluid temperature of the collector and the ambient temperature. The equation is expressed as below:

$$q_{sc} = A_{sc}F_R[I\tau\alpha - U_{sc}(T_{sci} - T_o)] \tag{3.41}$$
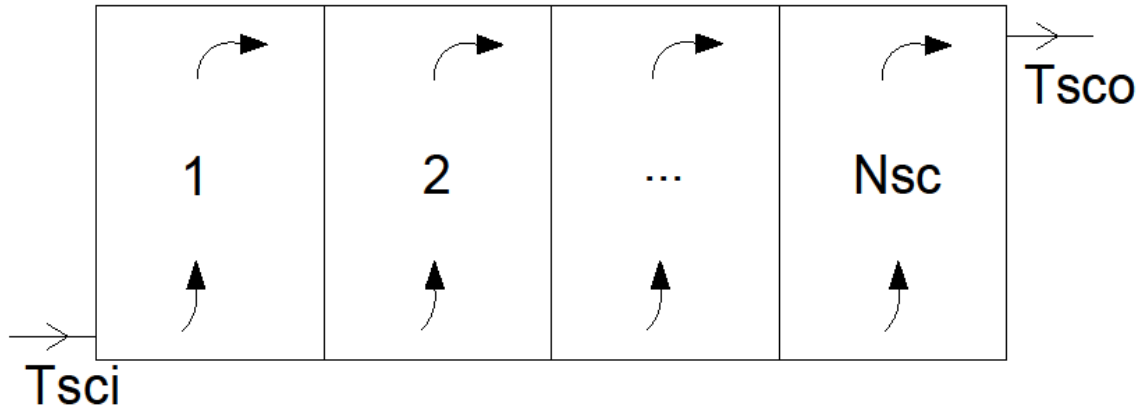
Figure 3.3.8 Collectors' array in parallel connection

Figure 3.3.8 shows arrays of N_{sc} modules with parallel connection. Assume for all flat-plate collector modules are identical, the performance of each module will be the same. Therefore, for flat-plate collector modules in parallel connection, the total useful energy gain q_{sct} can be determined from:

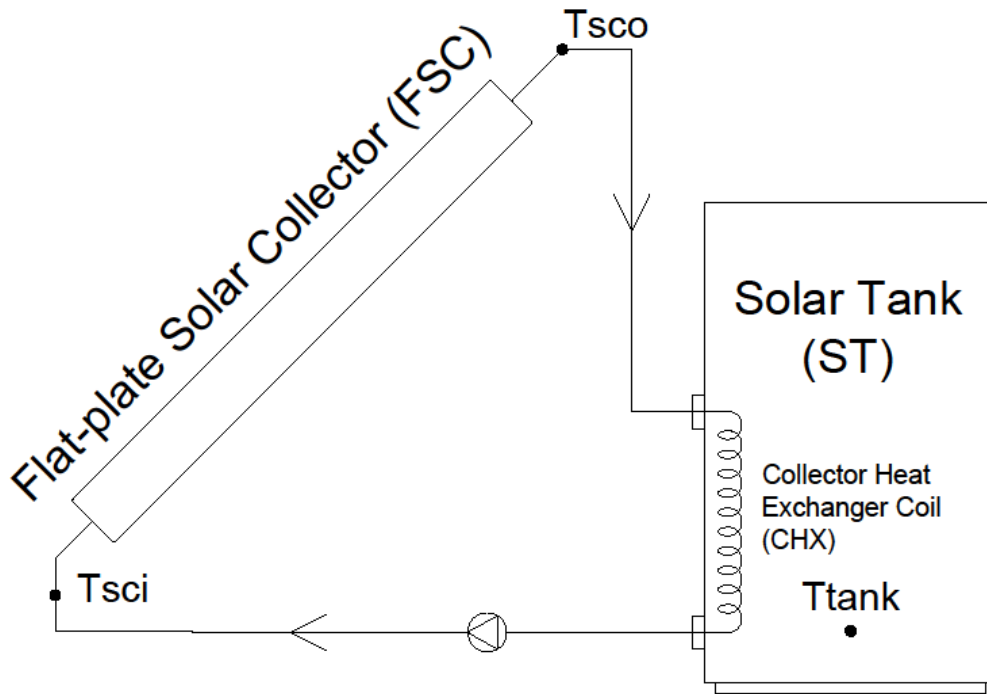$$q_{sct} = A_{sc}N_{sc}F_R[I\tau\alpha - U_{sc}(T_{sci} - T_o)] \tag{3.42}$$

Figure 3.3.9 Flat-plate solar collector with a heat exchanger coil in the tank

Therefore, the dynamic equation of flat-plate solar collector outlet temperature can be expressed as:

$$C_{sct}\frac{d(T_{sco})}{dt} = q_{sct} - c_f m_{sct}(T_{sco} - T_{sci}) \tag{3.43}$$

There is very often a collector heat exchanger between the solar collector and the thermal storage tank when antifreeze is used in the collector. The schematic diagram of a collector with coil heat exchanger and storage tank is shown in Figure 3.3.9. The combination of a collector and a coil heat exchanger performs exactly like a collector alone but with a reduced value of F_R'. The equation for calculating F_R' is expressed as below:

$$\frac{F_R'}{F_R} = \left[1 + \left(\frac{A_{sc}U_{sc}F_R}{m_{sct}C_f}\right) * \left(\frac{1}{\varepsilon} - 1\right)\right]^{-1} \tag{3.44}$$

Then, the solar collector equation and the coil heat exchanger equation are combined into a single equation that has the same form as the collector expression alone. The rewritten useful energy gain in a flat-plate solar collector combining with a heat exchanger can be expressed as:

$$q_{useful} = A_{sc}N_{sc}F_R'[I\tau\alpha - U_{sc}(T_{tank} - T_o)] \tag{3.45}$$

The solar tank which located between the collector and zone plays an essential role in the entire hydronic heating system. The volume for the solar tank is based on a recommendation from Duffie and Beckman (2013). The dynamic equation of unstratified solar tank is expressed as:

$$C_{tank}\frac{d(T_{tank})}{dt}$$
$$= q_{useful} - m_{w,shxp}C_w(T_{tank} - T_{shxpr}) - U_{tank}A_{tank}(T_{tank} \tag{3.46}$$
$$- T_a)$$

All mentioned symbols in the above equations, corresponding definitions and values are listed in the following Table 3.3.3 and Appendix A.

Definition	Symbol	Value or Formula	Unit
Number of glass covers	N	2	-
-	f	$f = (1 + 0.089h_{wind} - 0.1166h_{wind}\varepsilon_p) * (1 + 0.07866N)$	-
-	C	$C = 520(1 - 0.000051\beta^2)$	-

-	e	$e = 0.430\left(1 - \dfrac{100}{T_{pm}}\right)$	-
Emittance of absorber plate	ε_p	0.95	-
Emittance of glass cover	ε_g	0.88	-
Mean plate temperature	T_{pm}	50	°C
Wind heat transfer coefficient	h_{wind}	10	W/m² °C
Absorber plate thermal conductivity	k_p	385	W/m °C
Absorber plate thickness	δ_p	0.5	mm
Bond conductance	C_{bond}	∞	-
Heat transfer coefficient between the working fluid and tube wall	h_f	$h_f = \dfrac{Nu * k_f}{D_{sc}}$	W/m² °C
Nusselt number	Nu	$Nu = 4.4 + \dfrac{0.00236\left(RePr\dfrac{D_h}{L}\right)^{1.66}}{1 + 0.00857\left(RePr\dfrac{D_h}{L}\right)^{1.13}}$	-
Reynold number	Re	$Re = \dfrac{d_f * v_f * D_h}{\mu_f}$	-
Density of working fluid	d_f	1055	kg/m³
Hydraulic diameter	D_h	$D_h = \dfrac{4A_{riser}}{p_{riser}}$	m
Dynamic viscosity	μ_f	$2.32*10^{-3}$	kg/m s

Perimeter of riser tube	p_{riser}	$p_{riser} = \pi D_{sc}$	m
Prandtl number	Pr	4.83	-
Solar radiation intensity	I	-	W/m^2
Transmission coefficient of glass cover	τ	0.895	-
Absorption coefficient of absorber plate	α	0.95	-
Specific heat of antifreeze	c_f	3850	J/kg K
Specific heat of water	c_w	4187	J/kg K

Table 3.3.3 Physical properties of the flat-plate solar collector

3.3.7   Heat exchanger model

Two water to water tube heat exchangers are installed in the entire system. The first one is located between the boiler and residential zones which is used for heating the radiant floor system return water in case of the solar system is completely off, or the solar energy is not sufficient. The next heat exchanger is placed between the solar tank and residential zones. The purpose of installing this solar heat exchanger is to heat the radiant floor system return water by using hot water in the solar tank.

The dynamic equations of two water-to-water heat exchangers primary (hot) and secondary side (cold) temperatures are described in below. The rate of heat stored in the primary side is equal to heat supplied from hot source minus the heat transferred to the secondary side. On the other

hand, the rate of heat stored in the secondary side is equal to heat transferred from the primary side minus the heat absorbed by the cold source.

$$C_{hxp} \frac{d(T_{o,hxp})}{dt} = c_w m_{w,hxp}(T_{i,hxp} - T_{o,hxp}) - q_{hx} \tag{3.47}$$

$$C_{hxs} \frac{d(T_{o,hxs})}{dt} = q_{hx} - c_w m_{w,hxs}(T_{o,hxs} - T_{i,hxs}) \tag{3.48}$$

The working equation of the heat exchanger heat transfer rate q_{hx} is defined in below equation, where $T_{i,hxp}$ and $T_{i,hxs}$ are the hot fluid inlet and cold fluid inlet temperatures respectively, and $m_{hx}C_{p_{min}}$ is the lower of two capacitance rates [6].

$$q_{hx} = \epsilon (m_{hx}C_p)_{min}(T_{i,hxp} - T_{i,hxs}) \tag{3.49}$$

For a counter-flow exchanger, the effectiveness ϵ is given by

If $C^* \neq 1$

$$\epsilon = \frac{1 - e^{-NTU(1-C^*)}}{1 - C^* * e^{-NTU(1-C^*)}} \tag{3.50}$$

If $C^* = 1$

$$\epsilon = \frac{NTU}{1 + NTU} \tag{3.51}$$

Where NTU is the number of transfer units, it is defined in below equation. UA is the overall heat transfer coefficient-area.

$$NTU = \frac{UA_{hx}}{(m_{hx}C_p)_{min}} \tag{3.52}$$

Besides, the dimensionless capacitance rate is calculated by

$$C^* = \frac{(m_{hx}C_p)_{min}}{(m_{hx}C_p)_{max}} \tag{3.53}$$

3.3.8 Boiler model

A gas-fired condensing boiler is considered in this thesis. The supply water temperature of a boiler is a function of boiler capacity, boiler efficiency, supply and return water flow rate and the rate of fuel consumption. The energy balance equation of the boiler can be expressed as [14]:

$$C_b \frac{d(T_{s,b})}{dt} = u_f m_{fmax} * HV * e_b - m_{w,b} c_w (T_{s,b} - T_{r,b}) - a_j (T_{s,b} - T_a) \tag{3.54}$$

The boiler return water temperature can be described as:

$$T_{r,b} = \frac{m_{wr,hxp} T_{r,bhxb} + m_{wr,cz} T_{r,czb}}{m_{wr,hxp} + m_{wr,cz}} \tag{3.55}$$

3.3.9 Heat losses from pipes in the distribution system

The heat losses due to the water distribution system are evaluated based on the boiler supply water temperature, ground temperature, supply and return water flow rate, pipe insulation and the total pipe length. The pipe segments related with pipe heat losses are from the boiler to the commercial zones, from the commercial zones back to the boiler, from the boiler to boiler heat exchanger and from boiler heat exchanger back to the boiler. For the rest of the pipe segments, the heat losses are considered as negligible.

$$C_{pipe,bcz} \frac{d(T_{s,cz})}{dt} = c_w m_{w,cz} (T_{s,b} - T_{s,cz}) - U_{pipe,loss,bcz} (T_{s,b} - T_{ground}) \tag{3.56}$$

$$C_{pipe,czb} \frac{d(T_{r,czb})}{dt} = c_w m_{w,cz}(T_{r,cz} - T_{r,czb}) - U_{pipe,loss,czb}(T_{r,cz} - T_{ground}) \qquad (3.57)$$

$$C_{pipe,bbhx} \frac{d(T_{s,bhx})}{dt}$$

$$= c_w m_{w,bhx}(T_{s,b} - T_{s,bhx}) - U_{pipe,loss,bbhx}(T_{s,b} - T_{ground}) \qquad (3.58)$$

$$C_{pipe,bhxb} \frac{d(T_{r,bhxb})}{dt}$$

$$= c_w m_{w,cz}(T_{r,bhx} - T_{r,bhxb}) \qquad (3.59)$$

$$- U_{pipe,loss,bhxb}(T_{r,bhx} - T_{ground})$$

3.4   Open loop test simulation

All individual components described above are integrated to build the overall system model. The open loop test is conducted to study the dynamic responses of the entire system by using the MATLAB program. The simulated results at design condition are presented in Figure 3.4.1 and 3.4.2 respectively. All design condition parameters are provided in Appendix-A Table.
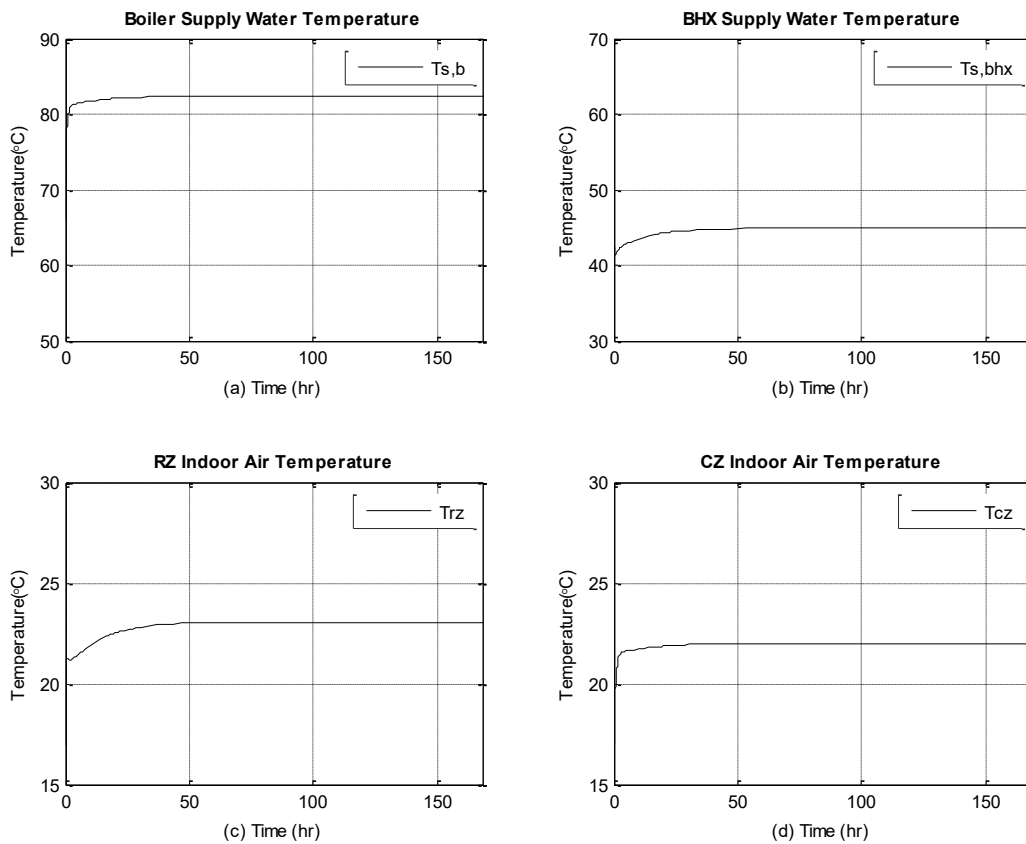
Figure 3.4.1 Open-loop test of supply water and zone temperatures at design condition

The simulation process starts from assumed initial conditions. As shown in the Figure 3.4.1 (a) and (b), the boiler and boiler heat exchanger (BHX) supply water temperatures can reach their steady state temperature at 83°C and 45°C respectively. Based on Figure 3.4.1 (c) and (d), the residential zone (RZ) and commercial zone (CZ) indoor air temperatures reach their steady state temperature of about 23°C and 22°C respectively. However, it is noted that the residential zones air temperature takes longer to reach steady state compared with commercial zones air temperatures. This is because the response time is affected by the thermal capacity of the system components. The main reason causing the slow response time is the radiant floor heating system

in the residential zones which has a larger thermal mass compared to the baseboard heater heating system in the commercial zones.
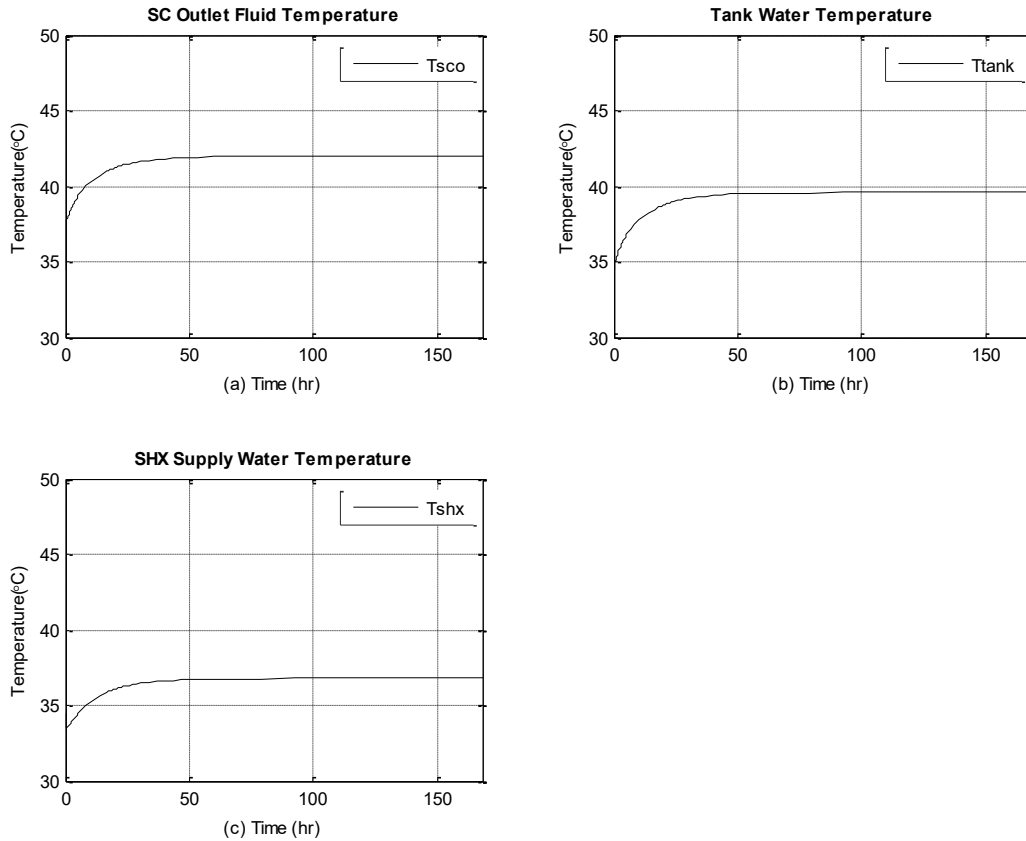
Figure 3.4.2 Open-loop test of solar system temperature at design condition

At the design condition, Figure 3.4.2 (a) shows the effect of solar incident energy on the flat-plate solar collectors. The flat-plate solar collector antifreeze outlet temperature can reach nearly 42°C. Besides, Figure 3.4.2 (b) shows the water temperature inside the solar storage tank. This temperature is approaching nearly 40°C which is two degrees lower than the collector outlet temperature. The reason is due to heat losses and the effectiveness of the heat exchanger. In the tank. Also, Figure 3.4.2 (c) indicates the solar heat exchanger (SHX) secondary (cold) side outlet

water temperature. As can be noticed the residential zones return water temperature is increased to 36.8°C by the energy transferred from the solar system. Taken together, the open-loop responses show expected trends from a space heating system. And the magnitude of temperatures indicates that the overall system is properly sized. Also, it can be noted that the overall system responses show a multi-time scale property. In other words, the solar tank temperature response is the slowest, followed by the residential zone air temperature responses and the boiler and the commercial zone temperature responses. The overall system consists of coupled heat transfer processes with energy interactions taking place among the sub-systems.

CHAPTER 4 CONTROL STRATEGIES FOR THE HYDRONIC SPACE HEATING SYSTEM

4.1 Introduction

In this chapter, the design, tuning and control performance of the hydronic space heating system under different control strategies will be explored. First of all, the control structures of the integrated system are discussed. After that, the entire system dynamic responses subjected to various disturbances are investigated. Then, the controller performance under conventional on-off and PI control strategy will be examined. In the end, a gain scheduling adaptive control strategy is developed. The objective is to find an appropriate control strategy in order to improve the control performance of the system.

4.2 Overall system control loops

In total, this solar-assisted hydronic space heating system has ten individual control loops as such this system is characterized as a multiple loop control system. The first control loop is the boiler control loop (C1) as shown in Figure 4.2.1, it regulates the boiler fuel supply rate in order to keep the boiler supply water temperature at its set-point. The second control loop is the boiler heat exchanger (BHX) control loop (C2) as shown in Figure 4.2.2, which governs the boiler heat exchanger secondary (cold) side outlet water temperature which is inlet temperature to the radiant floor heating system, by regulating the primary (hot) side mixed water temperature. The third controller (C3) is in the flat-plate solar collector circulating loop as shown in Figure 4.2.3 on the left side. This controller turns on-off the circulating water pump to charge or not charge the storage

tank with solar energy. The fourth controller (C4) is in the solar tank and solar heat exchanger (SHX) control loop as shown in Figure 4.2.3 on the right side. The controller C4 controls the solar heat exchanger pump on or off in deciding whether or not to use solar tank energy to offset the residential zones load. Next group of control loops (C5-C6) are for the commercial zones water loops as shown in Figure 4.2.4. They regulate the supply water flow rate to the baseboard heaters of two commercial zones through two-way valves. The last group of control loops (C7-C10) are the residential zones water loops as shown in Figure 4.2.5. These group of controllers control the supply water flow rate to the radiant floor heating system supplying hot water to four residential zones via three-way mixing valves. An integrated solar-assisted hydronic space heating system with all control loops is depicted in Figure 4.2.6. For simplicity, only one control loop for each of the residential and commercial zones is depicted in Figure 4.2.6. The overall control system is a mixed mode control system involving both modulating controls and on-off controls. This adds complexity in designing control strategies for the overall systems due not only to the interacting thermal processes of the physical system but also due to interactions between the multiple control loops of the system.
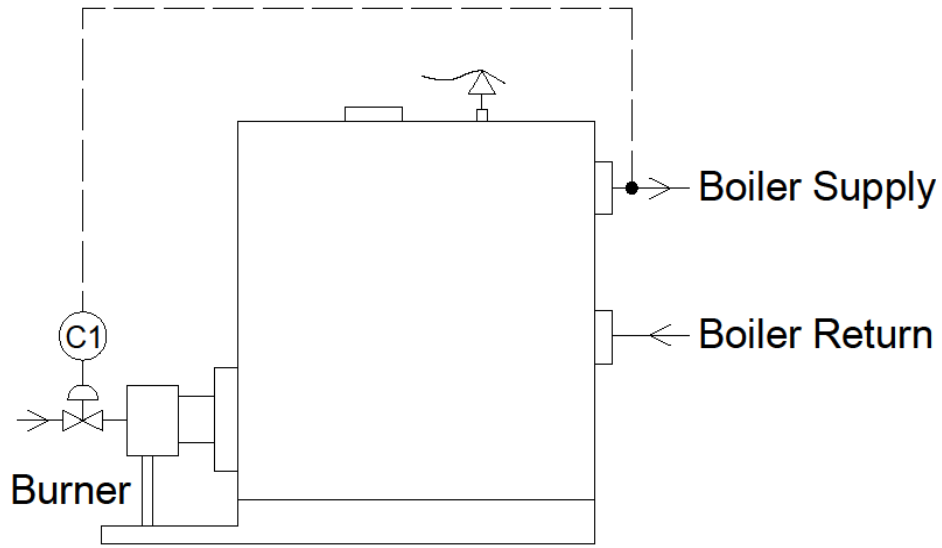
Figure 4.2.1 Gas-fuel boiler (B) control loop
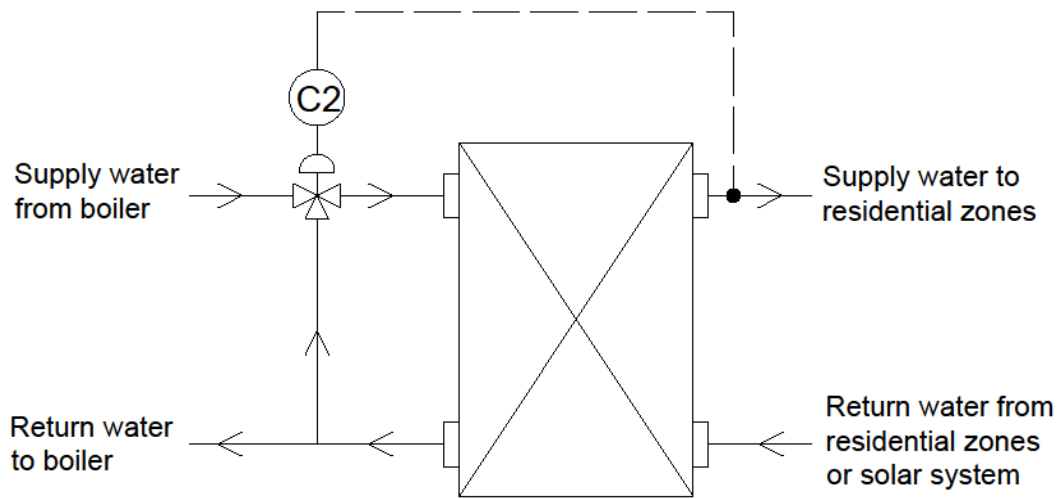
Figure 4.2.2 Boiler heat exchanger (BHX) control loop
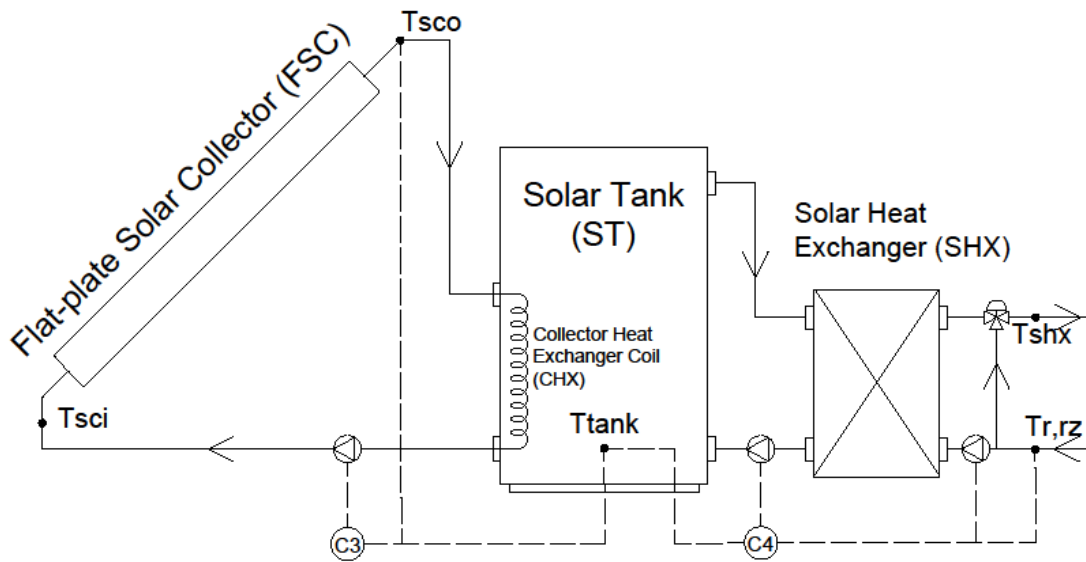
Figure 4.2.3 Solar system control loops
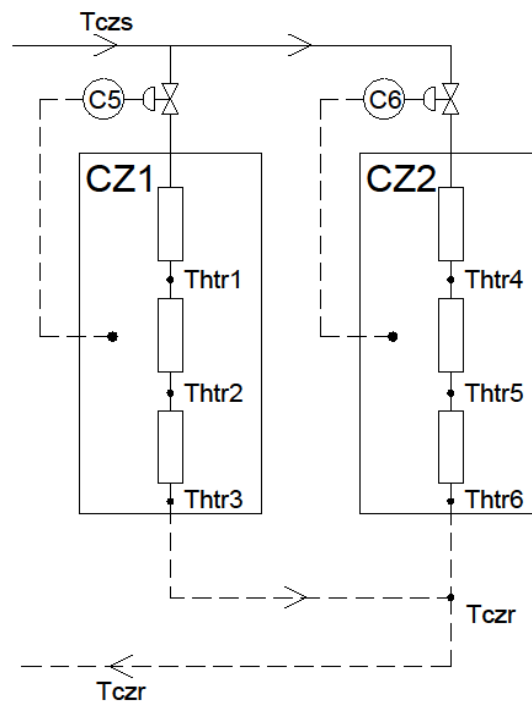
Figure 4.2.4 Commercial zones control loops
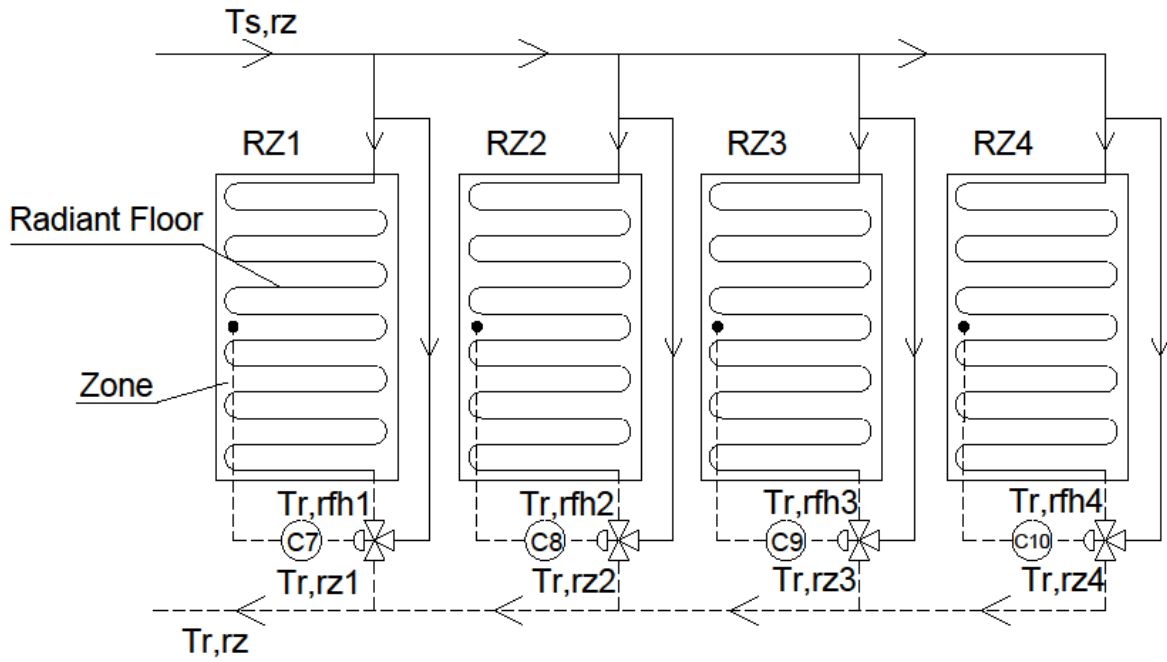
Figure 4.2.5 Four residential zones control loops
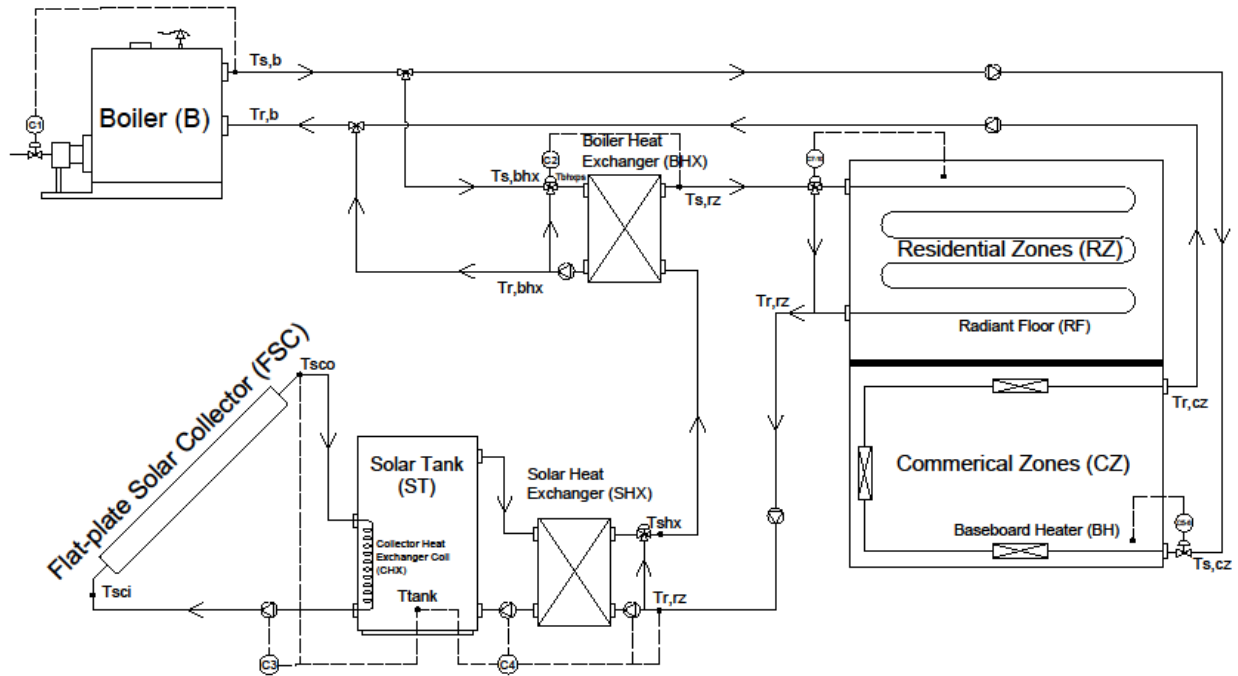
Figure 4.2.6 Schematic diagram of the solar-assisted hydronic space heating system control loops

4.3 The impact of load disturbances on zones

Three main disturbances have an impact on zone air temperature responses which include the outdoor air temperature, solar heat gain and internal heat gain. Besides, the initial condition itself may also affect the zone air temperature responses. Most of building HVAC systems are designed for the worst case scenario. In other words, in the case of space heating system design, the worst case condition means the lowest outdoor air temperature and without any solar heat gains and internal heat gains. However, in practice, the building HVAC systems operate under relatively mild environment compared with the design condition, which means the hydronic space heating system usually works at a higher outdoor air temperature conditions and with some internal heat gains. Therefore, the proper design of HVAC control system and appropriate HVAC control strategies are essential to maintain desired indoor air temperature and to optimize the energy consumption.

To investigate the impact of load disturbances, a typical day outdoor air temperature profile is assumed as shown in Figure 4.3.1. This typical day outdoor air temperature follows a sinusoidal profile with a 10°C daily range. The lowest temperature -23°C occurs at midnight around 3:00, and the highest temperature -13°C occur in the afternoon around 15:00. In addition, the hourly solar radiation profile, as shown in Figure 4.2.1, is modeled based on the Hottel's clear sky model [6]. It can be seen from Figure 4.3.1 that the peak solar radiation occurs at noon, and the daytime starts from 7:00 and ends at 17:00. By applying this solar irradiance profile, the indoor solar heat gain can be calculated for each zone. Furthermore, internal heat gains are also considered in this study. The commercial zones have higher internal heat gain during the operation hours between 8:00 to 19:00. For the residential zones, the internal heat gain is usually small as such it is neglected.
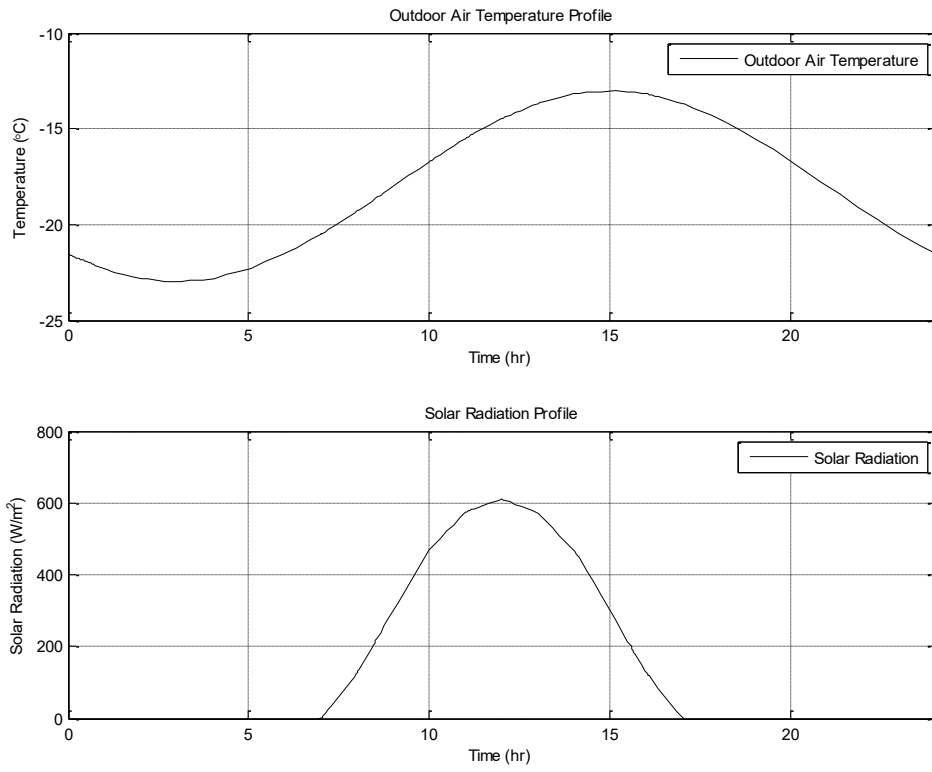
Figure 4.3.1 Typical day outdoor air temperature and solar irradiance

The dynamic response of both zones indoor air temperatures subjected to above load disturbances and without any controls are presented in Figure 4.3.3.
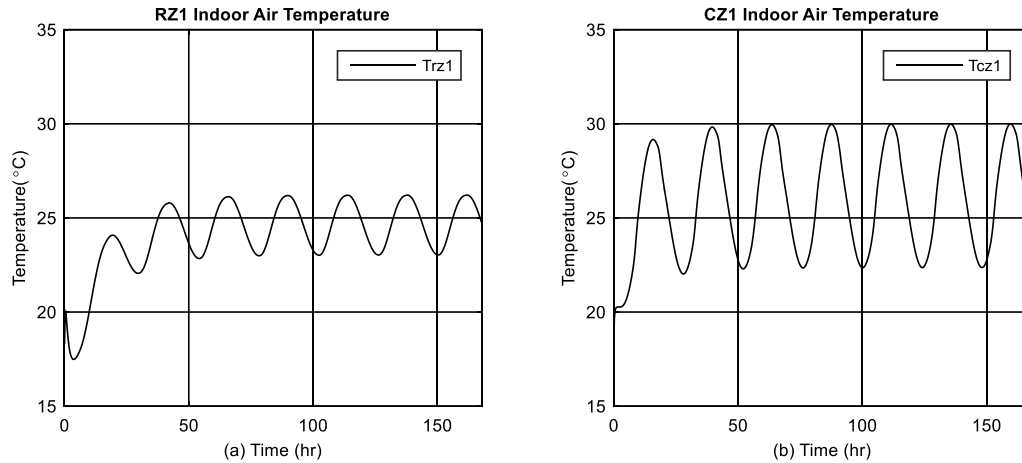
Figure 4.3.2 Residential and commercial zones indoor air temperature responses with no control

A seven days simulation was conducted to investigate the impact of load disturbances on both zone temperatures. It can be seen that with no controls the residential zone indoor air temperature fluctuates between 23 °C to 26°C, and the commercial zone temperature fluctuates between 22°C to 30°C. The commercial zones indoor air temperature has larger oscillations compared with residential zone temperature. This is because of the commercial zones have higher solar heat gains and extra internal heat gains. On the other hand, the internal heat gains are not considered in the residential zones.

4.4   The overall system control structure

As stated before, the overall system consists of multiple control loops. Here the design of control strategies for each control loops is presented. The overall control system was designed to be comprised of on-off controls and modulating controls. The on-off control was used to control the operation of the solar system, and modulating controls were designed to control the boiler,

boiler heat exchanger, residential and commercial zones. This mixed mode control structure was selected in consideration of the practical operation of the system and to achieve good temperature control performance of the system.

The conventional on-off control strategy is designed for the solar system. Figure 4.4.1 shows the on-off control working strategy for the controller (C3) which is placed in the flat-plate solar collector side, and also for the controller (C4) which is located between the solar tank and the solar heat exchanger side.
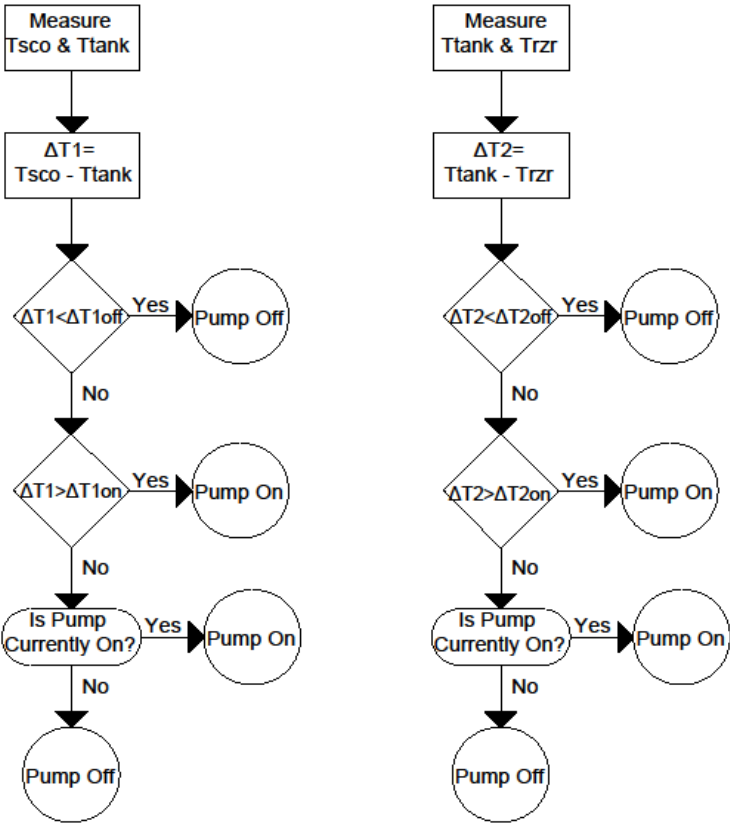
Figure 4.4.1 On-off control block diagrams

The pump in the flat-plate solar collector water circulating loop controlled by the controller C3 is turned on when the temperature difference between the flat-plate solar collector outlet temperature T_{sco} and solar tank temperature T_{tank} reach the turning on differential point ΔT_{1on} which is set at 5.5°C, and it is turned off when this temperature difference drops below ΔT_{1off} which is set as 1°C [8]. The operation strategy of controller C4 which is located between the solar tank and the solar heat exchanger is similar that of controller C3. It turns on the pump when the temperature difference between the solar tank temperature T_{tank} and residential zones return water temperature $T_{r,rz}$ greater than ΔT_{2on} which is set to 5°C, and the pump is turned off when this temperature difference drops below ΔT_{2off} which is set at 1°C [8]. The differential temperature limits were chosen to prevent frequent on-off switching of the pump.

4.5 Conventional PI control strategy for the boiler, boiler heat exchanger, residential and commercial zones

Except for the solar system which is on-off controlled, a conventional proportional-integral (PI) control strategy will be designed for all the remaining control loops in this section. Figure 4.5.1 shows a typical closed-loop PI control block diagram for the boiler control loop (C1), the boiler heat exchanger control loop (C2), the commercial (C5-C6) and residential (C7-C10) zones control loops. These controllers are designed to regulate the boiler supply water temperature, boiler heat exchanger secondary side supply water temperature and zone indoor air temperatures, respectively.
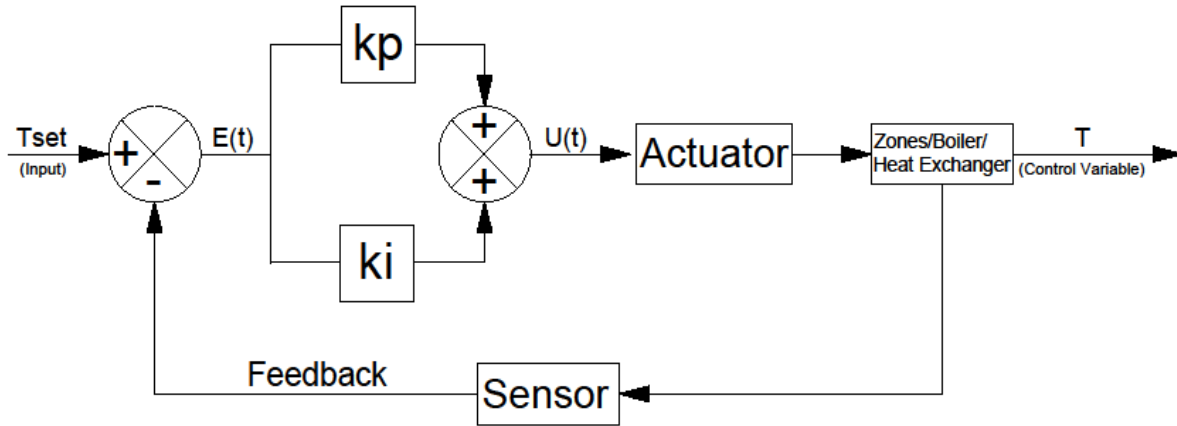
Figure 4.5.1 PI control block diagram

The PI control equations for the above block diagram are described below:

$$e(t) = T_{set} - T \tag{4.1}$$

$$U(t) = k_p e(t) + k_i \int_o^t e(t)dt \tag{4.2}$$

Where $e(t)$ is the error, T_{set} is the set-point temperature, T is the current temperature. k_p is the proportional gain, k_i is the integral gain and $U(t)$ is the control signal. Both gains are obtained by applying Ziegler-Nichols tuning rules. These were further fine-tuned to achieve better control performance. By using the residential zone 1 as an example, the closed-loop PI control response of indoor air temperature under design outdoor temperature of -23°C and design supply water temperature of 50°C were obtained. These are depicted in Figure 4.5.2. The indoor temperature set-point was set at 22°C. The PI controller gains were as follows: proportional gain k_p =1, and the integral gain k_i =0.001 respectively. The simulated result shows that the residential zone 1 indoor air temperature has an acceptable set-point tracking response. The larger thermal mass of radiant floor heating system is the main reason for small initial oscillations.
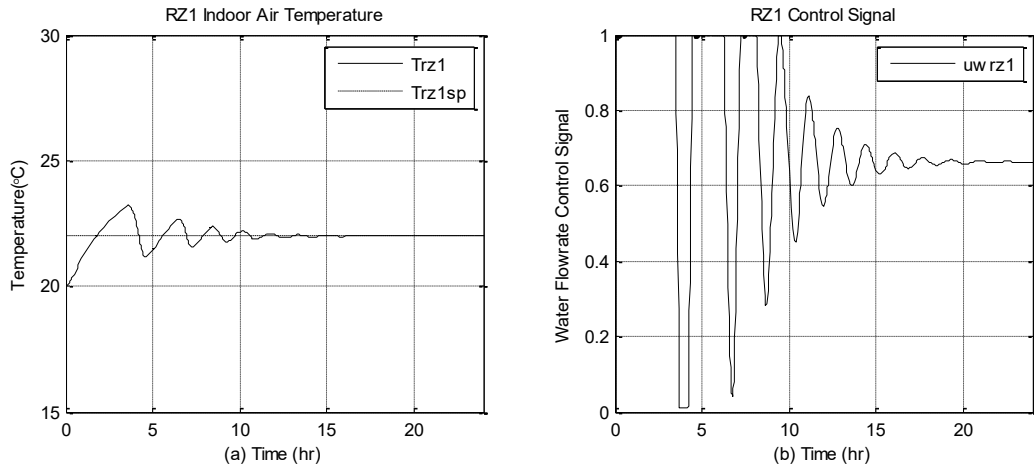
Figure 4.5.2 Conventional PI controller responses of residential zone indoor air temperature

However, when the zone is subjected to different outdoor conditions or a sudden set-point change, this conventional constant gain PI control strategy does not provide an acceptable temperature tracking performance. Below Figure 4.5.3 (a) and (b) show the residential zone indoor air temperature responses subjected to a less cold outdoor air temperature of -13°C. Figure 4.5.3 (c) and (d) shows the impact of a sudden change in zone temperature set-point. All other parameters were kept the same as in the above simulations.
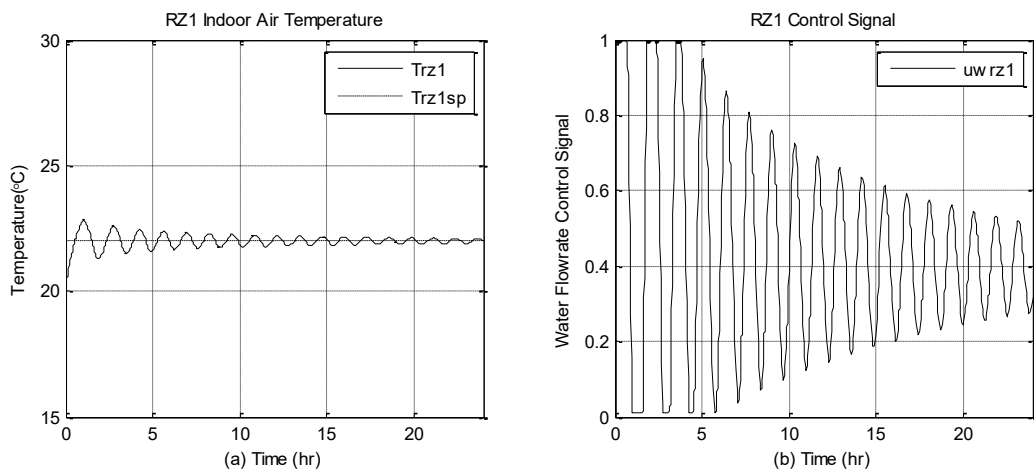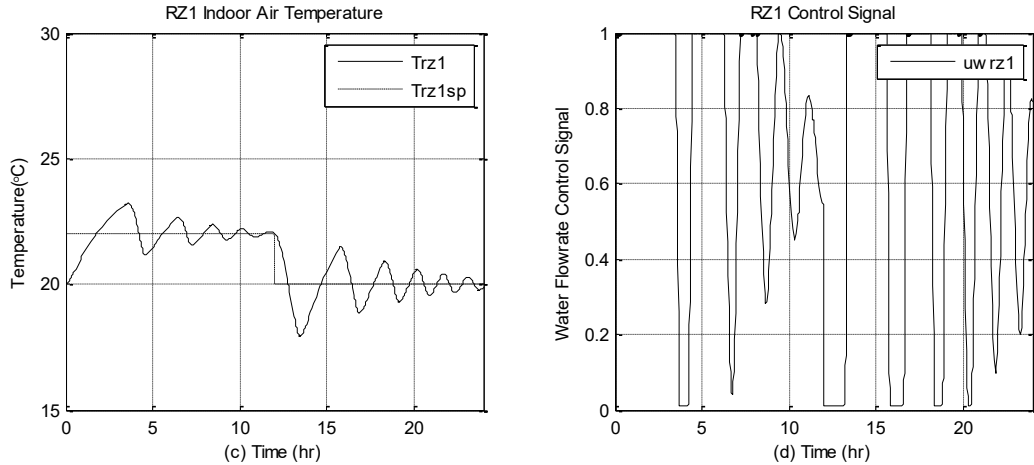
Figure 4.5.3 Temperature response subjected to low outdoor temperature and a 2°C set-point change

From Figure 4.5.3(a) and (b) it can be noted that the residential zone temperature shows oscillatory response around the set-point. Longer settling time is also one of the outcomes when subjected to outdoor temperatures warmer than the design outdoor temperature. In addition, when a 2°C set-point change is applied, as can be seen in Figure 4.5.3(c) and (d), more noticeable overshoots and oscillations set-in. This is due to the fact that the controller gains were designed for design outdoor conditions (Full-load condition). When the same gains are used for the controller for low-load conditions, the control responses will be sluggish and as shown above, which could lead to significant oscillations. Furthermore, being a system with multiple control loops, interactions among the control loops also contribute to oscillations. Under these circumstances, a control strategy which attenuates the effects of interactions and compensates for changes in loads and operating conditions is needed. To address these issues, a gain scheduling adaptive (GSA) PI control strategy is proposed to improve the controller performance under all operating conditions.

4.6 Gain scheduling adaptive PI control strategy

Due to the nonlinear characteristics of the system and unknown disturbances acting on the system, the conventional constant gain PI controller cannot give good temperature control responses. In addition, frequent tunings of each control loop for different situations are very time-consuming. For the above reasons, a gain scheduling adaptive (GSA) PI control strategy is proposed to improve the control performance and achieve good set-point tracking. The gains in GSA PI controller are variable within a predetermined range, and the change rate is adaptive with the error and system load. The GSA PI control equations are shown below:

$$U(t) = k_p(t)e(t) + k_i(t) \int_o^t e(t)dt \tag{4.3}$$

Where $k_p(t)$ and $k_i(t)$, both are followed as a function of the error $e(t)$, the proportional gain $k_p(t)$ is expressed as below:

$$k_p(t) = k_{p(max)} - \left(k_{p(max)} - k_{p(min)}\right)exp^{-(k|e(t)|)} \tag{4.4}$$

$$k = |e(t)| * \frac{a_z(T_z - T_o)}{C_w m_w(T_{zs} - T_{zr})} \tag{4.5}$$

A larger proportional gain value is used to speed the system response when $e(t)$ is large, and a small proportional gain value is used to eliminate overshoots and oscillation once $e(t)$ become small. From the equation, it can be noted that, when the error $e(t)$ is large, the exponential term will approach zero, therefore the proportional gain will reach $k_{p(max)}$. Likewise, when the $e(t)$ becomes small, the exponential term will approach 1, and so the proportional gain will equal to $k_{p(min)}$. Moreover, k is the adaptive parameter which takes over the rate of change of gains between its maximum and minimum value. a_z is the zone heat loss coefficient, T_z and T_o are the

zone air and outdoor air temperatures. T_{zs} and T_{zr} are the zone supply and return water temperature respectively. Figure 4.5.1 shows the effect of different k values on the proportional gain when the error is increasing. When a larger error occurs, a higher k value can speed up the rate of increase in the proportional gain to approach its maximum value and vice versa.
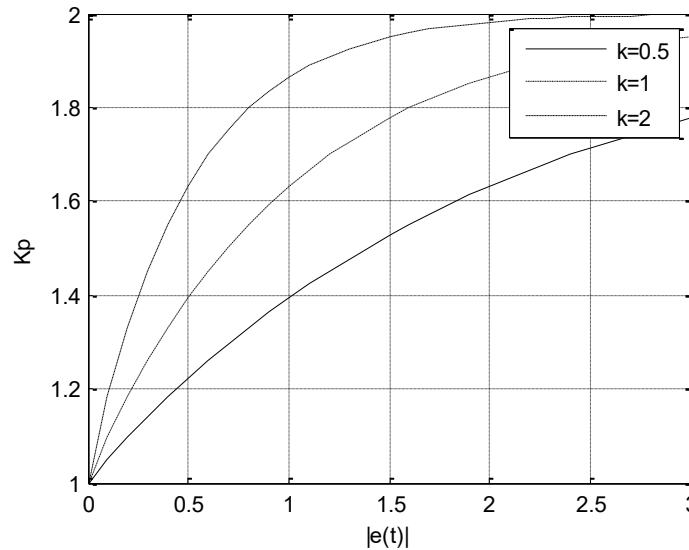
Figure 4.6.1 Effect of different k values work on the proportional gain changing

The integral gain $k_i(t)$ can be expressed as a function of error as below:

$$k_i(t) = k_{i(max)}exp^{-(k|e(t)|)} \tag{4.6}$$

Under steady-state conditions, when $e(t)$ becomes small, a lager integral gain is used to eliminate the steady-state error and vice versa. A smaller integral gain can eliminate the undesirable oscillations and overshoots. Still using the residential zone 1 as an analysis example, the dynamic response of its indoor air temperature subjected to design outdoor condition (-23°C) and design supply water temperature (60°C) was simulated. The responses are shown in Figure 4.6.2. The gains of GSA PI controller used in this simulation are updated based on previous

constant gain values, setting $k_{p(max)} = 2k_p = 2$, and $k_{p(min)} = k_p = 1$. The value of $k_{i(max)}$ is

selected as a small value. The results show that the controller has a better performance compared

with the constant gain PI control. Below Figure 4.6.2 and 4.6.3 show the zone temperature

responses and the corresponding evolution of gains.
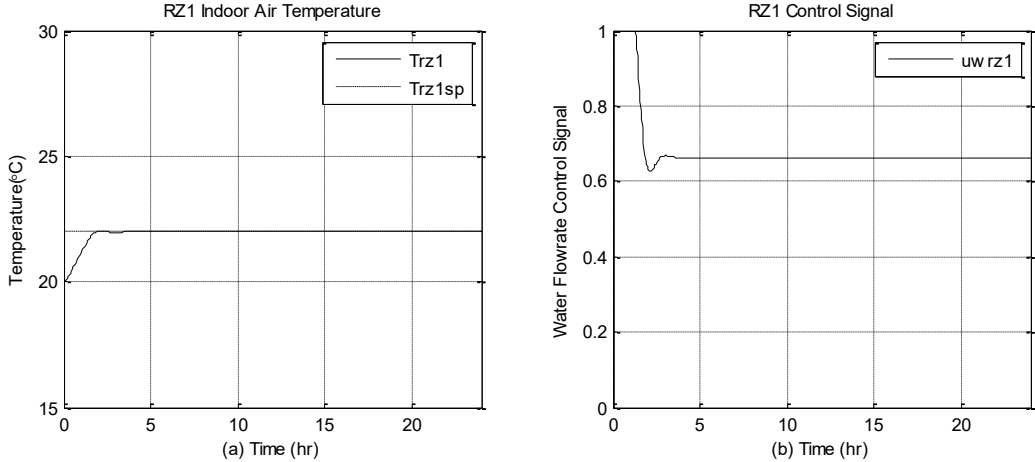
Figure 4.6.2 GSA PI control responses of residential zone indoor air temperature
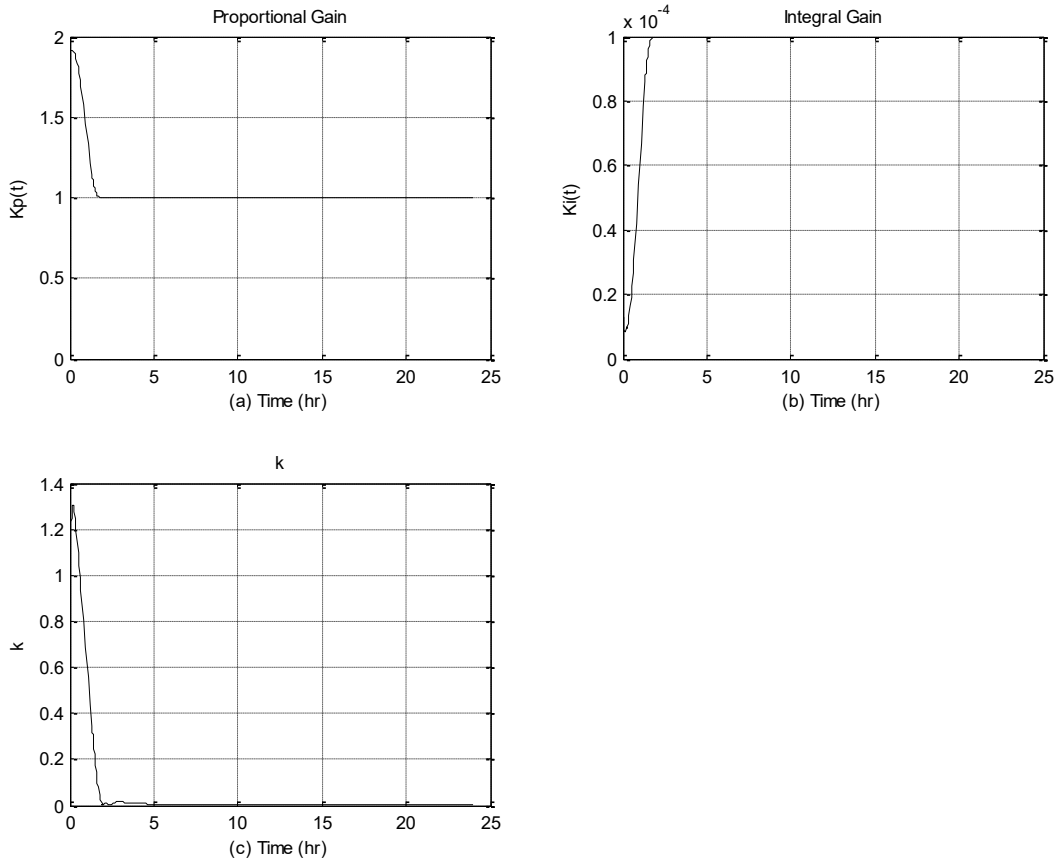
Figure 4.6.3 Variation of $k_p(t)$, $k_i(t)$ and k

The dynamic responses of the zone temperature under GSA control with the zone subjected to low outdoor air temperature (-13°C) or a sudden 2°C indoor set-point change, are shown in Figure 4.6.4.

\
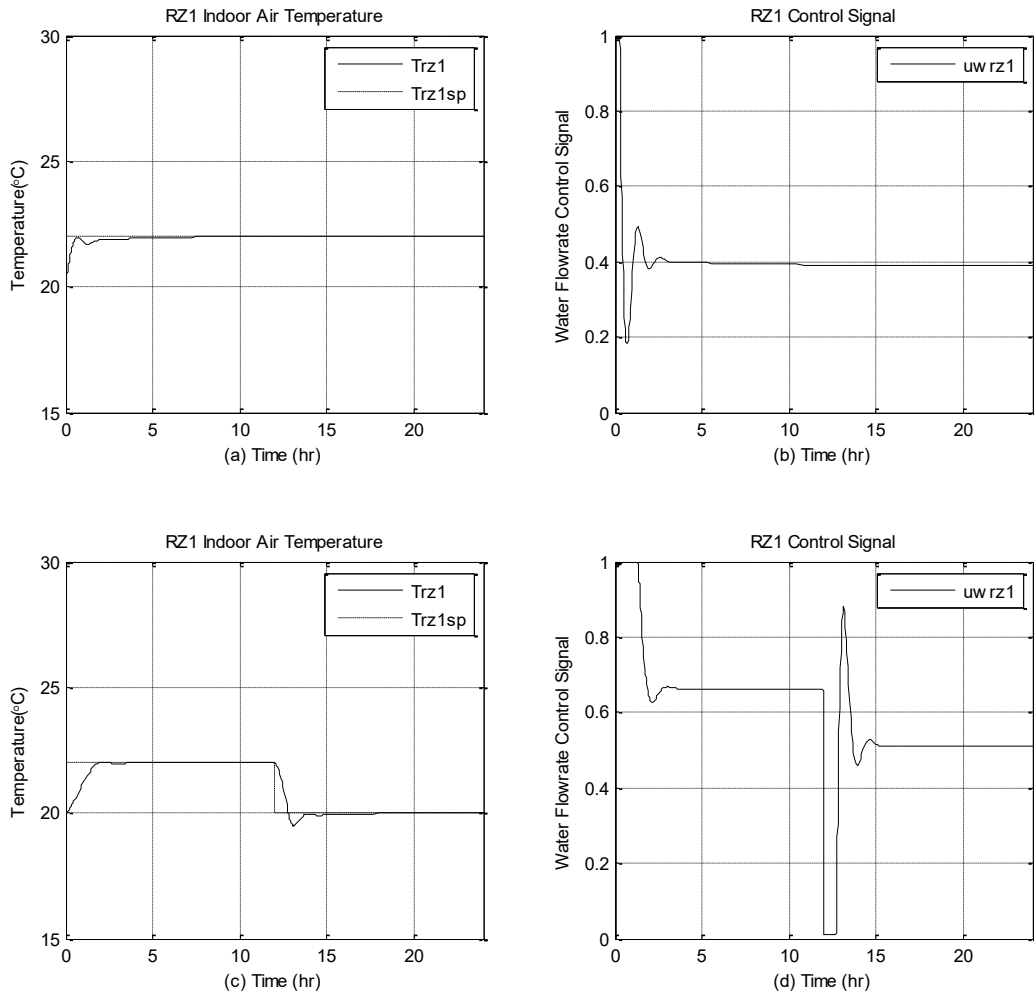
Figure 4.6.4 GSA control temperature response under low outdoor temperature or 2°C

set-point change

Comparing the GSA PI control responses with constant gain PI controller responses, it can be stated that the GSA PI controller responses show obviously better control performance under low load condition or due to a 2°C set-point change. Therefore, it is apparent from the above results that the GSA PI controller gives superior and stable responses under different load conditions. In the next section, the GSA PI controller will be applied to the other control loops in the integrated system, and its performance will be studied,

4.7 Integrated system dynamic response under on-off and GSA PI control

The GSA PI control was applied to all control loops except for the solar system which was controlled by two on-off controllers. The integrated solar-assisted hydronic space heating system responses under two different situations are simulated in this section. The first simulated case is full load condition, and the second case is partial load condition and also subjected to a 2°C change in zone temperature set-point.
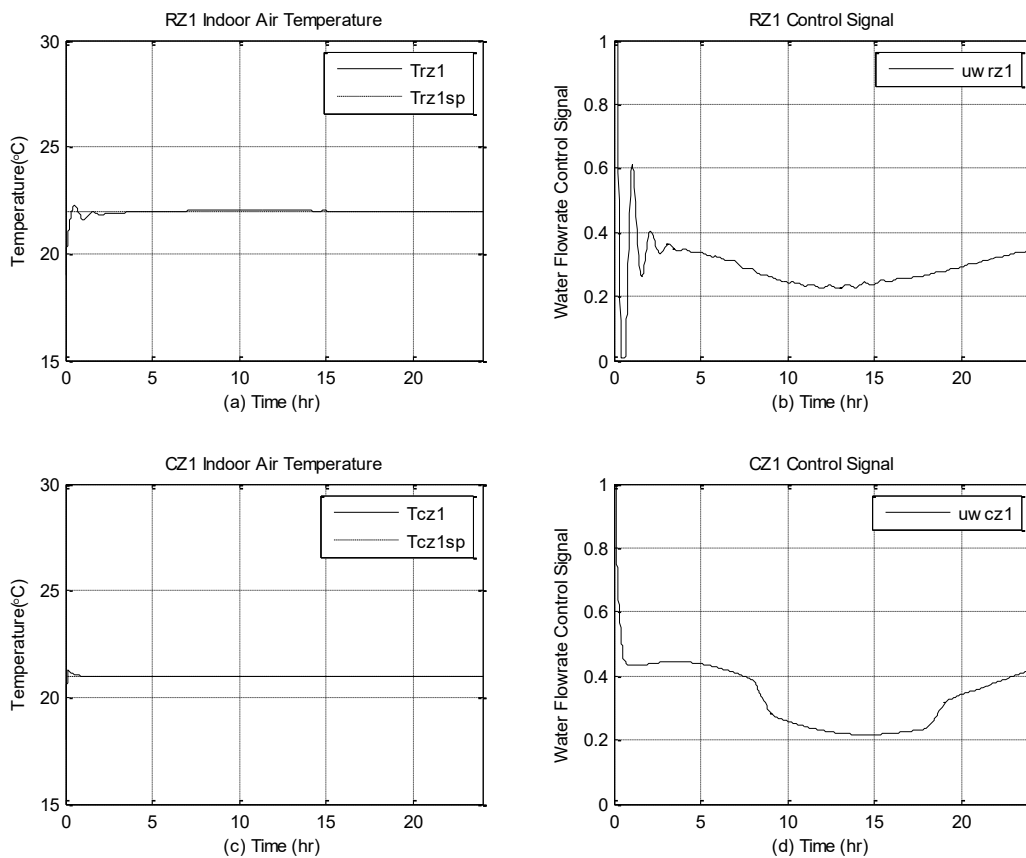
Figure 4.7.1 Residential and commercial zone temperature responses under GSA PI control in full load case
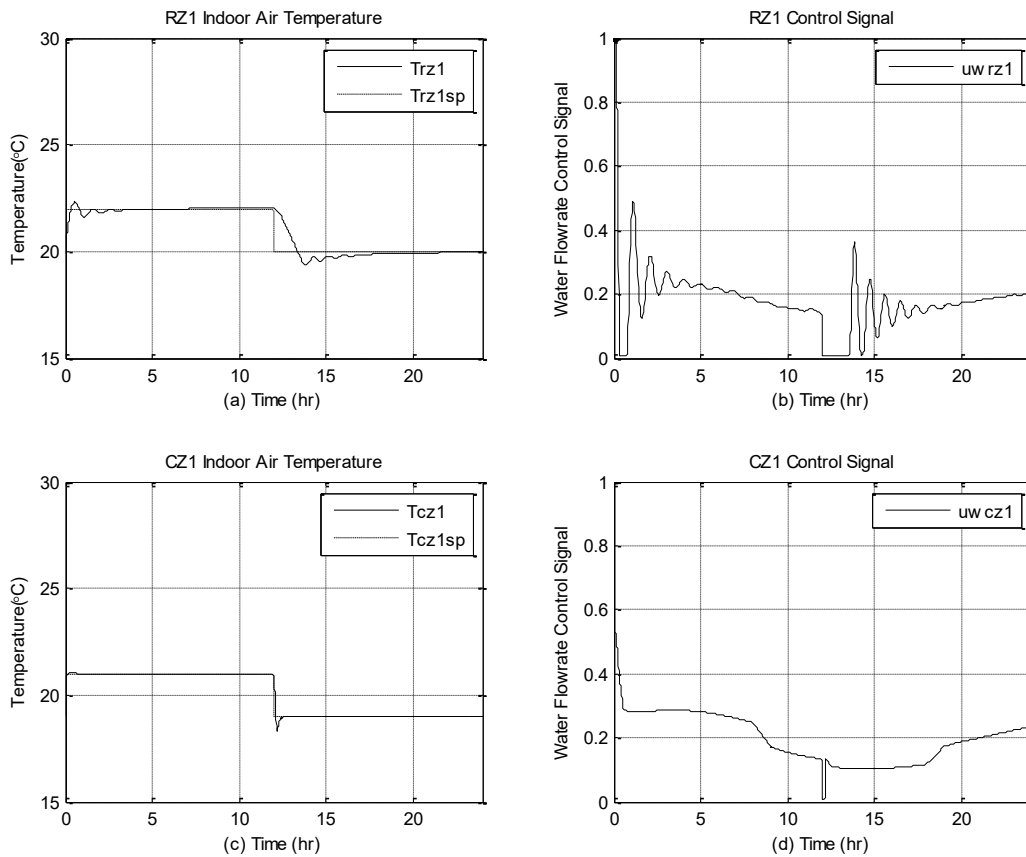
Figure 4.7.2 Residential and commercial zone temperature responses under GSA PI control in partial load case and subjected to 2°C set-point change

Figure 4.7.1 shows the indoor air temperature responses and water flowrate control signals for residential and commercial zones respectively. It can be seen that the indoor air temperatures for both zones are well regulated by using GSA PI control under full load conditions. Both temperatures reached their respective set-points 22°C and 21°C. Figure 4.7.2 shows the zone temperature response under partial load conditions together with a change in zone temperature set-point. During partial load the outdoor temperature is warmer which varies between -13°C and -3°C as opposed to full load case in which the outdoor air temperature was -23°C. In addition, the solar irradiance level is 1.25 times higher under partial load conditions than the full load condition.

A sudden 2°C set-point changes in both residential and commercial zone temperatures have also added to the severity of the multiple disturbances acting on the system. Under these load conditions, the overall system performance with multiple control loops was simulated. The results are presented in Figures 4.7.1, and 4.7.2 show that the GSA PI controllers are responding faster when subjected to a sudden set-point change. Also, under partial load conditions, the water flowrate control signals for both zones have decreased compared to the full load conditions.
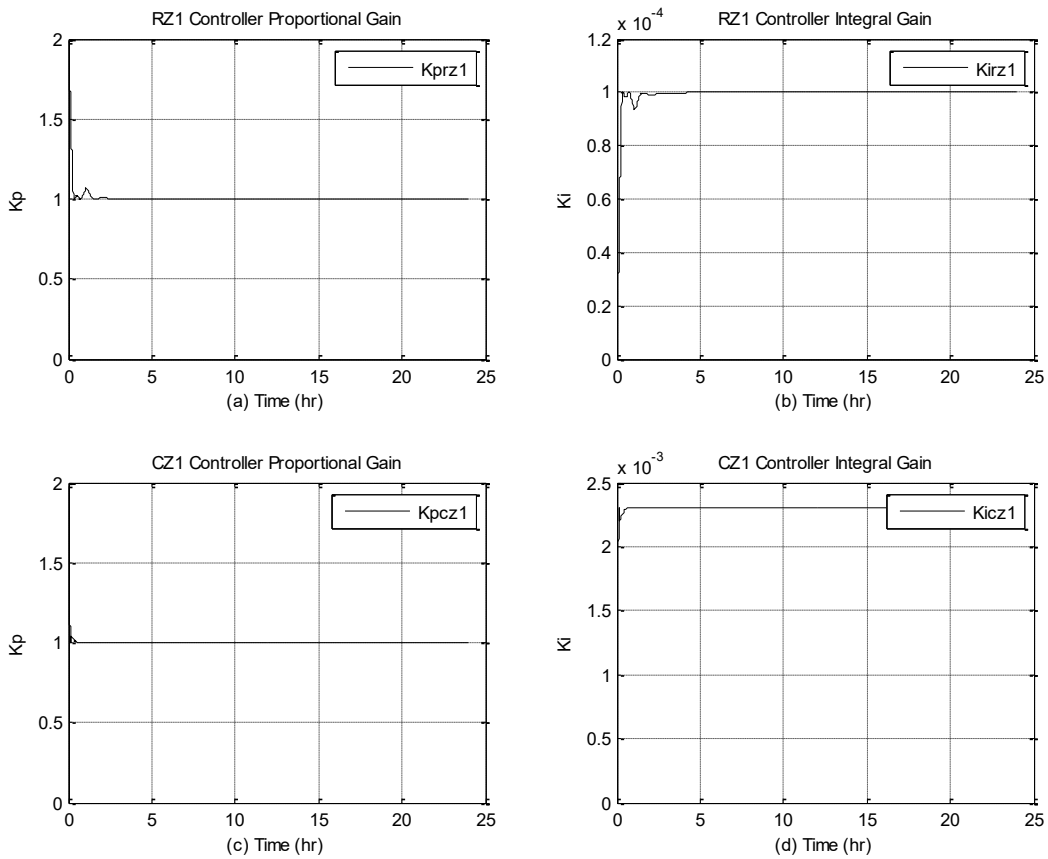
Figure 4.7.3 Adaptive proportional and integral gains for zone temperature controllers in full load condition
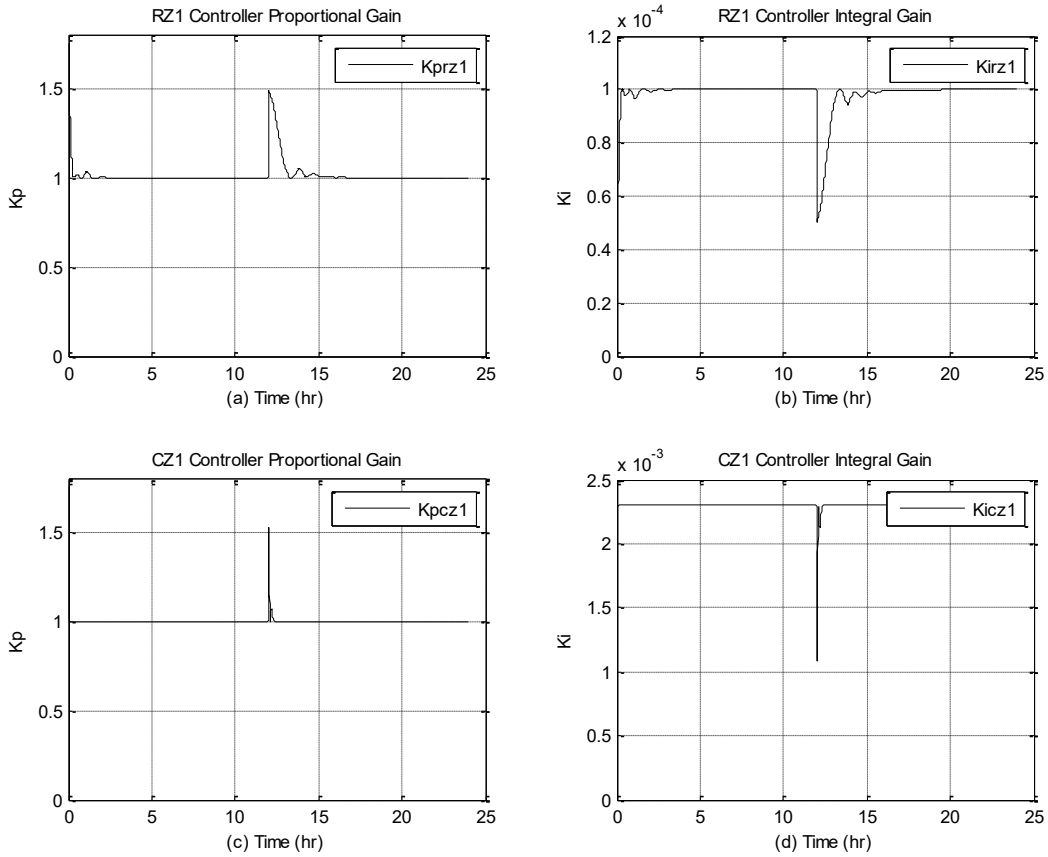
Figure 4.7.4 Adaptive proportional and integral gains for zone temperature controllers in partial

load case and subjected to 2°C set-point change

Figure 4.7.3 and Figure 4.7.4 show the adaptive proportional and integral gains of the zone temperature controllers. It should be noted that, when the system is subjected to a sudden load change, the controller gains adapt to this change which confirms the adaptation process is working efficiently. The proportional gains are increasing when a larger error occurs and vice versa. A large proportional gain can accelerate the system response. Contrary to proportional gains, the integral gains start to decrease when a larger error occurs. Because a smaller integral gain can make the controller work in a more stable manner with less oscillations.
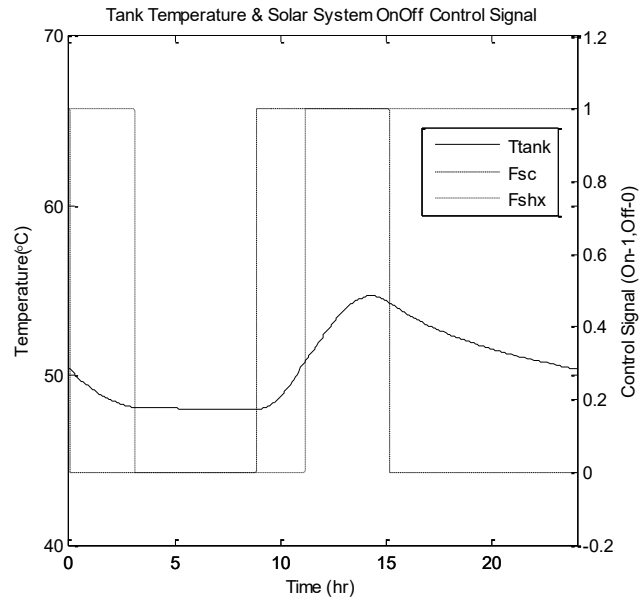
Figure 4.7.5 Tank temperature response and solar system on-off control signal in full load

condition
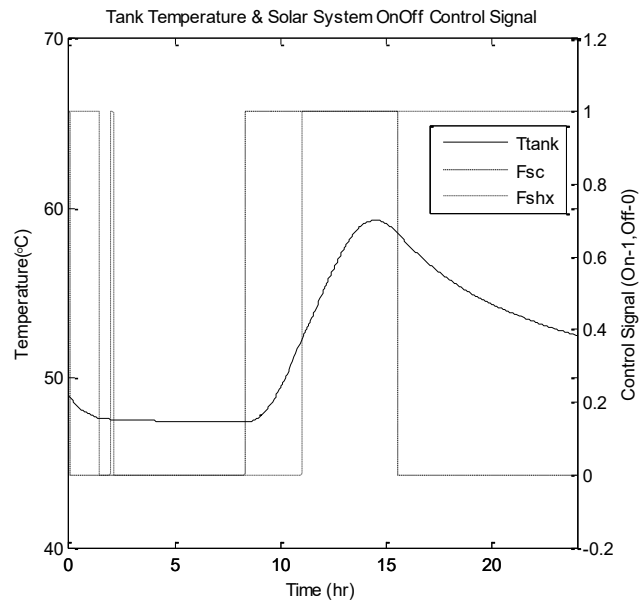
Figure 4.7.6 Tank temperature response and solar system on-off control signal in partial load

case and subjected to 2°C set-point change

Figures 4.7.5 and 4.7.6 show the responses of the conventional on-off control strategy applied to the solar system. The on-off cycles of the controller and solar tank temperature are depicted in Figure 4.7.5 and Figure 4.7.6 respectively. The available solar energy is dependent on ambient air condition and the solar radiation intensity. As can be seen from Figure 4.7.5, under full load condition, the pump controller C3 turns on around 09:00 in the morning and turns off after 15:00 in the afternoon. However, from Figure 4.2.1, the simulated daytime starts from 7:00 and ends at 17:00. It means the collector system needs about 2 hours to reach the pump turn-on temperature differential (ΔT_{1on}). For the solar heat exchanger side controller C4, when the temperature difference between the tank and radiant floor return water temperature reaches ΔT_{2on}, the pump controller C4 is tuned on. During the solar system working period, the solar tank water temperature increases. However, in the partial load condition, due to higher solar intensity level and outdoor temperature, the controller operation cycle shows a longer working period than full load case. Moreover, the water temperature in the tank can reach to a higher level.
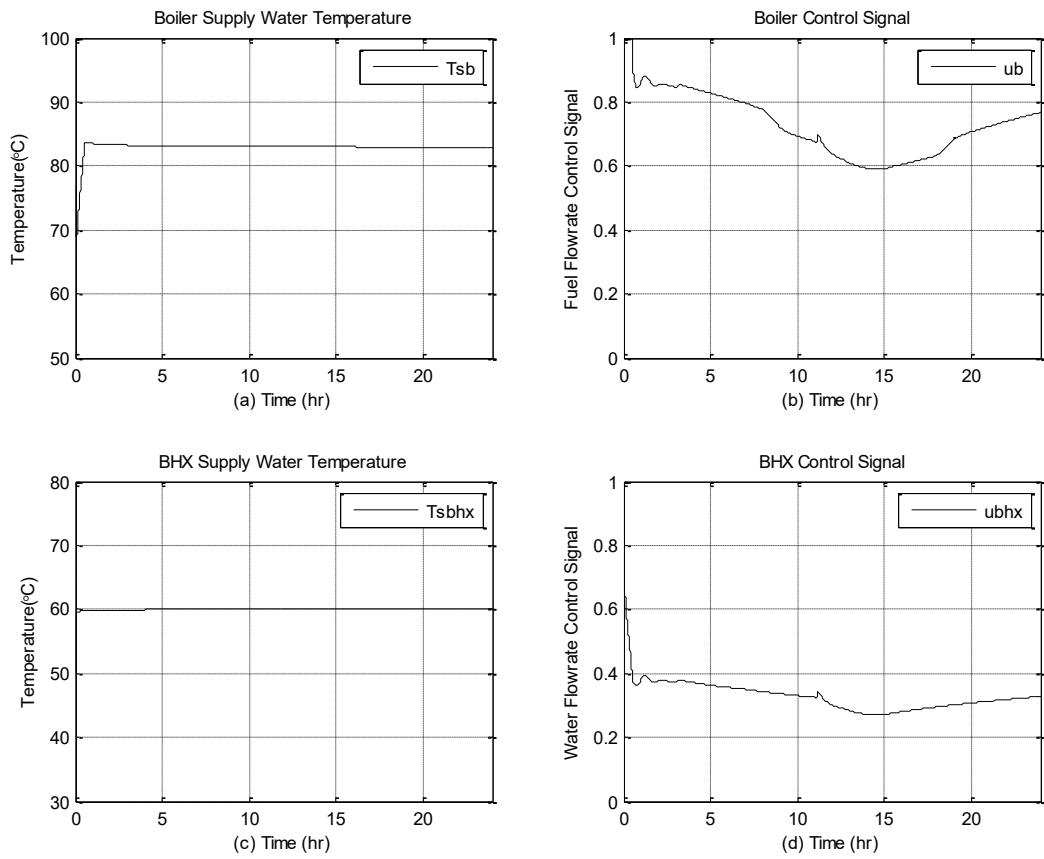
Figure 4.7.7 Temperature responses of the boiler and BHX control loops under GSA PI control

in full load condition
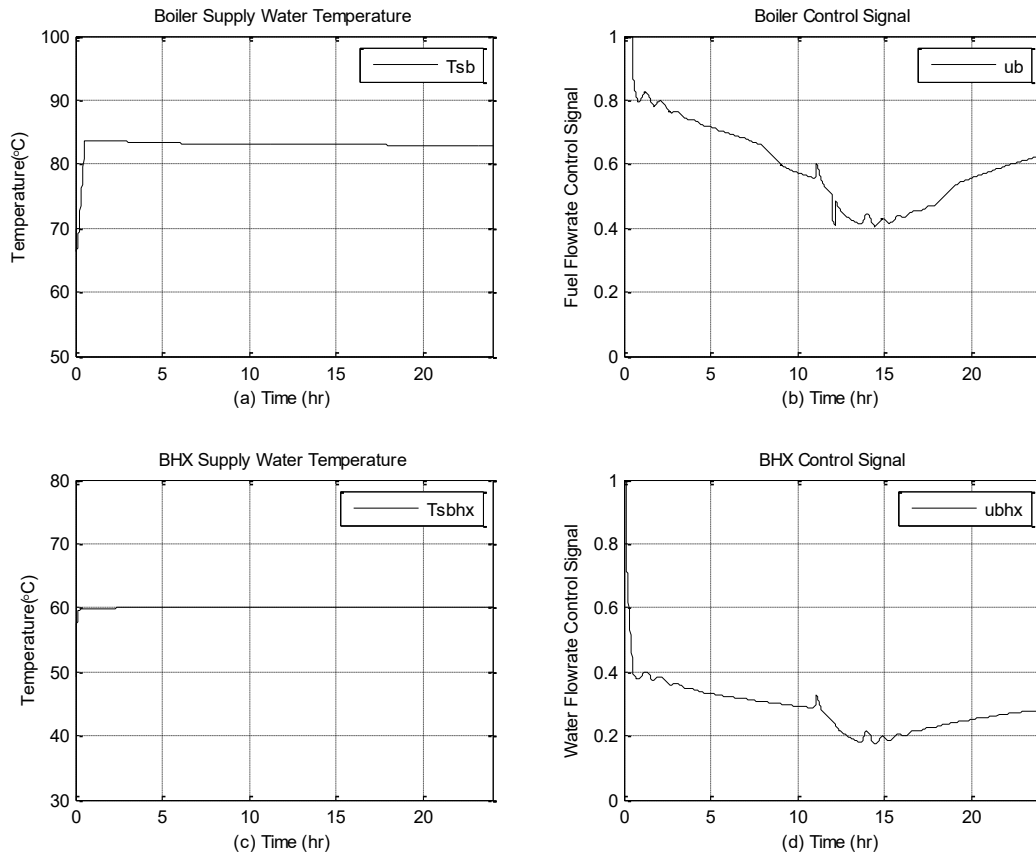
Figure 4.7.8 Temperature responses of the boiler and BHX control loops under GSA PI control

in partial load case and subjected to 2°C set-point change

Figure 4.7.7 and Figure 4.7.8 show the GSA PI controller responses of the boiler supply

water temperature and boiler heat exchanger under full-load and partial-load conditions. The boiler

supply water temperature in both cases is maintained close to their set-point 83°C and 60°C,

respectively. However, it can be noticed that starting from around 11:00 clock, both water flowrate

control signals show a slightly declining trend. This due to the fact that energy is being added by

the solar system which is used via the solar storage tank to preheat the return water temperature

from the radiant floor system. To improve the overall system energy efficiency, it is important to

reset the boiler and boiler heat exchanger supply water temperatures as a function of the load so

that more and more solar energy can be utilized by the radiant floor heating system for space heating of the residential zones. To study this aspect, a system optimization problem is formulated and solved as discussed in next Changer 5.

CHAPTER 5 SYSTEM OPTIMIZATION

5.1 Introduction

In the last Chapter 4, the supply water set-points for boiler and boiler heat exchanger are somewhat arbitrary as they were selected by carrying out open loop tests under full-load and partial conditions. However, it is important to explore energy savings through resetting of the supply water temperature set-points based on system optimization techniques. To this end, an optimization problem was formulated and solved to determine optimal set-points. Based on this an optimal set-point operation strategy for the overall system is proposed in this chapter. The objective is to minimize the system energy consumption and maintain good control of indoor air temperature in the zones.

5.2 Aggregated model versus the full-order model

The overall detailed model of the system developed in Chapter 3, which is referred to here as the full-order model, consists of 275 differential equations. As such it is too large and complex to do the system optimization. Therefore, a simplified aggregated model of the system is developed in this chapter for the optimization study. The simplified aggregated model consisting of 24 equations is presented below:

Residential zone air aggregated model:

$$C_{rz,agg} \frac{d(T_{z,rz,agg})}{dt}$$

$$= Q_{radfloor,agg} - A_{rzwin,agg} U_{win}(T_{z,rz,agg} - T_o)$$

$$- A_{rzwall,agg} U_{wall}(T_{z,rz,agg} - T_o) \qquad (5.1)$$

$$- A_{rzroof,agg} U_{roof}(T_{z,rz,agg} - T_o)$$

$$- \frac{ACH_{rz} * Vol_{rz,agg} * c_a * \rho_a * (T_{z,rz,agg} - T_o)}{3600} + Q_{agg,sol,rz}$$

Radiant floor heating system aggregated model:

$$C_{wt,agg} \frac{d(T_{w,agg})}{dt}$$

$$= c_w m_{w,rz,agg}(T_{s,rz,agg} - T_{r,rz,agg})$$

$$+ 2U_{cond\_wc1,agg}(T_{c1,agg} - T_{r,rz,agg}) \qquad (5.2)$$

$$+ U_{cond\_wc2,agg}(T_{c2,agg} - T_{r,rz,agg})$$

$$C_{c1,agg} \frac{d(T_{c1,agg})}{dt}$$

$$= 2U_{cond\_wc1,agg}(T_{r,rz,agg} - T_{c1,agg}) \qquad (5.3)$$

$$+ U_{cond\_c1c3,agg}(T_{c3,agg} - T_{c1,agg})$$

$$C_{c2,agg} \frac{d(T_{c2,agg})}{dt}$$

$$= U_{cond\_wc2,agg}(T_{r,rz,agg} - T_{c2,agg})$$

$$+ 2U_{cond\_c2c3,agg}(T_{c3,agg} - T_{c2,agg}) \qquad (5.4)$$

$$+ U_{cond\_c2f1,agg}(T_{flo1,agg} - T_{c2,agg})$$

$$C_{c3,agg} \frac{d(T_{c3,agg})}{dt}$$

$$= 2U_{cond\_c2c3,agg}(T_{c2,agg} - T_{c3,agg})$$

$$+ U_{cond\_c1c3,agg}(T_{c1,agg} - T_{c3,agg})$$

$$+ U_{cond\_c3f2,agg}(T_{flo2,agg} - T_{c3,agg})$$

(5.5)

$$C_{flo1,agg} \frac{d(T_{flo1,agg})}{dt}$$

$$= U_{cond\_c2f1,agg}(T_{c2,agg} - T_{flo1,agg})$$

$$+ 2U_{cond\_f1f2,agg}(T_{flo2,agg} - T_{flo1,agg})$$

$$+ U_{cond\_f1sf1,agg}(T_{sf1,agg} - T_{flo1,agg})$$

(5.6)

$$C_{flo2,agg} \frac{d(T_{flo2,agg})}{dt}$$

$$= U_{cond\_c3f2,agg}(T_{c3,agg} - T_{flo2,agg})$$

$$+ 2U_{cond\_f1f2,agg}(T_{flo1,agg} - T_{flo2,agg})$$

$$+ U_{cond\_f2sf2,agg}(T_{sf2,agg} - T_{flo2,agg})$$

(5.7)

$$\frac{d(T_{sf1,agg})}{dt} = T_{flo1,agg} - \left(\frac{q_{r1,agg}}{U_{cond\_f1sf1,agg}}\right) - \left(\frac{q_{c1,agg}}{U_{cond\_f1sf1,agg}}\right)$$

(5.8)

$$\frac{d(T_{sf2,agg})}{dt} = T_{flo2,agg} - \left(\frac{q_{r2,agg}}{U_{cond\_f2sf2,agg}}\right) - \left(\frac{q_{c2,agg}}{U_{cond\_f2sf2,agg}}\right)$$

(5.9)

Commercial zone air aggregated model:

$$
\begin{aligned}
C_{cz,agg} \frac{d(T_{z,cz,agg})}{dt} \\
= c_w m_{w,cz,agg}(T_{s,cz,agg} - T_{r,cz,agg}) \\
- A_{czwin,agg} U_{win}(T_{z,cz,agg} - T_o) \\
- A_{czwall,agg} U_{wall}(T_{z,cz,agg} - T_o) \\
- \frac{ACH_{cz} * Vol_{cz,agg} * c_a * \rho_a * (T_{z,cz,agg} - T_o)}{3600} - Q_{agg,int,cz} \\
+ Q_{agg,sol,cz}
\end{aligned}
\tag{5.10}
$$

Baseboard heater aggregated model:

$$
\begin{aligned}
C_{htr,agg} \frac{d(T_{htr,agg})}{dt} \\
= c_w m_{w,cz,agg}(T_{s,cz,agg} - T_{r,cz,agg}) \\
- U_{htr,agg} \left(\frac{T_{s,cz,agg} + T_{r,cz,agg}}{2} - T_{z,cz,agg} \right)^{1+n}
\end{aligned}
\tag{5.11}
$$

Boiler heat exchanger aggregated model:

$$
C_{bhxp,agg} \frac{d(T_{r,bhxp,agg})}{dt} = c_w m_{w,bhxp,agg}(T_{bhxmix,agg} - T_{r,bhxp,agg}) - q_{bhx}
\tag{5.12}
$$

$$
C_{bhxs,agg} \frac{d(T_{s,bhxs,agg})}{dt} = q_{bhx} - c_w m_{w,rzr,agg}(T_{s,bhxs,agg} - T_{shx,agg})
\tag{5.13}
$$

$$
q_{bhx} = \varepsilon_{bhx}(m_{w,bhx,agg} C_p)_{min}(T_{bhxmix,agg} - T_{shx,agg})
\tag{5.14}
$$

$$
\begin{aligned}
\frac{d(T_{bhxmix,agg})}{dt} \\
= \frac{u_{bhx} m_{w,bhx,agg} T_{s,bhx,agg} + (1 - u_{bhx}) m_{w,bhx,agg} T_{r,bhxp,agg}}{u_{bhx} m_{w,bhx,agg} + (1 - u_{bhx}) m_{w,bhx,agg}}
\end{aligned}
\tag{5.15}
$$

Solar system aggregated model:

$$C_{sc,agg} \frac{d(T_{sco,agg})}{dt} = q_{sct} - c_f m_{f,sc,agg}(T_{sco,agg} - T_{tank,agg}) \qquad (5.16)$$

$$C_{tank,agg} \frac{d(T_{tank,agg})}{dt}$$
$$= q_{soalr,useful} - c_w m_{w,shxp,agg}(T_{tank,agg} - T_{r,shxp,agg}) \qquad (5.17)$$
$$- U_{tank} A_{tank}(T_{tank,agg} - T_a)$$

$$C_{shxp,agg} \frac{d(T_{r,shxp})}{dt} = c_w m_{w,shxp}(T_{tank,agg} - T_{r,shxp,agg}) - q_{shx} \qquad (5.18)$$

$$C_{shxs,agg} \frac{d(T_{shx,agg})}{dt} = q_{shx} - c_w m_{w,shxs}(T_{shx,agg} - T_{r,rz,agg}) \qquad (5.19)$$

$$q_{shx} = \varepsilon_{shx}(m_{w,shx,agg} C_p)_{min}(T_{tank,agg} - T_{r,rz,agg}) \qquad (5.20)$$

Boiler aggregated model:

$$C_{b,agg} \frac{d(T_{s,b,agg})}{dt}$$
$$= u_f m_{fmax} HV e_b - m_{w,br,agg} c_w(T_{s,b,agg} - T_{r,b,agg}) \qquad (5.21)$$
$$- a_j(T_{s,b,agg} - T_{ambient})$$

$$\frac{d(T_{r,b,agg})}{dt} = \frac{m_{w,bhx,agg} T_{r,bhxb,agg} + m_{w,cz,agg} T_{r,czb,agg}}{m_{w,bhx,agg} + m_{w,cz,agg}} \qquad (5.22)$$

Pipe distribution system aggregated model:

$$C_{pipe,bcz,agg} \frac{d(T_{s,cz,agg})}{dt}$$
$$= c_w m_{w,cz,agg}(T_{s,b,agg} - T_{s,cz,agg}) \qquad (5.23)$$
$$- U_{pipe,loss1}(T_{s,b,agg} - T_{ground})$$

$$C_{pipe,czb,agg} \frac{d(T_{r,czb,agg})}{dt}$$

$$= c_w m_{w,cz,agg}(T_{r,cz,agg} - T_{r,czb,agg}) \qquad (5.24)$$

$$- U_{pipe,loss2}(T_{r,cz,agg} - T_{ground})$$

$$C_{pipe,bbhx,agg} \frac{d(T_{s,bhx,agg})}{dt}$$

$$= c_w m_{w,bhx,agg}(T_{s,b,agg} - T_{s,bhx,agg}) \qquad (5.25)$$

$$- U_{pipe,loss1}(T_{s,b,agg} - T_{ground})$$

$$C_{pipe,bhxb,agg} \frac{d(T_{r,bhxb,agg})}{dt}$$

$$= c_w m_{w,bhx,agg}(T_{r,bhxp,agg} - T_{r,bhxb,agg}) \qquad (5.26)$$

$$- U_{pipe,loss2}(T_{r,bhxb,agg} - T_{ground})$$

To validate the substitutability of the above reduced-order model, open loop tests were conducted, and the results were compared with the responses from the full-order model. Open loop test results are plotted in Figures 5.2.1 and 5.2.2. As can be seen from the figures, both the zone temperatures and supply water temperatures from the aggregated model match reasonably well with the full-order model responses. The discrepancy is negligible. The aggregated model mimics the full order model well as such it was used in the energy optimization study.
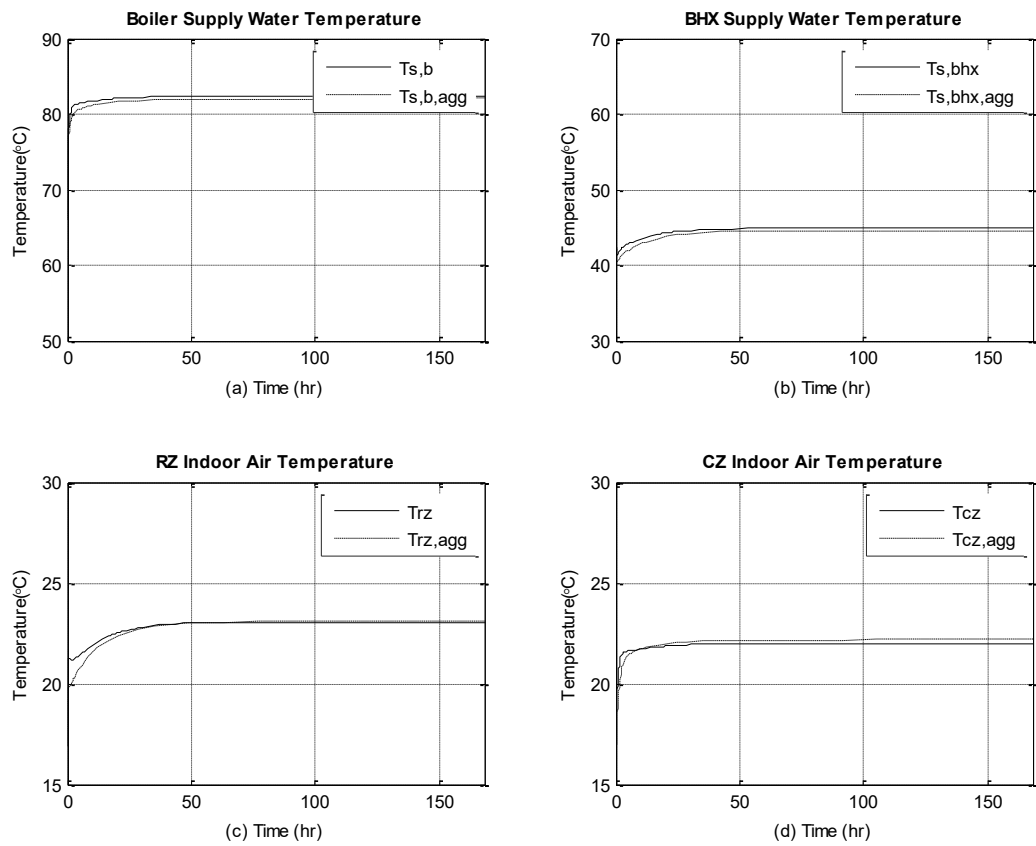
Figure 5.2.1 Open-loop test comparison between the simplified aggregated model and the full-

order detailed model in supply water and zone temperatures
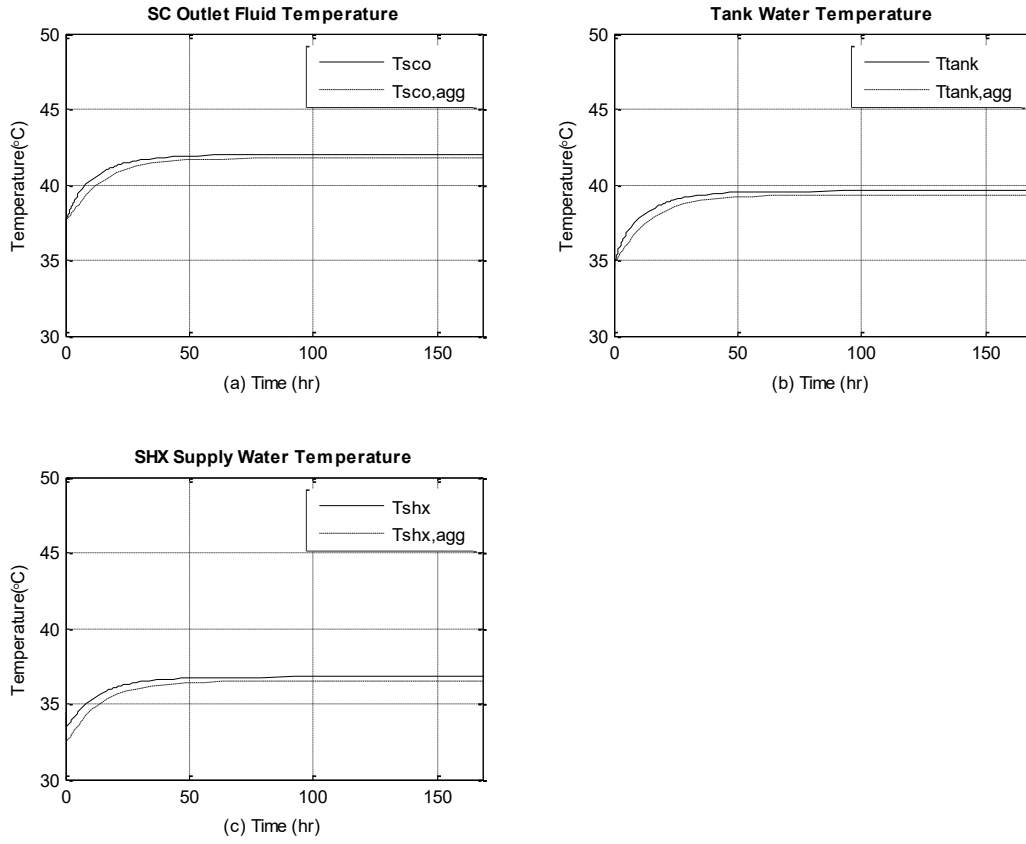
Figure 5.2.2 Open-loop test comparison between the simplified aggregated model and the full-order detailed model in solar system temperatures

5.3 Optimization method

The simplified aggregated model of solar-assisted hydronic space heating system in steady state condition can be written as below:

$$f(x, u_f, u_{bhx}, u_{w,cz}, u_{w,rz}, T_o, G) = 0 \tag{5.27}$$

$$x_0 = x|_{t=0} \tag{5.28}$$

Where x is the state vector, $x = \left[T_{z,rz}, T_{z,cz}, T_w, T_{c1}, T_{c2}, T_{c3} \cdots T_{tank}, T_{shx}, T_{bhx}, T_{s,b}, T_{r,b}\right]$ and x_0 is the initial conditions of each variable. The minimized objective function is setup based on three main considerations: (1) both zone's (commercial and residential zones) indoor air temperatures should be maintained around their corresponding set-points, (2) the state vector x cannot exceed their upper and lower limits, (3) the boiler energy input should be minimized. To this end, the objective function J was expressed as below:

$$J = u_f m_{fmax} HV e_b + \alpha \left(T_{z,rz,agg} - T_{z,rz,set}\right)^2 + \beta \left(T_{z,cz,agg} - T_{z,cz,set}\right)^2 \qquad (5.29)$$

The optimization problem is solved by using the function $f_{mincon}(J)$ in MATLAB. The relationships of the optimized boiler, boiler heat exchanger and solar heat exchanger supply water temperatures versus the outdoor air temperature and solar irradiance are plotted in Figure 5.3.1.
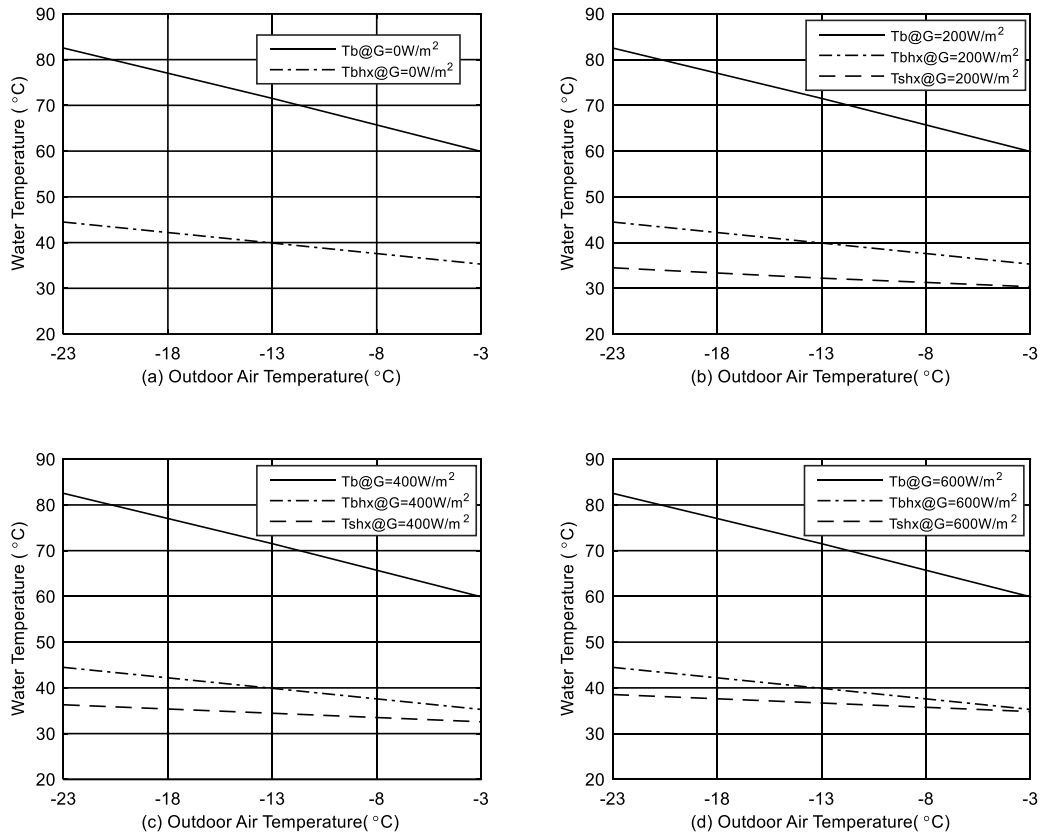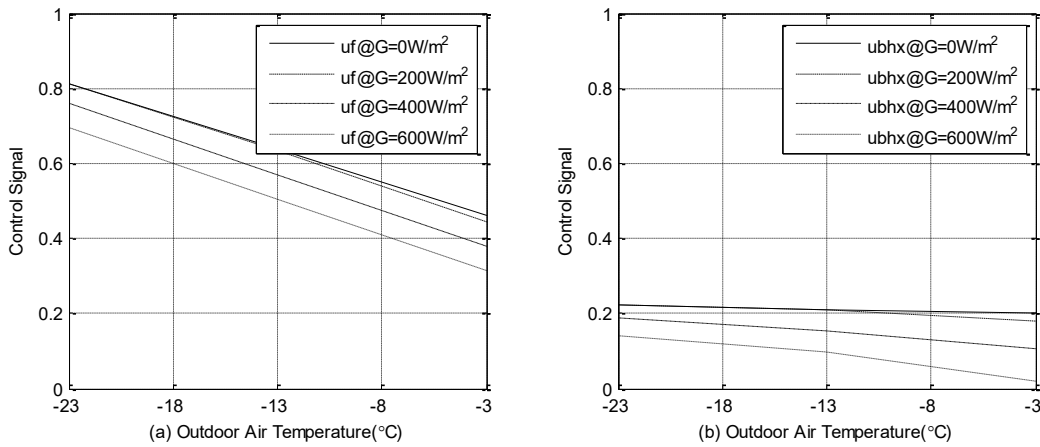
Figure 5.3.1 Optimized supply water temperature profile for boiler, BHX and SHX at different

solar irradiance levels

Figure 5.3.1 shows the optimal supply water temperature profile for the boiler, boiler heat exchanger (BHX) and solar heat exchanger (SHX) as a function of outdoor air temperature at three different solar irradiance levels. In general, the simulation results indicate that the set-point temperatures decrease as the outdoor air temperature increases. Figure 5.3.1 (a) shows the optimized supply water temperatures with no solar irradiance. It can be seen that the temperature curves show a decreasing trend with the rising outdoor air temperature. However, the SHX supply water temperature curve is absent in this figure, because there is no available solar energy to use. The entire solar system is turned off in this case. All the return water from the radiant floors will

pass through the BHX heat exchanger. The sub-figures (b) and (c), show three optimized supply water temperatures under different solar irradiance levels. When the simulated solar radiation level is increased, the SHX supply water temperature shows an upward trend which means higher outdoor solar irradiance level can contribute more energy to the system. From sub-figure (d) it can be noted that, when the simulated solar irradiance and the outdoor air temperature reach a certain point, the two supply water temperature curves of the SHX and BHX intersect. It is the balance point which means under this condition, the solar system can work independently to feed the residential zones load without drawing any energy from the boiler. All radiant floor return water can be heated to its set-point by passing it through the SHX heat exchanger.

Figure 5.3.2 Optimized supply water control signal profile for boiler, BHX and SHX at different solar irradiance levels

Figure 5.3.2 shows the control signal of the boiler and BHX controllers under different solar irradiance levels. It can be noticed that the control signals decrease as the outdoor air temperature increases. Also, the control signals decrease as the solar irradiance level increases. In

chapter 6, these optimal set-points will be implemented on the full-order system using GSA PI controllers and energy simulations will be performed to determine energy savings due to optimal set-points compared to constant set-points. Here in this chapter, the optimal set-points will be implemented on the aggregated model with PI controllers to get preliminary energy savings obtained through the use of optimal set-points on two typical days with assumed outdoor air temperature profiles.

5.4   Aggregated model simulation

In order to study the impact of optimal set-points on the energy performance of the system, simulation runs were conducted by implementing the PI controllers on the aggregate model. Being simple, the aggregate model gives quick estimates of energy savings. To this end, two different load conditions are considered in the simulation: a mild and a warm day conditions. In mild day condition, the assumed outdoor temperatures range between -13°C to -3°C. For the warm day condition, the simulated outdoor temperature varies between -3°C to 7°C. The system responses under mild day condition are plotted in Figures 5.4.1 and 5.4.2. Moreover, the energy simulations under two different operation strategies are conducted: an optimal set-point PI control versus constant set-point PI control. The energy comparisons are presented in Table 5.4.1.
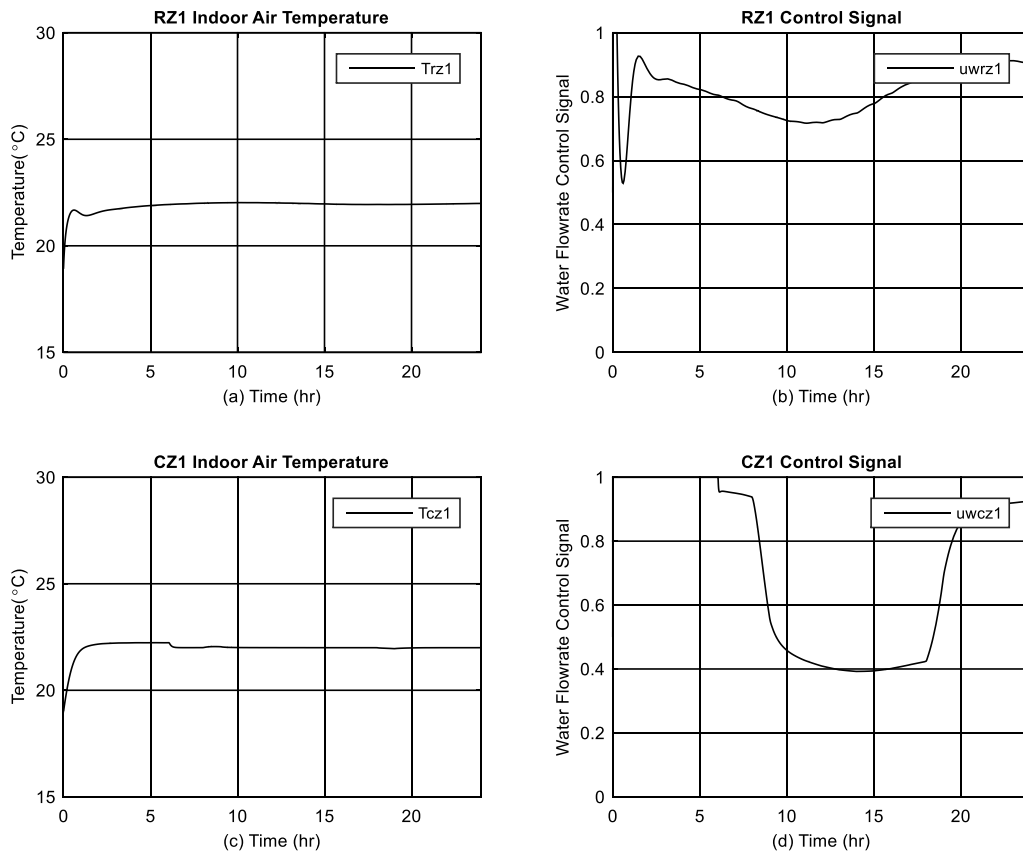
Figure 5.4.1 System responses of optimal PI control for residential and commercial zones under

mild day condition
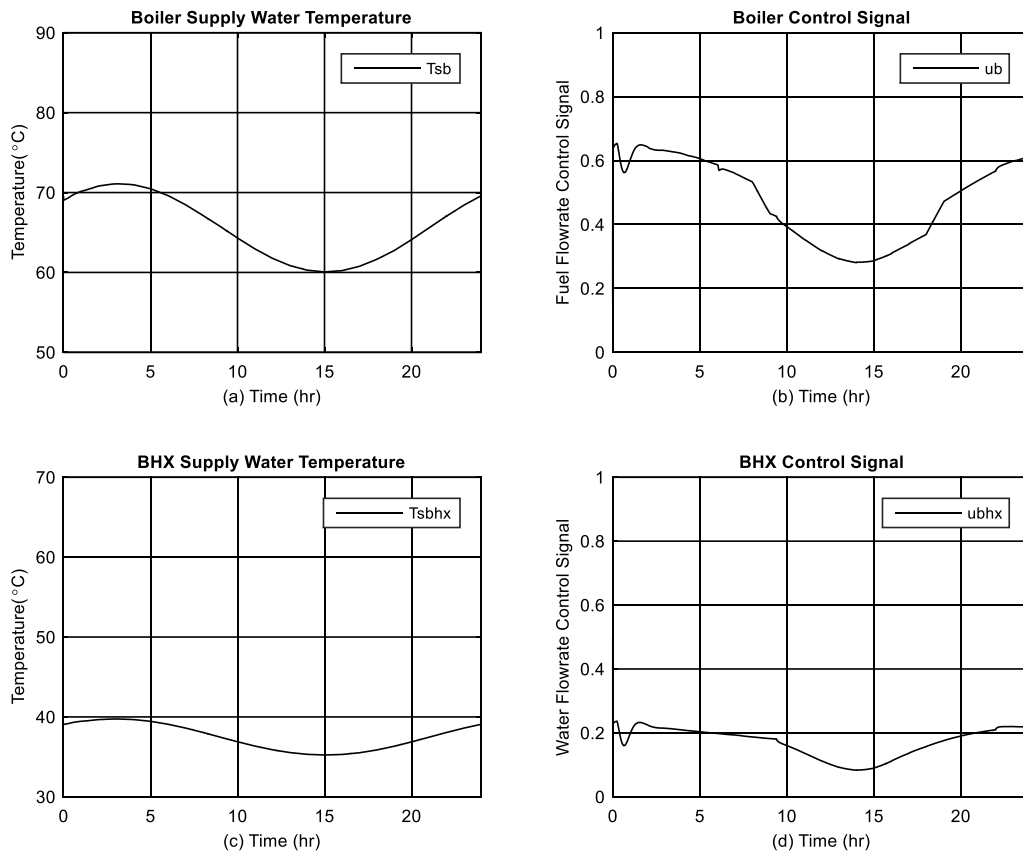
Figure 5.4.2 System responses of optimal PI control for boiler and BHX under mild day

condition

As can be seen from Figure 5.4.1 and 5.4.2, all PI controllers are working well when subjected to diurnal load changes. The residential and commercial zone temperatures remained at their respective set-points throughout the day. Besides, the boiler and BHX supply water temperatures are tracking their optimal set-points well.

Control and operation strategy	Conventional constant set-point PI control	Optimal set-point PI control	Boiler energy saving (%)
Simulated condition: mild day condition			
Boiler demand (MJ)	1031.1	958.83	7.01
Simulated condition: warm day condition			
Boiler demand (MJ)	689.19	586.74	14.87

Table 5.4.1 Boiler demand comparisons between conventional PI and optimal PI control in two

different load conditions

It can be seen from Table 5.4.1 the boiler energy consumption is decreased by around 7% during the mild day condition. However, in the warm day, the boiler saving can rise up to 14.87%. This is because on a warm day the optimal boiler supply water temperature is lower thus resulting in lower energy consumption. A lower supply water temperature can contribute to less boiler heat loss, less heat loss from the piping system, and improved boiler efficiency. In summary, preliminary results with the aggregate model show that by implementing optimal set-points energy savings of the order of 7 to 15% can be achieved. This will be further investigated in the next chapter by conducting weekly energy simulation runs using TMY weather data as input to the full-order system model operated by GSA PI controllers.

CHAPTER 6 SYSTEM ENERGY SIMULATION AND SOLAR ENERGY UTILIZATION

6.1   Introduction

As shown in Chapter 5, the aggregate model energy simulations predicted between 7% to 15% energy savings due to the implementation of optimal set-points versus constant set-point. Furthermore, these simulations were done with PI control on a day with an assumed outdoor air temperature profiles. It is of interest to verify the energy savings potential of optimal set-points implemented on the full-order model with GSA PI controllers. The simulation runs will be conducted over a period of one week using the measured (TMY) weather data [7] as described in this chapter. To this end, the solar-assisted hydronic space heating system energy consumption and solar utilization factor were determined by carrying out simulation runs under two different outdoor conditions. The objective is to compare the energy performance of the overall system, and the energy contribution of the solar system under different control strategies.

6.2   TMY energy simulation

To explore the solar energy contribution to the energy consumption of the overall system, simulation runs were conducted with the full-order model over a period of one week using measured data. The outdoor temperatures and solar irradiance are based on field collected data, which are extracted from the source "Engineering Climate Dataset, Canadian Weather Year for Energy Calculation."

One Week Outdoor Air Temperature in December

One Week Solar Radiation in December
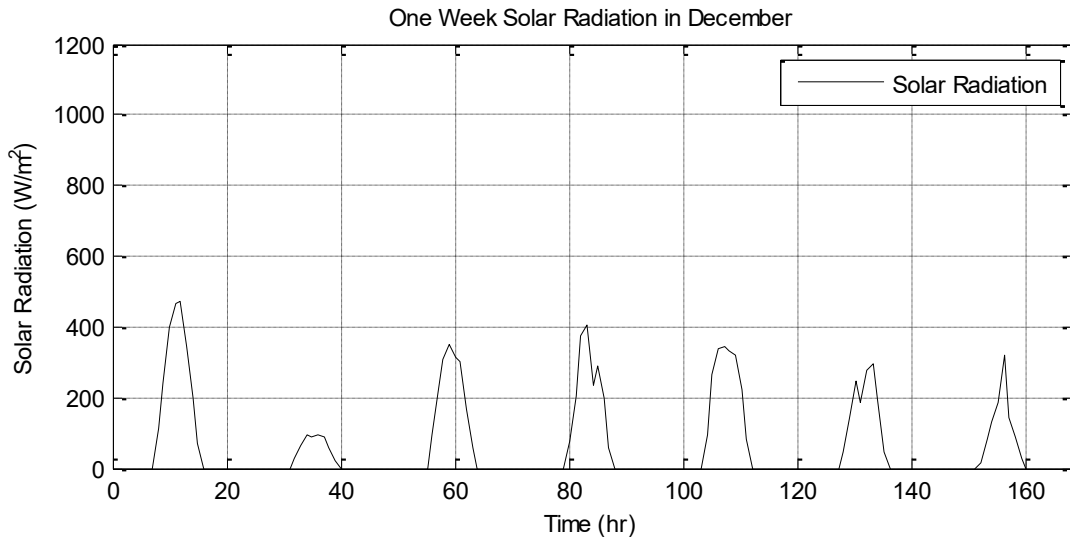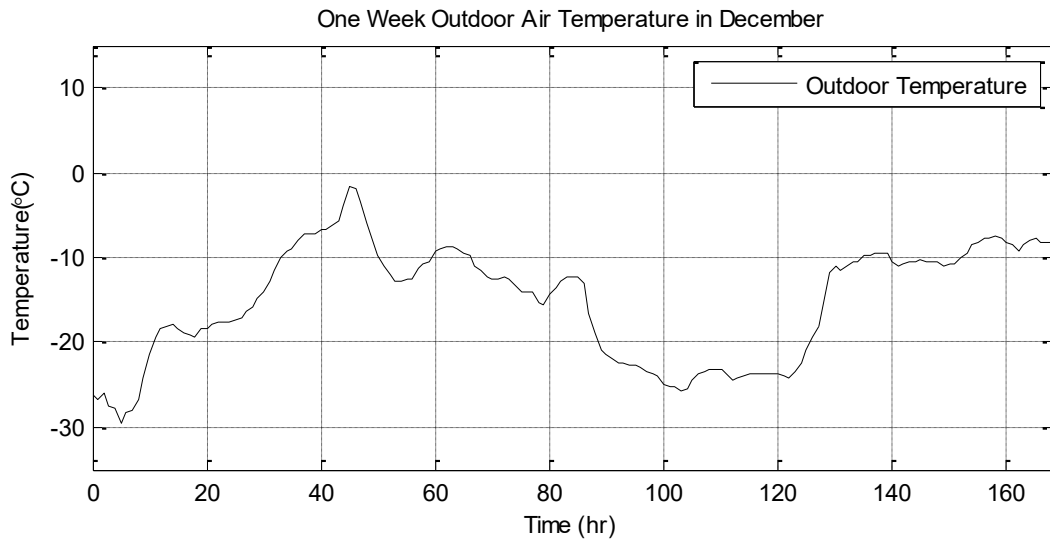
Table 6.2.1 One-week outdoor air temperature and solar irradiance in December based on TMY

Figure 6.2.1 shows the simulated period of one week cold conditions in Montreal starting from December 21st to 27th. Another Figure 6.2.2 is the warm week conditions starting from March 21st to 27th. Based on the data from the typical meteorological year (TMY), the lowest outdoor temperature in December is nearly approaching to -30°C and the highest temperature is around 0°C. The temperature fluctuation is large and the weekly average temperature is around -17°C.

95

However, the recorded data of March based on TMY shows that the temperature range is much smaller than in December. The weekly average outdoor air temperature is about 2°C. In addition, when comparing the weekly solar radiation for both months, it is obvious that the peak solar intensity and the weekly average solar intensity in TMY-March is much higher than in TMY-December. The peak solar radiation is about 900 watts per square meter in March. However, in December, the peak solar radiation intensity is only around 500 watts per square meter.
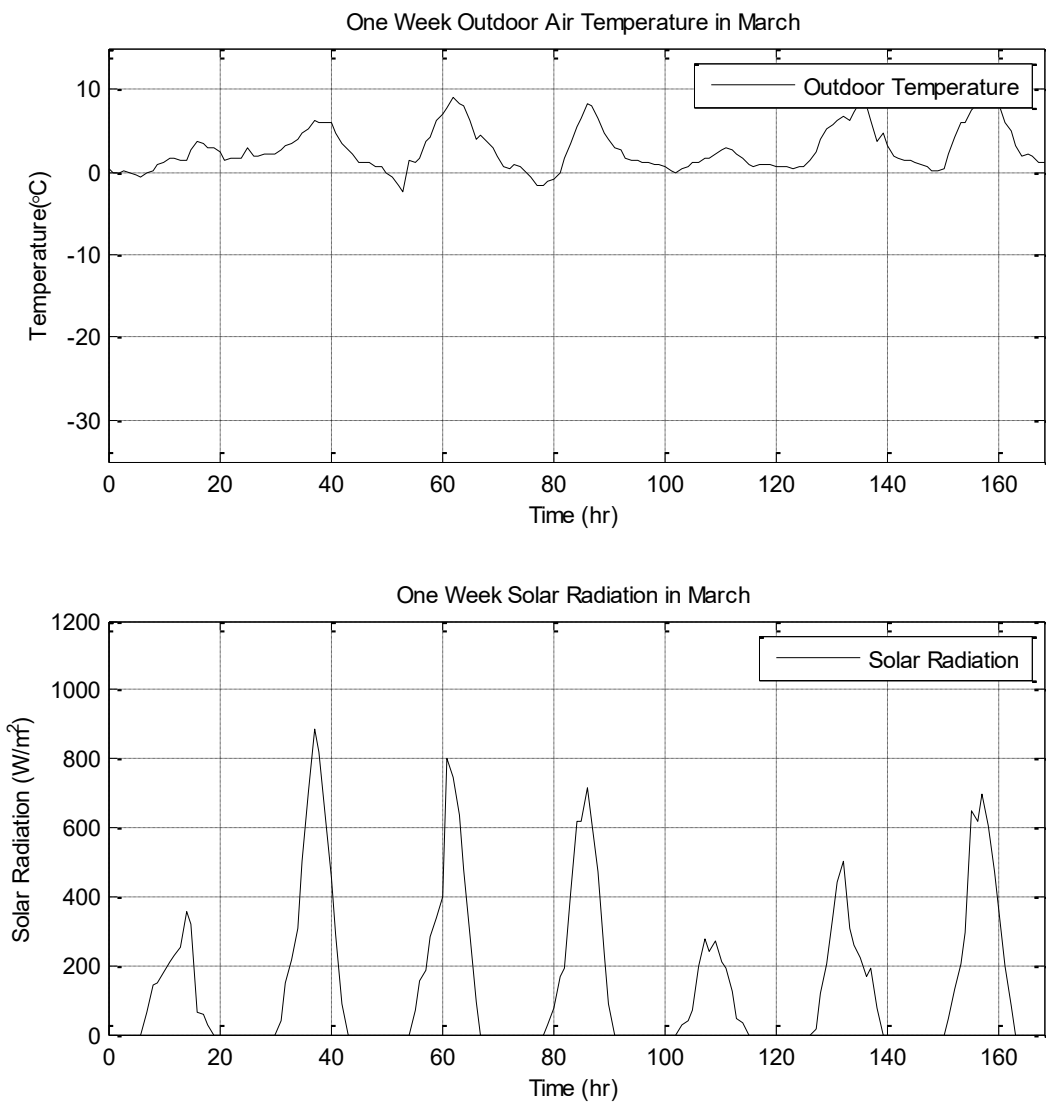
Table 6.2.2 One-week outdoor air temperature and solar irradiance in March based on TMY

For making energy comparisons, a base case system was established. In this base case system, the boiler supplies heat to the entire building consisting of residential and commercial zones. The energy consumption of the all boiler base case system controlled by conventional constant gain PI controllers for a period of one week each in the month of December and March are shown in the second column in Table 6.2.3. As expected the weekly boiler energy consumption is much less in the month of March compared with the month of December. By comparing the weekly energy consumption of the solar-assisted hydronic space heating system with the all boiler base case system, using the same fixed set-point constant gain PI control strategy, it can be noted that the solar-assisted hydronic system saves 0.73% and 16.94% (fourth column in Table 6.2.3) of the boiler energy in the months of December and March, respectively. The results indicate that the solar-assisted hydronic space heating system is more energy efficient in warmer weather conditions. During the cold week conditions, due to colder outdoor air temperature, relatively lower and uncertain solar irradiance level, the solar system provides lower energy savings.

The last set of energy comparisons consisted of energy savings obtained from the solar-assisted hydronic heating system operated with GSA PI controllers using the optimal set-points versus the energy consumption of all boiler base case system. The results are presented in the last column in Table 6.2.3. It can be noted from the results that by implementing the gain scheduling adaptive (GSA) PI control strategy, the solar contribution shows a noticeable improvement in both cold and warm weather conditions. Especially in the month of March. The optimal set-point for BHX, which is the residential zone supply water temperature heat exchanger, contributes to lower supply water temperatures to the radiant floor heating system which helps lower the solar tank water temperature, This can improve the efficiency of the flat-plate solar collector resulting in more solar utilization of 5.71% in the month of December and 30.36% in the month of March,

respectively. By comparing the energy savings obtained with optimal set-point GSA PI control with the constant set-point PI control it can be noted that higher energy savings were obtained with optimal set-point GSA PI control strategy. This is not only due to the use of optimal set-points but also due to good set-point tracking property of GSA PI control strategy.

System	Conventional boiler heating	Solar-assisted heating	Solar fraction (%)	Solar-assisted heating	Solar fraction (%)
Control and operation strategy	Conventional PI control	Conventional PI control		Optimal GSA PI control	
Simulated condition: one week in TMY December condition					
Boiler energy supplied to rzs (MJ)	3239.1	3215.6	0.73	3054.7	5.71
Simulated condition: one week in TMY March condition					
Boiler energy supplied to rzs (MJ)	1769.6	1469.9	16.94	1232.3	30.36

Table 6.2.3 Solar fraction comparisons among conventional PI, optimal PI and optimal GSA PI control strategies in two different load conditions

CHAPTER 7 CONCLUSIONS, CONTRIBUTIONS AND RECOMMENDATIONS FOR FUTURE RESEARCH

7.1 Conclusions and contributions

The development of a dynamic model, design of control strategies, model-based optimization and energy performance simulations for the solar-assisted hydronic space heating system have been presented in this study. The conclusions and contributions are presented in the following sections: dynamic modelling, design of control strategies, optimization and energy performance simulations.

7.1.1 Dynamic modeling

A dynamic model of a solar-assisted hydronic space heating system is developed. The integrated model consists of individual models of components which include a boiler, heat exchangers, a flat-plate solar collector, a water storage tank, baseboard heaters and radiant floor heating system. The following specific conclusions are drawn from the model development study.

1. The solar-assisted hydronic space heating system model developed in this study shows a design method of integrating a high temperature baseboard heating system, a medium temperature solar-storage system and a low temperature radiant floor system to meet the space heating needs of a multi-functional building by incorporating a sustainable solar energy system in a conventional gas-fired boiler hydronic space heating system.

2. The integrated system responses show multiple time scale processes. The solar storage tank system responses are the slowest in the overall system, followed by the residential zone radiant floor system, and the boiler and the commercial zone baseboard system.

3. The overall system dynamic responses include substantial coupling effects among the sub-system heat transfer processes. The multi-time scale system dynamics could contribute significant interactions among the closed control loops of the system.

7.1.2 Design of control strategies

A conventional PI control and a gain-scheduling adaptive PI control strategies are developed for the overall system and the control performance of the control strategies are compared. Some specific conclusion includes:

1. An overall hybrid control structure is designed for the system. It consists of on-off controls for the solar system and modulating controls for the boiler, boiler heat exchanger, residential and commercial zone control loops.

2. A well-tuned conventional PI controller is able to provide acceptable temperature regulation under a limited range of load changes acting on the system.

3. However, under unknown and large variations in disturbances, it is shown that a constant gain PI controller shows large oscillations in temperature responses and poor tracking of set-point temperature.

4. To avoid interactions among the multiple control loops, minimize frequent controller tuning and achieve good control performance over a wide range of variations in space heating loads, a gain-scheduling adaptive gain PI control strategy is proposed.

5. The simulation results show that the GSA PI controllers give a better set-point tracking performance compared to the constant gain PI control in the aspect of disturbance rejection or maintaining stable operation of the system.

7.1.3   Optimization and energy performance simulations

An aggregated model was developed for optimizing the system energy performance. A model based multi-variable constraint optimization problem was formulated and solved to determine optimal supply water temperature set-points. The aggregated model was used to determine preliminary daily energy savings with assumed outdoor air temperature profiles and optimal set-points. The results showed that between 7 to 15% of energy could be saved under mild and warm weather conditions, respectively. To get better estimates of energy savings, the optimal set-points were implemented on the full-order model using GSA PI control strategy. Weekly energy consumption using TMY weather data were compared with an all boiler heating system which was used as a base case system. The results show that:

1. Weekly energy simulations based on typical meteorological year (TMY) data for Montreal were conducted during cold weather (December) and mild weather (March) conditions. The simulation results with the constant set-point PI control strategy showed that the solar system does not contribute greatly to energy savings under cold weather conditions. However, the solar system contributed 16.94% to the boiler energy savings in mild weather (March) conditions.

2. By implementing the optimal set-point GSA PI control strategy, it was shown that higher energy savings can be achieved. The results showed that solar fractions of 5.71%

and 30.36% as compared to the all boiler base case system can be achieved in the month of December and March, respectively.

3. The difference between the energy consumptions with optimal set-point GSA PI control and constant set-point PI control is due to the use of optimal set-points and as well as due to good tracking property of GSA PI control compared to constant gain PI control.

4. The results show that that the GSA PI control is an effective control strategy well suited for systems with multiple control loops and in systems with a hybrid control structure.

7.2   Recommendations for future research

1) Solar energy utilization fraction is dependent on outdoor temperatures and solar irradiance levels. Unlike other available sources such as geothermal energy, the available solar energy is uncertain. To this end, it is important to design a long-term solar energy storage system to improve the useful solar fraction in hydronic space heating systems.

2) Dynamic optimization method should be studied and implemented into the current system to develop more advanced control and operation strategies.

REFERENCES

[1] Arinze, E., Schoenau, G., & Sokhansanj, S. (1993). A dynamic performance simulation model of flat-plate solar collection for a heat pump system. *Energy Conversion and Management, 34*, 33-49.

[2] Bai, J., & Zhang, X. (2007). A new adaptive PI controller and its application in HVAC systems. *Energy Conversion and Management, 48*, 1043-1054.

[3] Cadafalch, J. (2009). A detailed numerical model for flat-plate solar thermal devices. *Solar Energy, 83*, 2157-2164.

[4] Candanedo, J., Allard, A., & Athienitis, A. (2011). Predictive control of radiant floor heating and transmitted irradiance in a room with high solar gains. *ASHRAE Transactions. 117*, pp. 652-665. Montreal: ASHRAE.

[5] Cho, S., Hong, S.-k., Li, S.-c., & Zaheeruddin, M. (2013). An optimal predictive control strategy for radiant floor district heating system: Simulation and experimental study. *Building Service Engineering Research & Technology, 0*(0), 1-21.

[6] Duffie, J., & Beckman, W. (2013). *Solar engineering of thermal processes* (Fourth ed.). Hoboken, New Jersey: John Wiley & Sons, Inc.

[7] Government of Canada. (2018). *Engineering Climate Datasets*. Retrieved from http://climate.weather.gc.ca/prods_servs/engineering_e.html

[8] Haddad, K. (2011). Solar energy utilization of a residential radiant floor heating system. *ASHRAE Transactions. 117*, pp. 79-86. Las Vegas: ASHRAE.

[9] Haddad, K., Purdy, J., & Laouadi, A. (2007). Comparison of the performance of a forced-air and a radiant floor residential heating system connected to solar collectors. *Journal of Solar Energy Engineering, 129*, 465-472.

[10] Huang, B., & Ko, P. (1994). A system dynamic model of fire-tube shell boiler. *Journal of Dynamic Systems, Measurement and Control, 116*(745).

[11] Kang, C.-S., Hyun, C.-H., & Park, M. (2015). Fuzzy logic-based advanced on–off control for thermal comfort in residential buildings. *Applied Energy, 155*, 270-283.

[12] Kazeminejad, H. (2002). Numerical analysis of two dimensional parallel flow flat-plate solar collector. *Renewable Energy, 26*, 309-323.

[13] Li, Hu, & Karava. (2015). System identification and model predictive control of office buildings with integrated photovoltaic-thermal collectors, radiant floor heating and active thermal storage. *Solar Energy*, 139–157.

[14] Li, L., Zaheeruddin, M., Cho, S.-H., & Jung, S.-H. (2010). Steady state and dynamic modeling of an indirect district heating system. *International Journal of Air-Conditioning and Refrigeration, 18*, 61-75.

[15] Li, S., Joe, J., Hu, J., & Karava, P. (2014). Modeling and predictive control of high performance building with distributed energy generation and thermal storage. *Solar Energy, 113*, 139-157.

[16] Liao, Z., & Parand, F. (2002). A dynamic model of commercial gas and oil burned boilers. *Advances in Building Technology* (pp. 1249-1256). Hong Kong: Elsevier.

[17] Liu, J. (2014). Dynamic modeling and gain scheduling control of a chilled water cooling system. *Energy Research Journal, 5*(1), 4-16.

[18] Ma, Y., & Zaheeruddin, M. (2018). Dynamic modeling, adaptive control and energy performance simulation of a hybrid hydronic space heating system. *Building Services Engineering Research & Technology, 39*(4), 406-429.

[19] Natural Resources Canada's Office of Energy Efficiency. (2013). *Energy efficiency trends in Canada 1990 to 2013*. Retrieved from Natural Resources Canada: https://www.nrcan.gc.ca/energy/publications/19030

[20] Natural Resources Canada's Office of Energy Efficiency. (2016). *Energy Use Data Handbook Tables*. Retrieved from Natural Resources Canada: http://oee.nrcan.gc.ca/corporate/statistics/neud/dpa/menus/trends/handbook/tables.cfm

[21] Ning, M., & Zaheeruddin, M. (2010). Neuro-optimal operation of a variable air volume HVAC&R system. *Applied Thermal Engineering, 30*, 385-399.

[22] Qu, G., & Zaheeruddin, M. (2004). Real-time tuning of PI controllers in HVAC systems. *International journal of energy research, 28*, 1313-1327.

[23] Saleh, A. (2012, May). *Modeling of flat-plate solar collector operation in transient states*. Fort Wayne: Purdue University.

[24] Seem, J. (1998). A new pattern recognition adaptive controller with application to the HVAC system. (Elsevier, Ed.) *Automatica, 34*(8), 969-982.

[25] Singh, G., Zaheeruddin, M., & Patel, R. (2000). Adaptive control of multivariable thermal processes in HVAC systems. *Energy Conversion & Management, 41*, 1671-1685.

[26] Sobhansarbandi, S., & Atikol, U. (2015). Performance of flat-plate and compound parabolic concentrating solar collectors in underfloor heating system. *Journal of Solar Energy Engineering, 137*(034501), 1-4.

[27] U.S. Energy Information Administration. (2011). *Annual Energy Review* . Retrieved from https://www.eia.gov/totalenergy/data/annual/pdf/aer.pdf

[28] World Business Council for Sustainable Development. (2009). *Transforming the Market: Energy Efficiency in Buildings*. Retrieved from https://www.wbcsd.org/Programs/Cities-and-Mobility/Energy-Efficiency-in-Buildings/Resources/Transforming-the-Market-Energy-Efficiency-in-Buildings

[29] Zaheeruddin, M. (1991). Dynamic performance of a sub-optimal controller. *Energy and Buildings, 17*, 117-130.

[30] Zaheeruddin, M., & Zheng, G. (1997). Optimal operation of an embedded-piping floor heating system with control input constraints. *Energy Conversion and Management, 38*, 713-725.

[31] Zaheeruddin, M., Zhang, Z., & Cho, S. (2002). Augmented control strategies for radiant floor heating systems. *International Journal of Energy Research, 26*, 79-92.

[32] Zelzouli, K., Guizani, A., & Sebai, R. (2012). Solar thermal systems performances versus flat plate solar collectors connected in series. *Scientific Research, 4*, 881-893.

[33] Zhang, Z., Pate, M., & Nelson, R. (1988). An investigation of a residential solar system coupled to a radiant panel ceiling. *Journal of Solar Energy Engineering, 110*, 172-179.

APPENDICES

Building Loads and System Design Summary

The building space heating loads, under design day conditions for Montreal, were calculated using ASHRAE steady state design methods. These calculations were done on a zone-by-zone basis. A summary of design day loads for each zone are given in the table in Appendix-A. A gas-fired boiler of 23 kW capacity was selected to provide space heating loads for the entire building as the base case all boiler system. For the residential zones, a radiant floor system was designed based on methods described in reference [18] which corresponds to a typical RFH system design. Due to relatively lower outdoor air temperature and uncertain solar irradiation level in cold months, the solar system was designed to cover 30% of the residential building space heating load. The appropriate size of flat-plate solar collector modules was selected from the manufacturer's catalogue data which is attached in Appendix-B. The total area of the solar collector was 14.3 m^2. The size of solar storage tank was based on the guidelines provided in reference [6]. For the designed system, the storage tank volume was 1071 liters. A summary of design parameters are listed in the table in Appendix-A.

Appendix-A: Design Parameters

Definition	Symbol	Value or Formula	Unit
Design day outdoor condition			
Outdoor design day temperature	T_d	-23	°C
Outdoor design day solar irradiance	G_d	400	W/m^2
Design day heating load calculation			
Commercial zone indoor design temperature	T_{czd}	22	°C
Residential zones indoor design temperature	T_{rzd}	23	°C
Design heating load of total commercial zones	Q_{czt}	9220.3	W
Design heating load of commercial zone 1	Q_{cz1}	4610.1	W
Design heating load of commercial zone 2	Q_{cz2}	4610.1	W
Design heating load of total residential zones	Q_{rzt}	6523.7	W
Design heating load of residential zone 1	Q_{rz1}	1630.9	W

Design heating load of residential zone 2	Q_{rz2}	1630.9	W
Design heating load of residential zone 3	Q_{rz3}	1630.9	W
Design heating load of residential zone 4	Q_{rz4}	1630.9	W
Boiler sizing			
Boiler design capacity	Q_{bd}	23000	W
Baseboard heater heating system sizing			
Commercial zone design supply water temperature	T_{czspd}	83	°C
Commercial zone design return water temperature	T_{rzrd}	63	°C
Heat transfer factor	n	0.3	-
Heat transfer coefficient of baseboard heater 1	U_{htr1}	$U_{htr1} = \dfrac{0.4 * Q_{cz1}}{\left(\dfrac{T_{czspd} + T_{rzrd}}{2} - T_{czd}\right)^{1+n}}$	W/K
Heat transfer coefficient of baseboard heater 2	U_{htr2}	$U_{htr2} = \dfrac{0.3 * Q_{cz1}}{\left(\dfrac{T_{czspd} + T_{rzrd}}{2} - T_{czd}\right)^{1+n}}$	W/K
Heat transfer coefficient of baseboard heater 3	U_{htr3}	$U_{htr3} = \dfrac{0.3 * Q_{cz1}}{\left(\dfrac{T_{czspd} + T_{rzrd}}{2} - T_{czd}\right)^{1+n}}$	W/K

Heat transfer coefficient of baseboard heater 4	U_{htr4}	$U_{htr4} = \dfrac{0.4 * Q_{cz2}}{\left(\dfrac{T_{czspd} + T_{rzrd}}{2} - T_{czd}\right)^{1+n}}$	W/K
Heat transfer coefficient of baseboard heater 5	U_{htr5}	$U_{htr5} = \dfrac{0.3 * Q_{cz2}}{\left(\dfrac{T_{czspd} + T_{rzrd}}{2} - T_{czd}\right)^{1+n}}$	W/K
Heat transfer coefficient of baseboard heater 6	U_{htr6}	$U_{htr6} = \dfrac{0.3 * Q_{cz2}}{\left(\dfrac{T_{czspd} + T_{rzrd}}{2} - T_{czd}\right)^{1+n}}$	W/K
Radiant floor heating system sizing			
Residential zone design supply water temperature	T_{rzspd}	45	°C
Residential zone design return water temperature	T_{rzrd}	35	°C
Interval between tubes of residential zones	S_{rz}	0.4	m
Radiant floor pipe length for each control segment	L_{rz}	25	m
Outer diameter of the tube	D_o	0.0185	m
Inner diameter of the tube	D_i	0.0145	m
Thickness of the concrete	H_c	0.0381	m
Thickness of the flooring	H_{flo}	0.0105	m
Boiler heat exchanger sizing			

BHX primary side design supply water temperature	T_{bhxpsd}	83	°C
BHX primary side design return water temperature	T_{bhxprd}	73	°C
BHX heat transfer coefficient-area	UA_{bhx}	3500	W/°C
Flat-plate solar collector and collector heat exchanger sizing			
Number of flat-plate solar collectors	N_{sc}	5	-
Distance between risers	W_{sc}	0.15	m
Riser diameter	D_{sc}	0.01	m
Each solar collector module mass flow rate	m_{sc}	0.03	kg/s
Length of each solar collector module	L_{sc}	2.38	m
Width of each solar collector module	W_{sc}	1.20	m
Collector heat exchanger heat transfer coefficient-area	UA_{chx}	3500	W/°C
Solar tank and solar heat exchanger sizing			
Volume of solar tank	V_{tank}	0.075	m^3 / m^2

Thermal resistance of solar tank wall	R_{tank}	1.2	m²°K /W
Surface area of solar tank	A_{tank}	15	m^2
Solar heat exchanger heat transfer coefficient-area	UA_{shx}	3500	W/°C
Solar heat exchanger primary side mass flowrate	m_{shxp}	0.06	kg/s

Appendix-B: Flat-plate solar collector data

G SERIES Solar Collectors
Glazed Liquid Flat Plate Collectors
Technical Specifications
SRCC Certification # 100-2006-005A

Thermo Dynamics Ltd.
101 Frazee Avenue
Dartmouth, Nova Scotia
Canada, B3B-1Z4
Tel: (902) 468-1001   Fax: (902) 468-1002
Email: solarinfo@thermo-dynamics.com
www.thermo-dynamics.com

0.086m (3-3/8")
1.27m (50-1/8")
1.20m (47-3/8")
2.47m (97-3/8")
2.38m (93-7/8")

G32

low-iron tempered glass
EPDM glazing gasket
baked enamel (dark brown) aluminum cap stripping
baked enamel (dark brown) aluminum frame
fibreglass insulation
copper header
selective black aluminum-copper absorber
fibreglass insulation
aluminum backing sheet
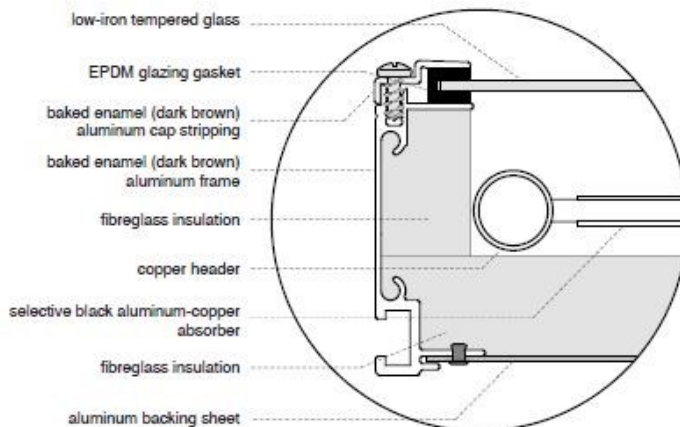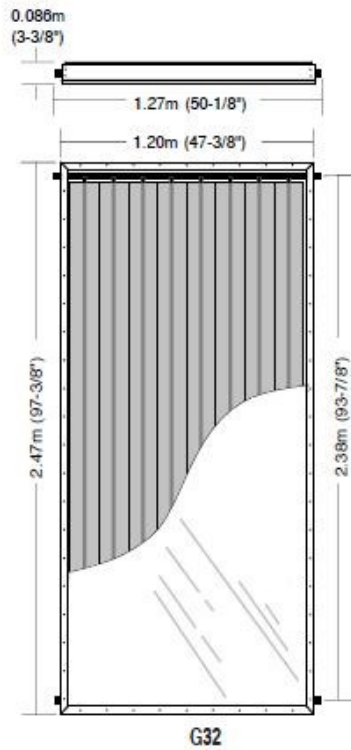
A. General Information

1.0 Product Description:
Thermo Dynamics G Series flat plate liquid collectors are single glazed with low-iron tempered glass. The absorber is an arrangement of parallel riser fins connected to top and bottom headers. The fins are aluminum with integral copper riser tubes, which are completely surrounded by the aluminum and are metallurgically bonded together. The copper riser tubes are soldered to internal manifolds (headers), which are available in either 19 mm (3/4") or 25 mm (1") diameter copper pipe. The back and sides are insulated with a 25 mm (1") layer of compressed fiberglass. The collector frame is extruded aluminum with a baked-enamel finish, (dark brown). Collector mounting is by way of a sliding bolt-track. Flush and racked collector mounting formats are easily accommodated.

1.1 Options:
Factory installed temperature sensors; 19 mm (3/4") and 25 mm (1") headers; 12 mm (1/2") riser tubes; absorber coatings: selective paint surface.

1.2 Dimensions:
1.205 m x 2.475 m x 0.086 m
47-3/8 in x 97-3/8 in x 3-3/8 in
Gross area: 2.982 m² (32.10 ft²)
Aperture area: 2.783 m² (29.96 ft²)
Absorber area: 2.870 m² (30.90 ft²)
Volume (19 mm (3/4") header):
2.3 liter (0.51 IG)
Volume (25 mm (1") header):
3.0 liter (0.66 IG)

1.3 Weight:
Net: 43.5 kg (96 lb)
Shipping: 64 kg (140 lb)
(includes wooden crate)

2.0 Product Use

2.1 Product Applications:
Residential and commercial domestic hot water, process hot water, space heating, pool heating

2.2 Geographic and Climatic Limitations:
None.

2.3 Certifications:
Solar Rating & Certification Corporation (SRCC) #100-2006-005A
http://www.solar-rating.org

Listed by Natural Resources Canada (NRCan) as an acceptable solar collector.
http://www.ecoaction.gc.ca
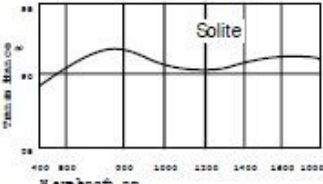
TC.201.05.JAN/09

G Series Collector Technical Specifications; page 1 of 8

G SERIES Solar Collectors

Glazed Liquid Flat Plate Collectors
Technical Specifications
SRCC Certification # 100-2006-005A

3.0 Manufacturer's Experience

3.1 Background:
Thermo Dynamics Ltd. (TDL) is a Canadian company engaged in the research, development, production, distribution and installation of solar thermal equipment. The company has been involved in the solar thermal industry since 1981 and operates from its head office and factory in Dartmouth, Nova Scotia, Canada, the sister city of Halifax situated on the Atlantic coast. The company's specialization is the glazed liquid-flat-plate (LFP) collectors with metal absorbers. TDL is a fully integrated solar thermal company with the ability to convert raw aluminum and copper into a high technology solar water heating system.

Thermo Dynamics Ltd., as a world leader in solar technology, manufactures and markets solar heating equipment from complete systems to basic selective surface components for O.E.M.'s licensees, dealers and distributors through out North America, Europe, Africa, New Zealand, as well as 10 other countries around the world.

3.2 Production:
3000 m² per year for G32 collectors.

3.3 Projects:
Mount Saint Vincent Motherhouse, Halifax, Nova Scotia, Canada. Largest SDHW system in Canada.
Collector type and number: 224 - G32
Collector area: 675 m² (7,265 ft²)
1.75 GJ/m²/year (154 MBtus/ft²/year)

Top of the Mountain Apartments, Halifax, Nova Scotia, Canada.
Collector type and number: 49 - G32; 49 - G40
Collector area: 328 m² (3,531 ft²)
1.78 GJ/m²/year (156 MBtus/ft²/year)

Somerset Place Apartments, Halifax, Nova Scotia, Canada
Collector type and number: 120 - G32
Collector area: 356 m² (3,332 ft²)
2.10 GJ/m²/year (185 MBtus/ft²/year)

Thermo Dynamics Ltd. has installed thousands of solar residential domestic hot water and pool heating systems.

B. Glazing System

1.0 General Description:
Glazing is a 3.2 mm (1/8") single sheet of low-iron tempered glass with an EPDM rubber seal around the edges. Glazing is secured by an aluminum capping fastened by stainless steel screws around the perimeter.

1.1 Trade Names:
Solite

1.2 Chemical Composition:
Iron oxide content of 0.03%

1.3 Physical Treatment:
All glazing is tempered with swiped edges and has a shallow stipple pattern to reduce specular reflectance.

1.4 Thickness:
3.18 mm (1/8")

1.5 Spacing:
Glazing to absorber: 20 to 25 mm (3/4" to 1")

1.6 Weight:
7.8 kg/m² (1.6 lb/ft²)

1.7 Appearance:
Translucent; the inner surface is embossed with a stipple pattern which produces a frosted effect.

2.0 Optical Performance

2.1 Spectral Transmittance:
Visible light 89.8% ASTM E424-71A
Ultra violet light 51% ISO 9050
Solar light/energy 89.5% ASTM E424-71A

2.2 Energy Transmission:
Solar spectrum (0-3 micrometres) 89.5%
Infrared spectrum (>3 micrometres)
No data available

2.3 Refractive Index:
1.525

3.0 Structural Performance

3.1 Tensile Strength:
Design Pressure is 2.87 kPa (.416 psi) for 1/8 inch glass with a design factor of 2.5. Tensile strength is 152 MPa (22,000 psi) with a 2.5 safety factor.

3.2 Impact Resistance:
Glazing can withstand 542 J (400 ft-lb) soft-body impact, 3 to 5 times stronger than annealed glass.

3.3 Uniform Load Resistance:
Uniform load testing was conducted at the National Solar Test Facility in January 2007 as part of CSA-F378-87.
Positive load: 1.5 kPa (0.22 psi)
Negative load: 1.9 kPa (0.28 psi)

4.0 Thermal Performance

4.1 Coefficient of Thermal Expansion:
89.9×10^{-7} 1/°C (49.9×10^{-7} 1/°F)

4.2 Operating Temperature Range:
Min: below -46°C (-51°F); max: 260°C (500°F)

4.3 Thermal Conductivity:
No data available

5.0 Fire Behavior:
Non-combustible. Does not produce toxic fumes in a fire situation.

6.0 Durability:
Glass is chemically inert to most chemical solvents and staining agents, and is resistant to surface weathering, ultraviolet and thermal degradation, and moisture damage.

G SERIES Solar Collectors
Glazed Liquid Flat Plate Collectors
Technical Specifications
SRCC Certification # 100-2006-005A

Thermo Dynamics Ltd.
101 Frazee Avenue
Dartmouth, Nova Scotia
Canada, B3B-1Z4
Tel: (902) 468-1001   Fax: (902) 468-1002
Email: solarinfo@thermo-dynamics.com
www.thermo-dynamics.com

THERMO DYNAMICS LTD.

C. Absorber System

1.0 General Description:
The absorber consists of eight parallel aluminum fins with integral copper riser tubes, which are bonded to and completely surrounded by the aluminum by means of high-pressure cold-rolling process. The absorber coating is slective black paint. The riser/header connection has two parts, a short copper nipple brazed to the header with the absorber fin soldered to the copper nipple.

1.1 Generic/Trade Names:
Absorber fins: "Sunstrip™"
Tubes: copper
Headers: Type M copper
Coating: SOLEC
Solder/Brazing: 95/5 tin antimony/Silfos

1.2 Chemical Composition:
Absorber fins: aluminum (AA 1350/0 alloy)
Tubes: copper (CDA 1220/0 alloy)
Headers: copper
Coating: selective black paint
Solder/Brazing: no data available

1.3 Physical Treatment:
None.

1.4 Dimensions:
Tube diameter: rhombic shape with an open area of about 120 mm² (0.19 in²)
Tube spacing: 143 mm (5.63")
Header diameter: 19 or mm (3/4" or 1") nominal
Absorber thickness: 0.5 mm (0.02")
Coating thickness: no data available.

2.0 Optical Performance

2.1 Absorptivity of Solar Radiation:
Painted surface: $\alpha = 95\%$

2.2 Emissivity of Infrared Radiation:
Painted surface: $\varepsilon = 25\%$

3.0 Thermal Performance

3.1 Thermal Transfer:
Good thermal transfer due to the high conductivity of aluminum and the bond between the aluminum fins and copper tubes.

3.2 Coefficient of Thermal Expansion:
Absorber: no data available
Tubes: no data available
To allow for thermal expansion, the absorber is free to float within the collector container. EPDM gaskets prevent contact between the copper headers and the aluminum container.

3.3 Thermal Capacity of Absorber System:
No data available.

### 3.4 Operating Temperature Range:
Absorber: max. 160°C (320°F)
Tubes: max. 160°C (320°F)
Solder/Brazing: min. -50°C (-58°F); max. 160°C (320°F)
Coating: max. 160°C (320°F)

4.0 Exposure Test:
The collector has completed a 30-day outdoor no-flow exposure test at The National Solar Test Facility (NSTF), Mississauga, Canada, June 2006. The test was in accordance to CAN/CSA F378-87. The test includes a preconditioning rain penetration test, 30 days exposure with a minimum of 17 MJ (16 MBtu) of incident energy per square metre of collector surface area, and a cold fill (thermal shock) test. There was no sign of degradation or loss in performance.
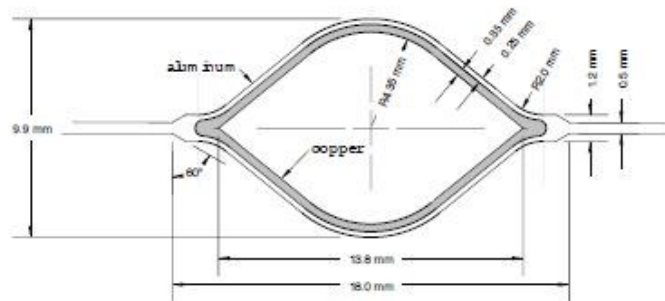
5.0 Durability:
The absorber and the selective surface are not affected by normal aqueous solutions. Stagnation testing has shown no thermal degradation.
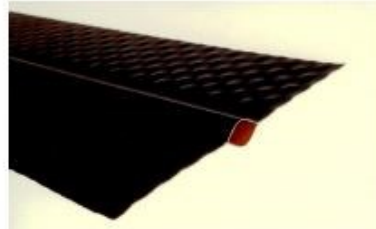
Sunstrip™ solar fin
Aluminum strip metalurgically bonded to a copper tube.

SS146/12:
· 143 mm wide
· 12 mm copper tube
· selective surface

Sunstrip™ solar fin cross section
SS146/12
Scale: 4:1 mm

G SERIES Solar Collectors

Glazed Liquid Flat Plate Collectors
Technical Specifications
SRCC Certification # 100-2006-005A

D. Insulation

1.0 General Description:
Collectors are insulated around the sides and back with fiberglass board. Complies with ASTM-C-612 Classes 1 and 2.

1.1 Trade Names:
Sides: Fiberglas AF530
Back: Fiberglas AF530

1.2 Chemical Composition:
Fibrous glass bonded by a thermosetting resin. Inorganic, will not rot.

1.3 Density:
48 kg/m^3 (3.0 lb/ft^3)

1.4 Thickness:
Side: 25 mm (1")
Back: 25 mm (1")

2.0 Thermal Performance

2.1 Thermal Conductivity:
0.036 W/m·°C (0.25 Btu ·in/hr·ft^2·°F) at 24°C (75°F)

2.2 Thermal Resistance:
RSI 0.7 °C·m^2/W (R 4 °F·ft^2·hr/Btu) at 24°C (75°F)

2.3 Coefficient of Thermal Expansion:
No data available

2.4 Operating Temperature Range:
Maximum continuous operating temperature is 232°C (450°F).

3.0 Fire Behavior

3.1 Surface Burning Characteristics:
Fiberglas AF530 is inherently fire safe. ULC Flame Spread rating of 15. (compared to untreated Red Oak as 100 - test method ULC S-102)

4.0 Durability:
No changes should occur to the insulation when subjected to chemicals normally encountered in use conditions. No thermal degradation has been found after prolonged stagnation testing. Moisture adsorption is less than 0.2% by volume, 96 hours at 49°C (120°F) and 95% R.H. Inorganic therefore does not breed or promote bacteria and fungus. Essentially odorless.

E. Collector Assembly

1.0 General Description:
The collector is assembled in four stages. First, the collector frame and backing sheet are assembled. Second, the back and side insulation are installed. Third, the tested absorber assembly is inserted, and finally, the glazing, seal and cap are installed.

1.1 Container:
The container consists of sections of aluminum extrusion assembled into a rectangular frame, with an aluminum backing sheet fitted into slots and pop-riveted in place.

1.2 Insulation:
Insulation is placed on the aluminum back and along the sides.

1.3 Absorber Assembly:
The pre-assembled absorber is fitted into the insulated container with the inlet and outlet connection pipes protruding through the sides. A high-temperature EPDM gasket is then fitted onto the pipes and locked into the aluminum frame. The absorber is free to expand or contract inside the container.

G32 solar collector
· Gross area: 2.96 m^2 (31.9 ft^2)
· Net: 45 kg (99 lb)

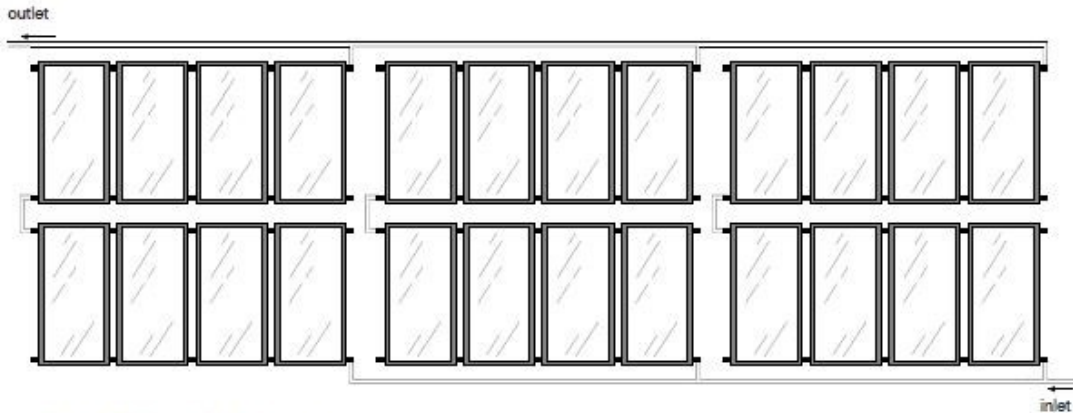# G SERIES Solar Collectors
Glazed Liquid Flat Plate Collectors
Technical Specifications
SRCC Certification # 100-2006-005A

Thermo Dynamics Ltd.
101 Frazee Avenue
Dartmouth, Nova Scotia
Canada, B3B-1Z4
Tel: (902) 468-1001   Fax: (902) 468-1002
Email: solarinfo@thermo-dynamics.com
www.thermo-dynamics.com

THERMO DYNAMICS LTD.

1.4 Glazing Assembly:
The pre-cut glass is cleaned and fitted onto the retainer ledge in the collector container with a high-temperature continuous EPDM gasket. A removable aluminum cap stripping is then secured to the container with black oxide coated stainless steel screws.

2.0 Collector Container:
Collector container sides are fabricated from aluminum extrusions with an integral mounting channel. The bottom is an aluminum sheet which fits into a slot in the frame and is pop-riveted to the sides.

2.1 Materials:
Extruded framework is aluminum 6061-T6 alloy. The back sheet is aluminum utility grade sheet with a thickness of 0.51 mm (.020")

2.2 Finish:
Aluminum frame comes in a standard dark brown baked enamel finish.

3.0 Moisture Control System:
Four holes in the back sheet allow sufficient air flow through the collector to remove any condensation or moisture.

4.0 Sealant and Gaskets

4.1 General Description:
Inlet and outlet pipes are sealed with high-temperature round EPDM gaskets. The continuous glazing gasket is a U-shaped EPDM neoprene. Silicone caulking is used for the container corner sealant.

4.2 Chemical Composition:
Header and glazing gasket: ethylene propylene diene monomer rubber (EPDM)
Caulking: silicone rubber

4.3 Physical Properties:
EPDM gasket has a tensile strength of 13800 kPa (2000 psi). Sealants and gaskets do not corrode other collector materials.

4.4 Coefficient of Thermal Expansion:
no data available.

4.5 Operating Ranges:
no data available.

outlet

inlet

Typical double tier solar collector array.
24 G32 (3m²) solar collectors
Total gross area of 72 m²

G SERIES Solar Collectors

Glazed Liquid Flat Plate Collectors
Technical Specifications
SRCC Certification # 100-2006-005A

F. Installation

1.0 Handling and Transportation

1.1 Packaging:
Collectors are shipped individually in dou-ble-strength cardboard boxes. Perimeter wooden crates are also available.

1.2 Labour and Equipment:
Two people can move and mount collec-tors.

2.0 Mounting Procedure:
Collector mounting channel allows precise spacing between collectors. Two adjacent collectors can be fastened to the sub-struc-ture using bolts positioned anywhere along the bolt track in the collector frame.

3.0 Collector Interconnection:
Connection of up to six collectors in a single array.
Collectors use standard copper couplings sweat-soldered with 95/5 solder to con-nect the internal manifolds of adjacent collectors.

4.0 System Connection:
Piping connections are sweat-soldered to the ends of the collector arrays using standard plumbing fittings.

5.0 Start-up Tests:
i) Air or water pressure test.
ii) Visual check for leaks.

G. Operation

1.0 Method of operation and Control:
Collectors can be used in closed or open loop systems with water or antifreeze.

2.0 Pressure Drop vs. Collector Flow:

ΔP (Pa)
Flow (mL/s)
ΔP (in H_2O)
Flow (USGPM)
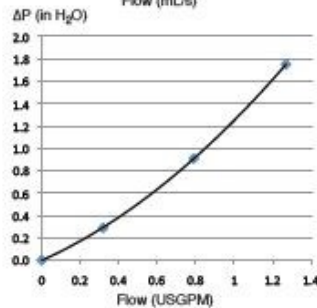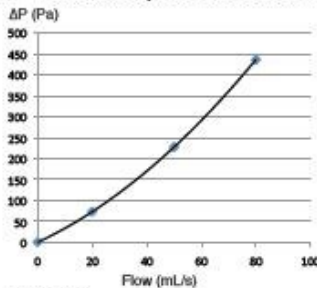
2.1 Testing Information:
Agency: Bodycote Testing Group
Date: January 18, 2007
Fluid: water

3.0 Recommended Flow Rate:
0.8 to 1.5 L/min (0.18 to 0.33 IGPM)

4.0 Maximum Operating Pressure:
Factory tested to 1724 kPa (250 psi).

5.0 Recommended Operating Pres-sure:
Below 200 kPa (30 psi) for drainback systems and 135-270 kPa (20-40 psi) for closed loop systems.

6.0 Maximum Operating Temperature:
200°C (392°F)

7.0 Stagnation Temperature:
Stagnation temperature of the collector is approximately 170°C (338°F).

8.0 Recommended Heat Transfer Flu-ids:
Propylene glycol USP, food grade antifreeze solution for closed loop systems, and water for drainback and seasonal pool systems. The use of inhibited glycols is not recom-mended. DO NOT use ethylene glycol.
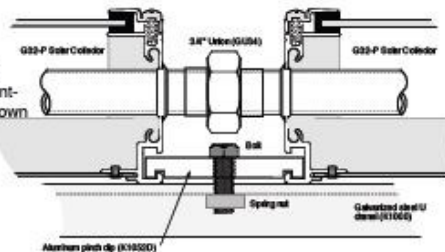

Recommended solar collector mounting methods.
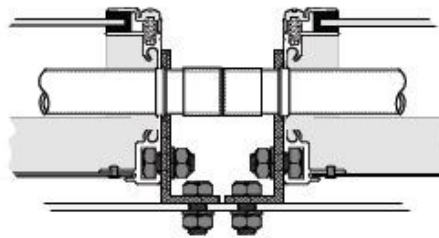
Collector connection using copper coupling. Collector mounting using aluminum angle bracket.

Collector connection using brass union. Collector mount-ing using aluminum pinch down clip.

G SERIES Solar Collectors

Glazed Liquid Flat Plate Collectors
Technical Specifications
SRCC Certification # 100-2006-005A

Thermo Dynamics Ltd.
101 Frazee Avenue
Dartmouth, Nova Scotia
Canada, B3B-1Z4
Tel: (902) 468-1001   Fax: (902) 468-1002
Email: solarinfo@thermo-dynamics.com
www.thermo-dynamics.com

THERMO
DYNAMICS LTD.

H. Maintenance and Warranty

1.0 Cleaning and Maintenance:
Glazing should be self-cleaning, depending on local conditions. Dirt accumulation on the glass cover will be washed away by the rain. If cleaning is required, use a standard window cleaning agent. The glycol antifreeze solution should be checked annually and renewed if necessary. No other maintenance is normally required.

2.0 Manufacturer Servicing:
A trouble-shooting guide to help the homeowner maintain and service the equipment is included in the installation manual. All service and repair is readily available from the manufacturer or distributor.

3.0 Availability of Parts:
All parts are available from the manufacturer and distributors.

4.0 Replacement of Parts:
The glazing may be replaced in the installed system without removing the collector from the array by removing the screws holding the glazing cap stripping. Total replacement time is a maximum of fifteen minutes and requires only a screw driver. Sensors are clamped on outlet piping using screw-type pipe clamps. Replacement time is approximately ten minutes.

If the recommended installation procedures are followed, one collector may be replaced in the array without removing another collector. Collectors are connected together with a standard copper couplings (mechanical or soldered).

5.0 Warranty:
The solar collector absorber is warranted for a period of ten years. Repair allowances may also apply. The manufacturer may repair or replace the absorber as required at his discretion.

I. Durability

1.0 Operating Experience:
The G32 has been installed worldwide since 1985.

2.0 Accelerated Aging Tests:
The collector has been subjected to 30 day plus high temperature (204°C;400°F) stagnation tests at the Canadian National Solar Test Facility with no evidence of deterioration (CSA F-378). One year of stagnation at DSET laboratories in Arizona were also conducted in 1982 with no sign of deterioration.

CFB Gagetown, New Brunswick, Canada
40 - G32-P Solar collectors
Solar Domestic Hot Water

YMCA, Yarmouth, Nova Scotia, Canada
40 G32-P Solar collectors
Solar Pool Heating

Thermo Dynamics Ltd, Dartmouth, Nova Scotia, Canada
30 - G32-P Solar collectors
Solar Radiant Floor Heating

Residence, Halifax, Nova Scotia, Canada
6 - G32-P Solar collectors
Solar Radiant Floor Heating, Solar Domestic Hot Water

G SERIES Solar Collectors

Glazed Liquid Flat Plate Collectors
Technical Specifications
SRCC Certification # 100-2006-005A

J. Collector Efficiency

1.0 General Description

1.1 Test Method:
Tested in accordance with SRCC (Solar Rating and Certification Corporation) 100-05, "Test Methods and Minimum Standards for Certifying Solar Collectors" with reference to ANSI/ASHRAE Standard 93 and ISO 9806-1.

1.2 Testing Information:
Agency: Bodycote Testing Group
Location: Ontario, Canada
    Lat. 43.53 °N
    Long. 79.66 °W
    Elevation: 160 m (525 ft)
Date: January 18, 2007
Web: www.bodycote.com

1.3 Details of Tested collector:
Model: G32-P
Glazing: low-iron tempered Solite
Absorber material: aluminum fin and tube
Absorber coating: SOLEC paint
Insulation: fiberglass
Gross area: 2.982 m² (32.10 ft²)
Aperture area: 2.783 m² (29.96 ft²)
Absorber area: 2.870 m² (30.89 ft²)

1.4 Comments:
The time constant, thermal efficiency and incident angle modifier were determined in the solar simulator.

2.0 Test Conditions

2.1 Collector Tilt and Orientation:
Normal to the direction of irradiation.

2.2 Heat Transfer Fluid:
Water

2.3 Liquid Flow Rate:
0.059 kg/s (0.13 lb/s)

2.4 Mean Ambient Air Temperature:
20.3°C (68.5°F)

2.5 Wind Velocity:
3.2 m/sec (10.5 ft/sec)

2.6 insolation:
808 W/m²
256 Btu/ft² h

3.0 Time Constant:
95 sec at 0.059 kg/s (0.139 lb/s) water
Inlet temperature: 22.8°C (73.0°F)
Ambient temperature: 20.1 (68.2°F)

4.0 Efficiency:
First order efficiency equation:
$$\eta = 0.700 - 4.933(T_i - T_a)/G$$
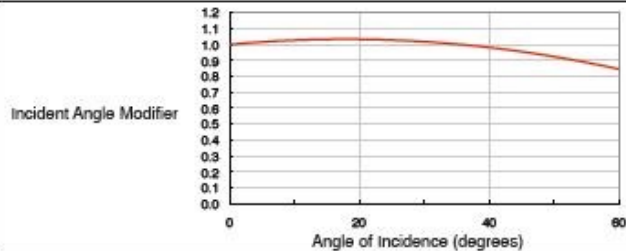
5.0 Incident Angle Modifier:
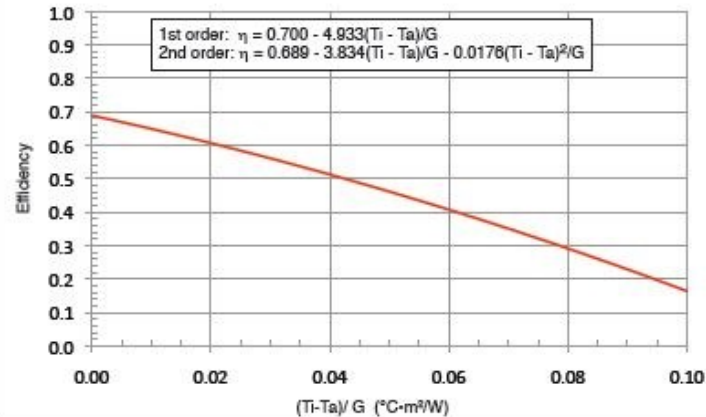$$K_{(\tau\alpha)} = 1 - 0.154(1/\cos\theta - 1)$$

6.0 FSEC Standard Day Tests:
The following standard day tests were performed by the Solar Rating & Certification Corporation, (SRCC).

SRCC Standard Day Tests, (SRCC Standard 100-81)

Megajoules Per Panel Per Day				Thousands of Btu Per Panel Per Day			
Category (Ti - Ta)	Clear Day 23 MJ/m²•d	Mildly Cloudy 17 MJ/m²•d	Cloudy Day 11 MJ/m²•d	Category (Ti - Ta)	Clear Day 2000 Btu/ft²•d	Mildly Cloudy 1500 Btu/ft²•d	Cloudy Day 1000 Btu/ft²•d
A (-5°C)	41.8	31.6	21.4	A (-9°F)	39.6	29.9	20.3
B (5°C)	37.3	27.0	16.9	B (9°F)	35.3	25.6	16.0
C (20°C)	30.4	20.4	10.4	C (36°F)	28.8	19.3	9.9
D (50°C)	17.2	8.1	1.1	D (90°F)	16.3	7.7	1.1
E (80°C)	5.8	0.2		E (144°F)	5.5	0.2	

Incident Angle Modifier

Collector Thermal Efficiency

1st order: $\eta = 0.700 - 4.933(T_i - T_a)/G$
2nd order: $\eta = 0.689 - 3.834(T_i - T_a)/G - 0.0176(T_i - T_a)^2/G$

(Ti-Ta)/ G (°C•m²/W)